**NATIONAL TECHNICAL UNIVERSITY OF ATHENS**
**SCHOOL OF NAVAL ARCHITECTURE & MARINE ENGINEERING**
**DIVISION OF MARINE ENGINEERING**

# DIPLOMA THESIS

**VASSILIS ZOUZOULAS**

# Thermohydrodynamic analysis of tilting pad thrust bearings with artificial surface texturing

**Thesis Committee:**

| | |
|---|---|
| **Supervisor:** | **C.I. Papadopoulos, Assistant Professor NTUA** |
| **Members:** | **L. Kaiktsis, Associate Professor NTUA** |
| | **G. Papalambrou, Lecturer NTUA** |

**Athens, December 2014**

**ΕΘΝΙΚΟ ΜΕΤΣΟΒΙΟ ΠΟΛΥΤΕΧΝΕΙΟ**
**ΣΧΟΛΗ ΝΑΥΠΗΓΩΝ ΜΗΧΑΝΟΛΟΓΩΝ ΜΗΧΑΝΙΚΩΝ**
**ΤΟΜΕΑΣ ΝΑΥΤΙΚΗΣ ΜΗΧΑΝΟΛΟΓΙΑΣ**

# ΔΙΠΛΩΜΑΤΙΚΗ ΕΡΓΑΣΙΑ

**ΒΑΣΙΛΕΙΟΣ ΖΟΥΖΟΥΛΑΣ**

# Θερμοϋδροδυναμική ανάλυση αυτορρυθμιζόμενων ωστικών εδράνων με τεχνητή επιφανειακή τραχύτητα

**Εξεταστική επιτροπή:**

**Επιβλέπων:** **Χ.Ι. Παπαδόπουλος, Επίκουρος Καθηγητής ΕΜΠ**

**Μέλη:** **Λ. Καϊκτσής, Αναπληρωτής Καθηγητής ΕΜΠ**

**Γ. Παπαλάμπρου, Λέκτορας ΕΜΠ**

**Αθήνα, Δεκέμβριος 2014**

## Acknowledgements

First and foremost, I would like to express my deepest gratitude to my supervisor, Assistant Professor Christos Papadopoulos for his dedicated involvement and assistance throughout every step of the present thesis. His enthusiasm has been an inspiration and essential to this project.

I must also thank the whole tribology research team for their constructive comments, guidance and for their will to help at crucial moments.

The data used for the validation of the studied model was graciously provided by Prof. Michael Fillon from the University of Poitiers, and I thank him for his kind cooperation.

Finally, a very special thanks is owed to my parents and brother who provided me the chance for an education, and supported me all these years of my studies, to Elina for her encouragement and precious contribution during the writing process, and to all my friends and fellow students for the experiences, skills and time we shared.

## Abstract

Friction is one of the most important causes of energy losses in mechanical systems. In ships, substantial friction losses are present in the propulsion system, both in the engine (in piston rings, crankshaft bearings and connecting rod bearings, etc.), and in the shaft arrangement (in journal bearings and in thrust bearings), as well as in the gearbox unit, if it exists.

The present work is concerned with the study of friction losses and their mitigation in thrust bearings, especially in those which fall into the category of fluid film bearings. These key machine components are used to transfer large axial loads between a rotating and a stationary part by developing hydrodynamic pressure in a thin lubricant film that separates the shaft from the bearing. Apart from their usage in marine propulsion systems, thrust bearings can also be found in many other rotating machines like pumps, turbines, compressors and hydro generators.

The aim of the present study is to model both the thermal and the hydrodynamic phenomena (Thermohydrodynamic - THD analysis) of the fluid flow during the operation of a tilting-pad thrust bearing, using Computational Fluid Dynamics (CFD). To this end, a geometric model of a three dimensional sector-shaped bearing pad is generated and utilized within a CFD code, which calculates the tribological characteristics of the system. Additionally, a developed scripting tool is used to attain the equilibrium position of the bearing pad, by equalizing the forces and moments exerted on the system. Attention is given to the trends of essential operating parameters, including minimum film thickness, friction torque, maximum fluid temperature and maximum fluid pressure, under various operating conditions, in particular under different rotating speeds and imposed thrust loads.

Following the results of recent research, which have shown that application of artificial surface texturing to a part of a sliding surface may lead to reduced friction and increased film thickness in other tribological applications, this study investigates the impact of certain geometric patterns on the performance of tilting-pad thrust bearings. Four different types of thrust bearings of the same principal dimensions have been evaluated for different combinations of thrust load and rotational speed: (a) a pocket bearing, (b) a bearing with circumferential grooves, (c) a bearing with radial grooves and (d) a bearing with rectangular texturing. In addition, for the two most effective geometries, a parametric analysis has been conducted to identify the effect of the main design parameters on bearing performance. The examined parameters are the textured depth, as well as the radial and circumferential texture extents. For each case, the performance

gains obtained by texturing are evaluated with respect to the performance of a conventional plain bearing. Finally, following a different approach, the potential effects on thrust bearing performance of introducing hydrophobic properties on part of the tilting-pad surface are assessed.

The present results demonstrate a potential for substantial improvement of bearing performance, with proper application of artificial surface texturing or hydrophobicity to the tilting-pads of thrust bearings. Specifically, introducing a large shallow pocket of appropriate dimensions at the inflow region of the pads may result in reduction of friction torque of approximately 12% in comparison to the plain tilting-pad thrust bearing, thus substantially improving bearing efficiency. At the same time, the observable increase in minimum thickness of the lubricating film (an indicator of bearing performance) reaches 23%. Even more impressive results can be expected by application of hydrophobicity to the tilting-pads of a thrust bearing. Based on the present results, an increase of 62% in minimum film thickness and a simultaneous decrease of 32% in friction torque, in comparison to the plain tilting-pad thrust bearing, can be theoretically achieved.

## Σύνοψη

Η τριβή αποτελεί μία από τις βασικότερες αιτίες ενεργειακών απωλειών στα μηχανολογικά συστήματα. Στα πλοία, σημαντικές απώλειες εξαιτίας των τριβών εντοπίζονται στη προωστήρια εγκατάσταση, τόσο στο εσωτερικό της κυρίας μηχανής (στα ελατήρια των εμβόλων, στα έδρανα βάσης και διωστήρα), όσο και στο αξονικό σύστημα (στα έδρανα γραμμής και χοάνης, καθώς και στο ωστικό έδρανο), όπως επίσης και στον μειωτήρα όταν υπάρχει.

Η παρούσα εργασία, αφορά στη μελέτη των απωλειών τριβής σε ωστικά έδρανα, και ειδικότερα σε εκείνα που εμπίπτουν στη κατηγορία των εδράνων υδροδυναμικής λίπανσης. Τα ωστικά έδρανα αποτελούν βασικά μηχανολογικά στοιχεία που χρησιμοποιούνται για τη μετάδοση μεγάλων αξονικών δυνάμεων, αξιοποιώντας τις υδροδυναμικές πιέσεις που αναπτύσσονται στο εσωτερικό ενός λεπτού φιλμ λιπαντικού που διαχωρίζει τον περιστρεφόμενο άξονα από το σταθερό τμήμα του εδράνου. Πέρα από τη χρήση τους στα ναυτικά συστήματα προώσεως, τέτοιου είδους έδρανα απαντώνται σε περιστρεφόμενες μηχανές διαφόρων ειδών, όπως οι αντλίες, οι στρόβιλοι, και οι συμπιεστές.

Στόχο της παρούσας εργασίας αποτελεί η μοντελοποίηση τόσο των θερμικών όσο και των υδροδυναμικών φαινομένων του ρευστού κατά τη λειτουργία ενός αυτορρυθμιζόμενου ωστικού εδράνου. Για τον σκοπό αυτόν δημιουργήθηκε τρισδιάστατο γεωμετρικό μοντέλο ενός πέλματος του εδράνου, το οποίο αξιοποιήθηκε στο πλαίσιο ενός κώδικα Υπολογιστικής Ρευστοδυναμικής (CFD), για τον υπολογισμό των τριβολογικών χαρακτηριστικών του συστήματος. Επιπλέον, με τη χρήση ενός προγραμματιστικού εργαλείου που αναπτύχθηκε στο πλαίσιο της παρούσας εργασίας, έγινε δυνατή η εύρεση της θέσης ισορροπίας του πέλματος του εδράνου, λαμβάνοντας υπόψη τις δυνάμεις και ροπές που εξασκούνται στο σύστημα. Έμφαση δόθηκε στη καταγραφή και ανάλυση βασικών παραμέτρων λειτουργίας όπως το ελάχιστο πάχος του λιπαντικού φιλμ, η ροπή αντίστασης λόγω τριβών, η μέγιστη θερμοκρασία και η μέγιστη πίεση του λιπαντικού, σε διαφορετικές καταστάσεις λειτουργίας του εδράνου (διαφορετικές ταχύτητες περιστροφής του άξονα και διαφορετικές αξονικές δυνάμεις).

Ακολουθώντας τα αποτελέσματα πρόσφατων ερευνητικών προσπαθειών, τα οποία καταδεικνύουν ότι εφαρμογή τεχνητής τραχύτητας σε μέρος της επιφάνειας του εδράνου μπορεί να οδηγήσει σε μειωμένη τριβή και αυξημένα πάχη λιπαντικού, η παρούσα εργασία εξετάζει την επίδραση συγκεκριμένων επιφανειακών διαμορφώσεων στην απόδοση ενός αυτορρυθμιζόμενου ωστικού εδράνου. Στην παρούσα εργασία μελετήθηκαν ωστικά έδρανα με τέσσερις διαφορετικές μορφές επιφανειακής τραχύτητας, ίδιων κύριων διαστάσεων, σε διάφορους συνδυασμούς φόρτισης και

περιστροφικής ταχύτητας: (α) έδρανα με ενιαία ρηχή κοιλότητα στην περιοχή εισόδου του λιπαντικού ελαίου, (β) έδρανα με περιφερειακές εγκοπές (αυλάκια), (γ) έδρανα με ακτινικές εγκοπές, (δ) έδρανα με ορθογωνική επιφανειακή τραχύτητα. Στη συνέχεια, για τα δύο αποδοτικότερα είδη εδράνων, διεξήχθη παραμετρική ανάλυση για να εξακριβωθεί η επίδραση των βασικών γεωμετρικών παραμέτρων στην απόδοσή τους. Οι εξεταζόμενες παράμετροι είναι το βάθος τραχύτητας, καθώς και η έκτασή της κατά την ακτινική και περιφερειακή διεύθυνση. Σε κάθε περίπτωση, η βελτίωση ποσοτικοποιήθηκε συγκρινόμενη με την απόδοση ενός συμβατικού εδράνου αναφοράς. Τέλος, ακολουθώντας μια διαφορετική προσέγγιση, αξιολογήθηκε η δυνατότητα βελτίωσης της απόδοσης ωστικών εδράνων, μέσω εφαρμογής υδροφοβικών χαρακτηριστικών σε τμήμα της επιφάνειας του πέλματος.

Τα παρόντα αποτελέσματα καταδεικνύουν τη δυνατότητα σημαντικής βελτίωσης της απόδοσης των ωστικών εδράνων, με κατάλληλη εφαρμογή τεχνητής τραχύτητας ή υδροφοβικότητας σε τμήμα της επιφάνειας του πέλματος. Συγκεκριμένα, η εισαγωγή μιας ενιαίας μεγάλης ρηχής κοιλότητας στην περιοχή εισόδου του λιπαντικού ελαίου μπορεί να οδηγήσει σε μείωση έως και 12% της ροπής τριβής, ενώ η αντίστοιχη αύξηση του ελάχιστου πάχους του λιπαντικού φιλμ είναι της τάξης του 23%. Περισσότερο υποσχόμενα είναι τα αποτελέσματα για τη περίπτωση της εφαρμογής υδροφοβικότητας σε αυτορρυθμιζόμενα ωστικά έδρανα, δίνοντας θεωρητικά μέγιστα της τάξεως του 62% αναφορικά με την αύξηση του ελάχιστου πάχους φίλμ, και 32% αναφορικά με τη μείωση της ροπής τριβής, σε σχέση με το συμβατικό έδρανο αναφοράς.

## Table of Contents

## Nomenclature

| | |
|---|---|
| $A$ | pad area ($m^2$) |
| $B$ | pad width (mm) |
| $B_t$ | width of textured area (mm) |
| $B_s$ | width of hydrophobic area (mm) |
| $c_{pf}$ | specific heat capacity of fluid (J/kg.K). |
| $c_{ps}$ | specific heat capacity of solids (J/kg.K) |
| $D_m$ | pad mean diameter (mm) |
| $D_i$ | pad inner diameter (mm) |
| $D_o$ | pad outer diameter (mm) |
| $\Theta_P$ | pad angle (°) |
| $\Theta_{Pivot}$ | circumferential position of pivot point (°) |
| $R_{Pivot}$ | pivot radius (mm) |
| $t_{pad}$ | pad thickness (mm) |
| $t_{collar}$ | collar thickness (mm) |
| $F_f$ | friction force (N) |
| $T_f$ | friction torque (Nm) |
| $f$ | friction coefficient |
| $f^*$ | normalized friction coefficient: $f^* = \frac{F_f.L}{W \cdot H_{min}}$ |
| $H$ | local film thickness (µm) |
| $H_{min}$ | minimum film thickness (µm) |
| $H_{Pivot}$ | film thickness at pivot location (µm) |
| $H_{ref}$ | reference film thickness (µm) |

$H_t$ textured depth (mm)

$L$ pad length at bearing mid-sector (mm)

$L_t$ textured length at bearing mid-sector (mm)

$L_s$ length of hydrophobic area at bearing mid-sector (mm)

$M_{x,p}$ x- component of torque about pivot point (Nm)

$M_{y,p}$ y- component of torque about pivot point (Nm)

$N_p$ number of pads

$N$ rotational speed (RPM)

$P$ specific load (MPa)

$p$ pressure (Pa)

$Pr$ Prandtl number

$P_f$ power loss due to friction

$Q_{feed}$ feeding oil flow rate ($m^3/s$)

$r$ radial coordinate (mm)

$Re$ local Reynolds number: $Re = \rho UH/\mu$

$T$ fluid temperature ($^oC$)

$T_{amb}$ ambient temperature ($^oC$)

$T_{in}$ fluid inlet temperature ($^oC$)

$T_{ex}$ fluid outlet temperature ($^oC$)

$T_{feed}$ feeding oil temperature ($^oC$)

$U$ rotor speed at pad mid-sector (m/s): $U = \omega \cdot r$

$\boldsymbol{V}$ fluid velocity vector

$W$ bearing load capacity / thrust load (N)

$x_P$ circumferential coordinate of a local Cartesian system having the pivot point as the origin

$y_P$ radial coordinate of a local Cartesian system having the pivot point as the origin

$\alpha$ hot oil mixing coefficient: $\alpha = \frac{T_{in}-T_{ex}}{T_{feed}-T_{ex}}$

$a_{conv}$ convention coefficient (W/m$^2$.K)

$\theta_{Pitch}$ tilt angle about the pivot point in the circumferential direction (μdeg)

$\theta_{Roll}$ tilt angle about the pivot point in the radial direction (μdeg)

$\lambda_f$ thermal conductivity of fluid (W/m.K)

$\lambda_s$ thermal conductivity of solid (W/m.K)

$\mu$ fluid dynamic viscosity (Pa.s)

$\nu$ fluid kinematic viscosity (cSt)

$\rho$ fluid density (kg/m$^3$)

$\tau$ shear stress (Pa)

$\omega$ rotor angular velocity (rad/s)

## List of Figures

## List of Tables

# 1. Introduction

## 1.1. The significance of tribology

Tribology is the science that studies friction, wear and lubrication of interacting surfaces that are in relative motion. While it is a relatively new branch of science, tribology is the mature result of the basic need of human activity to minimize work and wear wherever loads and motion must be transmitted between mechanical parts. The science of tribology draws from several other scientific branches including physics, mechanics, chemistry, engineering, and it encompasses a wide range of topics. These include the modeling of lubrication phenomena as well as the subsequent, development of new lubricants or surface treatment technologies and the general optimization of tribological elements, with the aim of reducing power losses or wear.

Though there have been great steps towards design optimization of machinery components in the last century, controlling friction and wear is still a topic of intense research and development. As is well known, friction between the moving parts of a machine leads to heat generation and (unwanted) power loss. It is estimated that one third of global energy consumption is spent in attempt to overcome friction in the various forms that it occurs. Clearly, the potential economic benefits of reducing friction are significant, but it is also recent environmental concerns which are responsible for the increasing interest in this field. In industry, there are countless numbers of applications which involve moving parts with surfaces in close proximity to each other, varying in scale from tiny micro turbines to massive machines like hydro generators.

The field of marine engineering is no exception and comprises many applications where friction plays a decisive role in overall performance. In ships, important power losses are present in Diesel engines (in piston rings, crankshaft bearings and connecting rod bearings which in total lead to 5-7.5% power loss of BHP), at the shaft arrangement system (where losses of 1-2% of BHP in thrust bearing and journal bearings can be found) as well as in the gear unit (with losses around 1-2% of BHP), if it exists (Figure 1). Energy cost due to friction and wear for a particular mechanical device may seem low compared to the total power of the device. However considering those same losses for a large number of similar-type systems, the cost becomes very important over time.

(a)

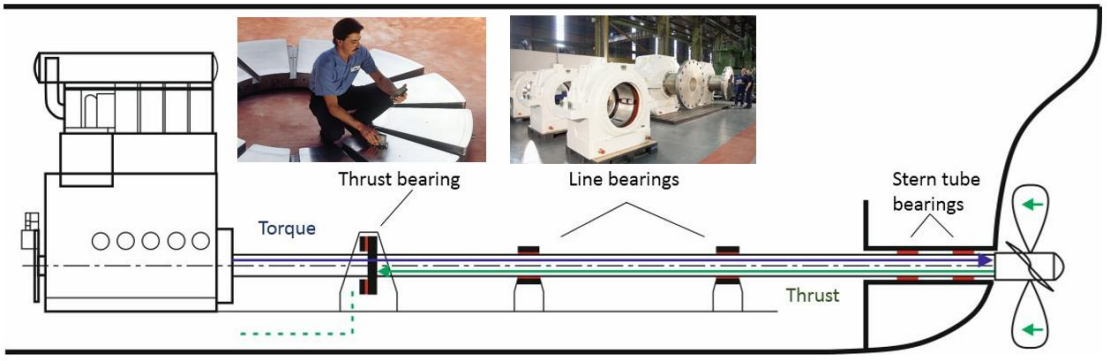


(b)

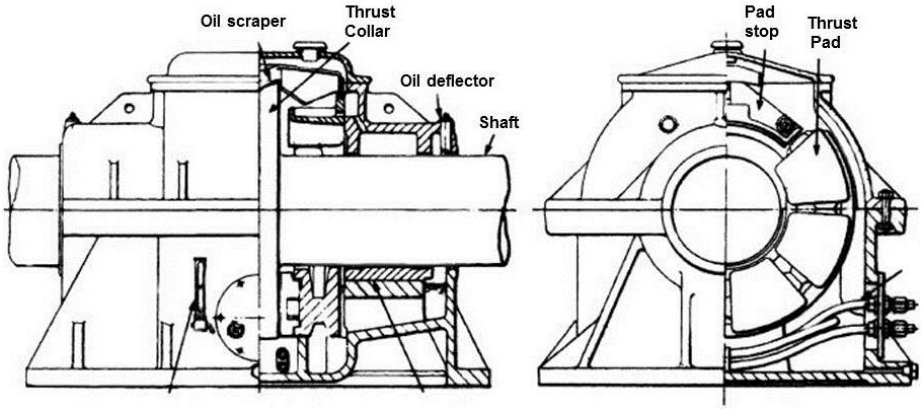


**Figure 1 (a) Typical arrangement of a marine propulsion system, and (b) typical thrust block unit.**

## 1.2. Historical-Literature review

One of the oldest and most important ways to reduce friction and the associated wear is a phenomenon called hydrodynamic lubrication. The theoretical basis of hydrodynamic lubrication was laid in 1886 by Osborne Reynolds and, to this day, it continues to be enriched by the publication of numerous research papers every year. According to Reynolds' theory, two sliding surfaces separated by a thin lubricating film of an appropriate fluid can transmit a thrust load between them on the condition that they have a slight relative inclination. In the converging region between the two surfaces, a pressure is generated to balance the applied load and maintain the separation between the surfaces, reducing friction wear and excessive heating of the mechanical components.

Among the typical applications of hydrodynamic lubrication are thrust bearings, designed to transfer axial loads between rotating and stationary parts. The standard design of

thrust bearings for many decades consisted of circumferentially placed pads with fixed surface inclination. Pivoted or tilting thrust bearings, in which each pad can rotate and balance at several inclinations, were first invented early in the 20th century. However, they were not widely used until several decades later due to their increased cost relative to fixed pad bearings. Independently invented by Kingsbury and Michell, tilting pad bearings, are able to self-adjust to optimal film geometry for any operating condition thanks to a joint located at the base of each pad. This unique ability is why, after overcoming some design problems associated with high parasitic losses, tilting-pad bearings proved their superior performance and they are now commonly used in all kinds of high-tech applications.

The improvements in the design of both fixed and tilting pad thrust bearings have been aided by corresponding developments on a theoretical level. Originally, the analyses of hydrodynamic thrust bearings were predominantly based on the solution of Reynolds equation for pressure distribution. However, with the constantly growing capacity of computers, research increasingly included solutions of more generalized forms of the Reynolds equation which take into account more complex fluid flow characteristics. These more recent numeric studies also considered significant secondary phenomena like viscosity variations [1], groove effect for determining the inlet pressure [2-3] and temperature [4] as well as elastic deformations of the pads and the collar due to pressure and thermal fields [5]. A recent study [6] has shown that, of the above, thermal effects in particular can drastically affect bearing performance indices, especially at high rotational speeds or/and loads.

With the deeper understanding of the tribological phenomena of hydrodynamic lubrication, the potential for optimizing existing designs expanded. New concept designs turned to the implementation of roughness patterns on the faces of the bearing components [7-10]. This process, called surface texturing, included the introduction of small, periodic irregularities of various shapes on a lubricated surface that could reduce frictional losses and increase load carrying capacity. Many experimental studies [11-12] have confirmed the effectiveness of such solutions: proper application of artificial textured patterns on part of the stator surface can, in certain situations, build up thicker lubricating films, simultaneously reducing the friction coefficient and acting against wear. For fixed pad thrust bearings in particular, the effects of implementing artificial surface texturing of varying characteristics have been presented in [13]. The authors found that optimal texturing dimensions do exist in terms of load capacity with texture density being the key parameter into improving a bearing's performance.

Research on surface texturing has been accompanied and further amplified by the advances in surface treatment technologies which have enabled the accurate manufacturing of texture patterns on machine components such as journal and thrust bearings with resolutions in the micron scale [14]. Although such surfaces, textured with micro-stereo lithography technology, have not been fully implemented in the industry, the potential for enhancing the tribological performance of machine elements has extensively been investigated by using laser surface texturing [15-16]. Aside from the above, other surface treatment techniques have been widely utilized, such as chemical etching, surface indentation, micromachining, LIGA processes and ultrasonic methods.

While the technical challenges of implementing surface texturing in bearing designs are being increasingly met, the issue of successfully modeling such designs still remains open. While, in general, the use of the Reynolds equation gives satisfactory results for problems of hydrodynamic lubrication in which the interacting surfaces have a simple geometry and the rotation speeds are small, it is not so effective for more complex textured geometries. For textured infinite-width sliders, the applicability of the Reynolds equation has been investigated in [17]. It was shown that the validity of the Reynolds equation cannot be decided by the Reynolds number alone, as the geometric parameters of the texturing (in particular, aspect ratio and depth) may have an equally important influence. As a result, the present state of the art models include three-dimensional solutions of the Navier-Stokes equations together with simultaneous solutions of the energy equation, resulting in full thermohydrodynamic (THD) simulations of textured bearings [18-19]. Such complex CFD analyses provide a better insight at the flow field and the operational characteristics of the bearings and, in contrast to older models based on the Reynold equation, they are capable of taking the effects of fluid inertia into account, as well as those of temperature and pressure distribution in the film thickness.

Optimization of the texture geometry and placement has also been attempted by several researchers. Either by utilizing Reynolds equation e.g. [12,20], or by using CFD [13,21], the results of such studies for textured pad thrust bearings prove the existence of an optimal design for a certain geometry and operating profile.

Though optimization of textured surfaces seems to have the potential to substantially improve bearing designs, many researchers have recently shifted their focus to the study of a much more promising surface treatment. In particular, many efforts have been oriented towards the idea of applying hydrophobic properties on sliding surfaces. Hydrophobic surfaces have wetting resistant characteristics, which drastically reduce the levels of friction during fluid flow [22-23]. A succession of experimental studies using several different methods has proven that, on such surfaces, simple Newtonian liquids

can slip over a solid boundary [24-25]. In particular, this occurs with surfaces characterized by a complex nano-structure, and fluids that exhibit low adhesion in the fluid-structure interface. The observed results are consistent with slip occurring at a critical shear stress of 0.03 Pa and a Navier slip length of 4 μm [26].

## 1.3. Goals of the present study – Thesis outline

Due to the limitations imposed by the application of the Reynolds equation, the use of Navier-Stokes equation solvers has become increasingly important in the flow analysis of fluid bearings. However, due to the high computational cost of a completely realistic, assumption-free solution, the majority of CFD studies have been isothermal and restricted to the study of fixed geometry flows. Taking this into account, the present study aims at modeling not only the flow but also thermal effects in tilting-pad thrust bearings. For these bearings, the equilibrium position of bearing is also sought, therefore, the proposed CFD-based thermohydrodynamic solver is coupled with an iterative equilibrium solver, based on the Newton-Raphson method.

The present model is first generated and validated for a typical smooth tilting pad thrust bearing. Then, the model is appropriately extended to account for different surface treatment patterns of the stator surface. In particular, four different patterns are considered, namely those of a stator with a large shallow pocket in the region of oil entrance, a stator with circumferential or radial grooves and a partially textured stator with rectangular dimples. For the two types of geometry with the most favorable performance, a parametric analysis is performed in order to identify the effect of texturing design parameters on bearing performance characteristics. Finally, the potential of implementing hydrophobic properties on part of the stator surface is also investigated. The summarized findings of the present thesis are presented and conclusions are drawn in the final chapter.

# 2. Thrust Bearings

## 2.1. Overview

A quite detailed definition for bearings is given by Hamrock [27], who states: “A bearing is a support or guide that locates one machine component with respect to others in such a way that prescribed relative motion can occur while forces associated with machine operation are transmitted smoothly and efficiently”.

In general, bearings can be categorized in two classes: bearings with rolling elements and sliding bearings. Rolling element bearings, Figure 2(a), attempt to minimize friction by introducing interfaces such as balls, cylinders or barrels which rotate in a direction opposite to the relative motion of the two surfaces. These are the most common type of bearings and are found in numerous applications in everyday life.

On the other hand, the term sliding bearing (see Figure 2(b)) refers to a type of bearing where two surfaces slide relative to each other with load distributed perpendicular to the interface. The "interface" in this case is a sufficiently thick film of lubricant, which is maintained between the sliding surfaces in order to keep them at a distance. The lubricant may be liquid or gas, and its load-carrying capacity is derived from the pressure within the lubricating film; this pressure is generated by hydrodynamic effects due to the relative motion of the sliding surfaces (self-acting bearings), by external pressurization (hydrostatic bearings), or by a combination of these actions (hybrid bearings).

Sliding bearings are commonly used in applications characterized by high loads and dynamic effects that require high standards in terms of lifespan and efficiency, which rolling bearings cannot provide. They are also preferred for their accuracy, robustness, lower noise levels and absence of vibration effects. Based on the direction of the forces acting on the bearing, sliding bearings can be categorized as journal bearings (support of radial forces) or thrust bearings (support of axial forces), with the latter being the subject of the present work.

Tilting pad fluid-film thrust bearings were invented by the Australian engineer G. Michell, and since then they have been implemented in various types of rotating machinery, such as pumps, compressors and turbines. A significant application of tilting pad technology are the thrust bearings in marine propulsion systems, which are responsible for receiving the axial forces produced by the propeller and subsequently transmitting the thrust to the whole ship structure.

Typically, thrust bearings consist of a moving part (rotor) and a stationary part (stator). The stator is composed by a number (usually 5 to 8) of circular sections or sector shaped

pads, circumferentially arranged. The lubricant required to form a thin film between the moving and the stationary bearing parts is usually supplied through appropriate grooves between each pair of pads.

**Figure 2: Sketch of (a) a thrust ball bearing, and (b) of a hydrodynamically lubricated thrust bearing.**

As already mentioned, this type of bearings operate based on the principle of hydrodynamic lubrication. Basic conditions for the development of a hydrodynamic lubrication film are the following:

- The usage of viscous lubricant
- Sufficient relative velocity of the interacting surfaces
- Slight inclination of the interacting surfaces relative to each other

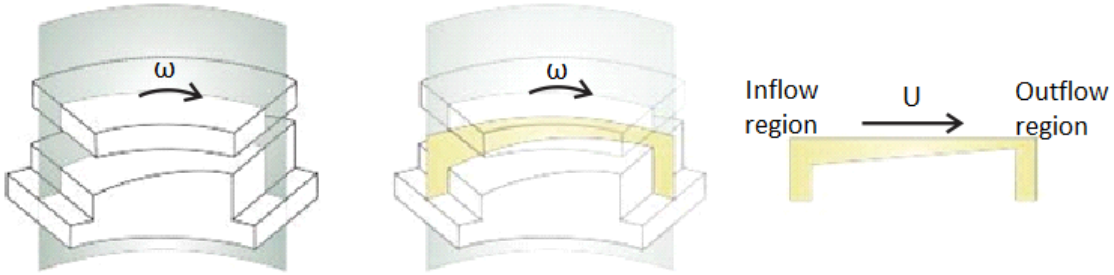


**Figure 3: Formation of hydrodynamic wedge in converging sector pad thrust bearings.**

The geometry of a converging micro-channel is presented in Figure 3. The moving wall generates shear forces, and exerts motion to the fluid which flows from the channel inflow to the outflow. As the fluid passes through the wedge geometry, it builds up pressure, which exerts forces on the channel walls. Force equilibrium is attained by the

presence of an external vertical load $W$ on both walls. Throughout this process, energy is expended by the work done by the shear forces at the moving wall - fluid interface.

The load carrying capacity is greatly dependent on the convergence angle of the wedge and, as a result, fixed inclination bearings do not work well under varying operating conditions. In order to have a satisfactory behavior in different loads, a prerequisite for many applications, a pivot point is placed at the bottom of the stationary pad. In this way small changes in angle (tilting) are allowed in all directions granting the ability of self-adjustment depending on load requirements. Therefore, changes in thrust load, rotational speed or lubricant viscosity will be followed by an adjustment of the bearing position (equivalently of the film geometry), so that equilibrium of forces is achieved. This change in geometry means reducing or increasing the minimum clearance between the faces of the stator and collar as smaller film thicknesses lead to higher pressure and thus higher load-carrying capacity, and vice versa.

Since each pad in the bearing is free to rotate about a pivot or, less often, along a line, or suspended on an array of springs [28], moments cannot be developed. As a result, the destabilizing forces are greatly reduced or eliminated, and the bearings are no longer a potential source of rotor-dynamic instability. This feature has made tilting pad bearings the standard fluid-film bearing for most high-speed applications.

As with all lubrication-based applications, the effectiveness of fluid-film bearings is based on the type of lubrication they provide, namely on the "lubrication regime" of the specific application. The main lubrication regimes are illustrated in Figure 4. This diagram is commonly referred as the “Stribeck curve”, after the German engineer Richard Stribeck. The dominating lubrication regime between two surfaces is indicated by the value of viscosity relative to the dimensionless film thickness parameter Λ which is a function of the minimum film thickness and of the surface roughness expressed as the quadratic mean surface deviation of the lubricated surfaces.

Correctly dimensioned, the bearings operate in the hydrodynamic lubrication regime and are only subject to boundary and mixed lubrication regimes during transient operating conditions such as sudden changes in load or speed, and at startup. The latter issue can be dealt with by using hydrostatic jacking for lifting up the rotor at startup. In general, the critical limit for low-speed operation is minimum oil film thickness, while in high-speed operation, the maximum temperature is usually the limiting criterion.

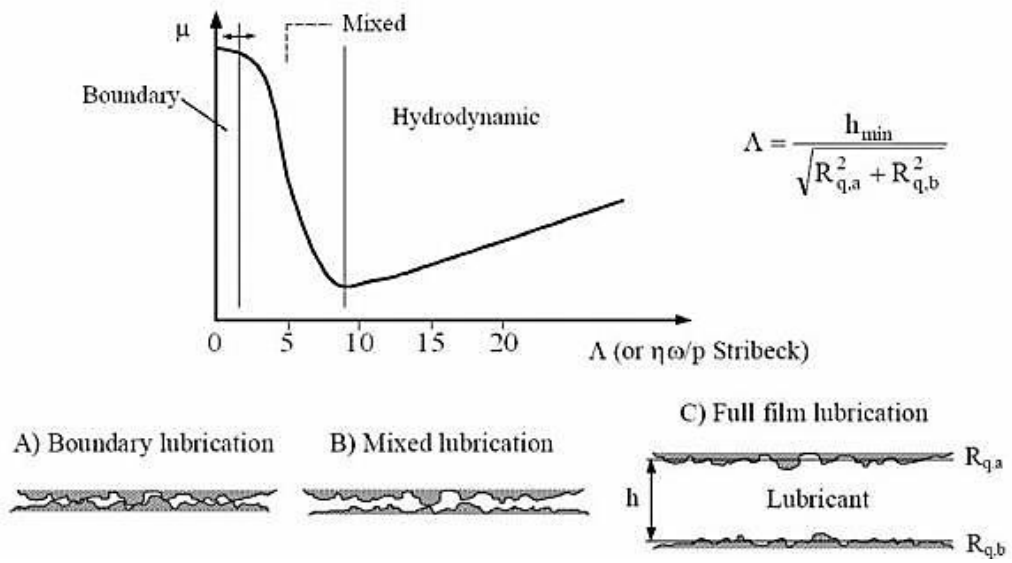


**Figure 4: Lubrication regimes, Stribeck curve [29].**

## 2.2. Hydrodynamic Lubrication

Hydrodynamic lubrication was first researched by Osborne Reynolds (1886) who observed that between a shaft and a journal bearing, the lubricant flows through a converging wedge. The gradual decrease in available flow volume in the gap slows the flow down and leads to a pressure build-up constituting a lifting ability of the bearing. Another justification for the development of pressure field is that otherwise there would be more lubricant entering the wedge than leaving it, something against the principle of mass conservation.

A better comprehension of the development of load-supporting pressures in hydrodynamic bearings can be gleaned by considering the physical conditions of geometry and motion required to develop hydrodynamic pressure.

Figure 5 shows velocity profiles for two parallel plane surfaces separated by a lubricating film. The plates are wide enough to accurately assume a two-dimensional flow without lateral (spanwise) components. The upper plate, often called the “rotor”, is moving with a constant velocity $u_a$ and the bottom plate, called the “stator” is stationary.

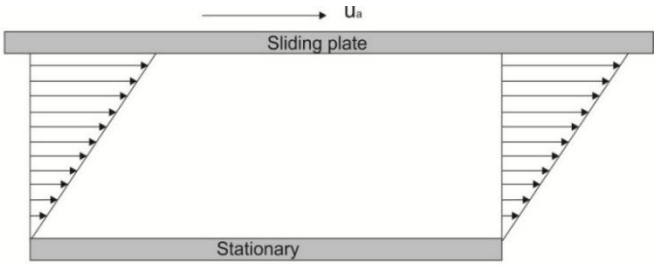


**Figure 5: Couette flow in parallel surfaces.**

The well-known "no slip" condition occurs at both surfaces. This states that the immediate layer of liquid next to a solid surface moves with the same tangential velocity as the solid surface itself. Therefore, the velocity varies linearly from zero, at the stator surface, to $u_a$ , at the rotor surface. This flow pattern, called Couette flow, is a result of the Newtonian rule of fluids, which states that the shear stress needed to deform a fluid is linearly proportional to shear strain (the derivative of fluid velocity in the direction perpendicular to the shear plane). The ratio of stress to strain is then the value of viscosity.

$$\tau = \mu \frac{\partial u}{\partial z} \tag{1}$$

The continuity theorem determines that the volume of fluid entering the channel per unit time is equal to that flowing out of it. However, the flow crossing the two boundaries (inlet, outlet) depends only on the velocity distribution at the boundary, and since velocity distributions are equal, the flow continuity requirement is satisfied without any pressure buildup. Therefore, since the ability of a lubricating film to support a load depends on pressure buildup in the channel, a slider bearing with parallel surfaces is not able to support any load. As a result, in rigid parallel bearing, application of vertical load would lead to lubricant being squeezed out, resulting in bearing collapse.

In Figure 6(a), the case of two nonparallel plates is considered. As before, the plate width is considered large enough so that flow in that direction is negligible. In this case, the volume of lubricant carried into the channel is greater than the volume that is discharged at the outlet boundary. Because flow continuity has to be satisfied, it can be concluded that there will be a relative increase in pressure across the channel. However, because of the pressure field and the fact that fluid flows from a high pressure region to a lower pressure area, lubricant will try to escape the area between the two pads, developing an additional flow pattern, called Poiseuille flow, see Figure 6(b). By superimposing the non-parallel Couette and Poiseuille flows we get Figure 6(c) which fairly represents the actual pressure and velocity profiles in a typical fixed-inclined slider bearing.

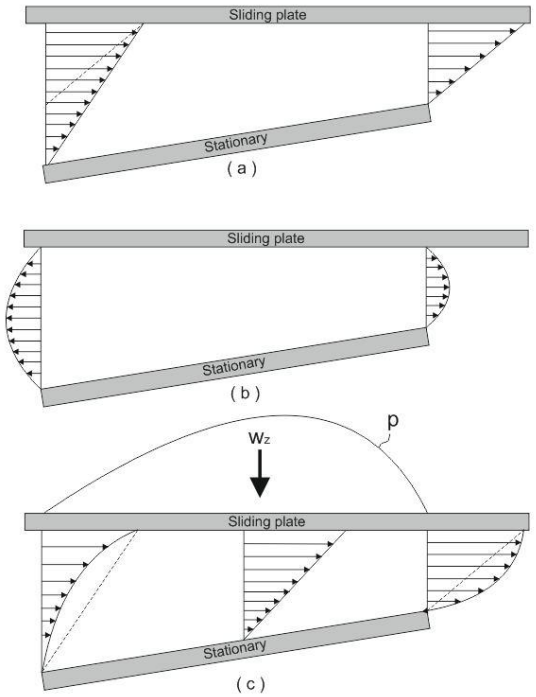


**Figure 6: Development of flow in hydrodynamic wedge.**

## 2.3. Mathematical Approach

### 2.3.1. Governing equations

In fluid mechanics, the Navier-Stokes equations are the basic governing equations of viscous flow and heat dissipation/conduction; they are an extension of the Euler equations for inviscid flow. Usually, the term “Navier-Stokes equations” refers to the following set of equations:

- three (3) time-dependent conservation of momentum equations
- one time-dependent continuity equation for conservation of mass, and
- one time-dependent conservation of energy equation

Fluid flow is caused by the action of externally applied forces. Common driving forces include pressure differences, gravity, shear, rotation and surface tension. Driving forces can be classified in two categories: surface forces, which are proportional to area, and body forces, which are proportional to volume. Gravitational, centrifugal, magnetic and/or electric fields may contribute to the total body forces, while the surface forces are due to the fluid static pressure as well as to viscous stresses (e.g. the shear force created by the motion of a rigid wall relative to the fluid).

***Momentum equations***

By applying the Newton's second law (conservation of momentum) for an arbitrary portion of the fluid, we get the general vector-form of Navier-Stokes equations:

$$\frac{\partial \rho \boldsymbol{V}}{\partial t} + \nabla \cdot (\rho \boldsymbol{V} \otimes \boldsymbol{V}) = -\nabla p + \nabla \tau + S \tag{2}$$

where:

$\boldsymbol{V}$**:** velocity vector

$\rho$: fluid density

$p$: pressure

$\tau$**:** total stress tensor

$S$: represents body forces (per unit volume) acting on the fluid

The vector field $S$ usually consists only of gravity, which is always present, but which in many cases may be neglected. In particular, this assumption is valid for hydrodynamic lubrication problems, therefore fluid motion is the outcome of a shear and a pressure field arising from the imposed motion.

For incompressible Newtonian fluid flows (Mach numbers much lower than the critical value of 0.3), the Eq.(2) is simplified to the following:

$$\rho(\frac{\partial \boldsymbol{V}}{\partial t} + \boldsymbol{V} \cdot \nabla \boldsymbol{V}) = -\nabla p + \nabla \tau \tag{3}$$

Eq.(3) can be split into three scalar equations, one for each spatial direction, with the velocity vector expanded as $\boldsymbol{V} = (u, v, w)$:

X direction:

$$\begin{aligned} \rho\left(\frac{\partial u}{\partial t} + u\frac{\partial u}{\partial x} + v\frac{\partial u}{\partial y} + w\frac{\partial u}{\partial z}\right) \\ = -\frac{\partial p}{\partial x} + 2\frac{\partial}{\partial x}\left(\mu\frac{\partial u}{\partial x}\right) + \frac{\partial}{\partial y}\left[\mu\left(\frac{\partial u}{\partial y} + \frac{\partial v}{\partial x}\right)\right] + \frac{\partial}{\partial z}\left[\mu\left(\frac{\partial u}{\partial z} + \frac{\partial w}{\partial x}\right)\right] \\ -\frac{2}{3}\frac{\partial}{\partial x}(\mu \nabla \boldsymbol{V}) \end{aligned} \tag{4}$$

Y direction:

$$\rho\left(\frac{\partial v}{\partial t}+u\frac{\partial v}{\partial x}+v\frac{\partial v}{\partial y}+w\frac{\partial v}{\partial z}\right) = -\frac{\partial p}{\partial y}+\frac{\partial}{\partial x}\left[\mu\left(\frac{\partial u}{\partial y}+\frac{\partial v}{\partial x}\right)\right]+2\frac{\partial}{\partial y}\left(\mu\frac{\partial v}{\partial y}\right)+\frac{\partial}{\partial z}\left[\mu\left(\frac{\partial v}{\partial z}+\frac{\partial w}{\partial y}\right)\right] - \frac{2}{3}\frac{\partial}{\partial y}(\mu\nabla\boldsymbol{V}) \quad (5)$$

Z direction:

$$\rho\left(\frac{\partial w}{\partial t}+u\frac{\partial w}{\partial x}+v\frac{\partial w}{\partial y}+w\frac{\partial w}{\partial z}\right) = -\frac{\partial p}{\partial z}+\frac{\partial}{\partial x}\left[\mu\left(\frac{\partial u}{\partial z}+\frac{\partial w}{\partial x}\right)\right]+\frac{\partial}{\partial y}\left[\mu\left(\frac{\partial v}{\partial z}+\frac{\partial w}{\partial y}\right)\right]+2\frac{\partial}{\partial z}\left(\mu\frac{\partial w}{\partial z}\right) - \frac{2}{3}\frac{\partial}{\partial z}(\mu\nabla\boldsymbol{V}) \quad (6)$$

***Continuity equation***

Regardless of the flow assumptions, a statement of the conservation of mass is also necessary. For fluid domains, this is achieved through the continuity equation, given in its most general form as:

$$\frac{\partial\rho}{\partial t}+\nabla(\rho V)\equiv\frac{\partial\rho}{\partial t}+\frac{\partial(\rho u)}{\partial x}+\frac{\partial(\rho v)}{\partial y}+\frac{\partial(\rho w)}{\partial z}=0 \quad (7)$$

Considering that density, ρ, is constant, as it is true in the case of incompressible flow, the mass continuity equation can be simplified to a volume continuity equation:

$$\frac{\partial u}{\partial x}+\frac{\partial v}{\partial y}+\frac{\partial w}{\partial z}=0 \quad (8)$$

***Energy equation***

Conservation of energy applied to a differential control volume in a moving fluid under steady conditions, means that the net rate at which energy enters a control volume, plus the rate at which heat is added, minus the rate at which work is done by the fluid, is equal to zero. After manipulation, the result can be rewritten as a thermal energy equation.

$$\rho c_{pf}\left(u\frac{\partial T}{\partial x}+v\frac{\partial T}{\partial y}+w\frac{\partial T}{\partial z}\right)=\lambda_f\left(\frac{\partial^2 T}{\partial x^2}+\frac{\partial^2 T}{\partial y^2}+\frac{\partial^2 T}{\partial z^2}\right)-\mu\Phi+q \quad (9)$$

where,

$\lambda_f$: thermal conductivity of the fluid

$c_{pf}$: specific heat capacity of the fluid

$q = 0$: heat generation

$\Phi$: viscous dissipation

$$\Phi = 2\left[\left(\frac{\partial u}{\partial x}\right)^{\mathbf{2}} + \left(\frac{\partial u}{\partial y}\right)^{2} + \left(\frac{\partial u}{\partial z}\right)^{2}\right] + \left(\frac{\partial u}{\partial y} + \frac{\partial v}{\partial x}\right)^{2} + \left(\frac{\partial v}{\partial z} + \frac{\partial w}{\partial y}\right)^{2} + \left(\frac{\partial w}{\partial x} + \frac{\partial u}{\partial z}\right)^{2} \quad (10)$$

The terms on the left-hand side account for the net rate at which thermal energy leaves the control volume due to bulk fluid motion, while the terms on the right-hand side account for net inflow of energy due to conduction, viscous dissipation, and heat generation. Viscous dissipation represents the net rate at which mechanical work is irreversibly converted to thermal energy due to viscous effects in the fluid. The heat generation term, $q$, characterizes conversion from other forms of energy (such as chemical, electrical, electromagnetic, or nuclear) to thermal energy.

***Heat transfer equations***

Heat is transported by means of conduction and convection. Heat conduction occurs mainly in all structural components of the bearing while in the fluid-solid interfaces, convection also exists due to the intensive flow.

Heat transfer due to conduction obeys Fourier's law, which, expressed for a three-dimension field, is:

$$q'' = -\lambda_s \nabla \boldsymbol{T} \equiv -\lambda_s \left(\frac{\partial T}{\partial x} + \frac{\partial T}{\partial y} + \frac{\partial T}{\partial z}\right) \quad (11)$$

where,

$q$": heat flux

$\lambda_s$: solid thermal conductivity

Respectively, convectional heat transfer can be calculated by:

$$q'' = a(T_{wall} - T_{bulk}) \quad (12)$$

Convection coefficient a $(\mathrm{W/m^2K})$ depends on the relation between thicknesses of the velocity and temperature boundary layers (Prandtl number) and the type of flow (laminar or turbulent) as described by the Reynolds number.

$$\Pr = \frac{\nu}{a} = \frac{c_P \mu}{\lambda} \sim \frac{\nu\text{iscous diffusion rate}}{\text{thermal diffusion rate}} \, , Re = \frac{\rho U h}{\nu} \sim \frac{\text{inertial forces}}{\text{viscous forces}} \tag{13}$$

***State equations***

The temperature dependence of liquid viscosity is typically represented by simplified mathematical or empirical models which are valid over limited temperature ranges and for selected fluids. The simplest model is based on an exponential equation and it was first proposed by Reynolds in 1886:

$$\mu(T) = \mu_0 \exp(-bT) \tag{14}$$

where $\mu_0, b$ are coefficients.

A more accurate relationship of viscosity to temperature for petroleum based oils and hydrocarbons is given by the McCoull-Walther equation:

$$loglog(\nu + 0.6) = A - Blog(T) \tag{15}$$

Where $\nu$ is the kinematic viscosity and both A and B are constants for a given liquid. The minus sign in the second term on the right side of the equation reveals that higher temperatures result in lower viscosities. The absolute or dynamic viscosity is then obtained by multiplying the kinetic viscosity of a fluid with its mass density:

$$\mu = \nu \cdot \rho = (10^{10^{A-Blog(T)}} - 0.6) \cdot \rho \tag{16}$$

Finally, in regards to density, the effect of temperature and pressure for liquids is small, so the density is considered to be constant for all the hydrodynamic lubrication problems considered in the present thesis.

$$\rho(p, T) \cong const \tag{17}$$

***Summary of governing equations***

Eqs.(4)-(6),(8)-(9),(16) comprise a system of six equations with six unknowns $(u, v, w, p, \mu, T)$, which fully describe the problem of hydrodynamic lubrication. Once the velocity field is solved through the Navier–Stokes equations, other quantities of physical significance may be derived. The values of flow rate, pressure or drag force are usually of great interest.

## 2.3.2. Reynolds approximation

In almost every real problem of fluid flow, the corresponding Navier–Stokes equations are nonlinear partial differential equations, which are generally very difficult or

impossible to solve. Even if we consider the simple case of laminar flow of an incompressible fluid, nonlinearity exists due to convective acceleration, i.e., acceleration associated with the change in velocity over position.

However in some cases, such as for one-dimensional flow, the equations can be simplified to linear equations leading to a straight-forward solution. Osborne Reynolds achieved a closed-form solution to the problem of hydrodynamic lubrication by retaining only the lowest order terms from the Navier-Stokes equations coupled with the continuity equation. However he was forced to make several simplifications, the most important of which are the following:

i. **Laminar and incompressible flow assumption**. Usually correct except for large bearings at high rotational speeds.
ii. **Zero pressure gradient through the oil film thickness**. This assumption is quite correct since the film thickness is of the order of magnitude of few micrometers in most cases. However, this restriction forbids modeling bearings with geometric features such as those studied in the present work. Phenomena such as oil stagnation and changes in flow velocity inside a recess create inertial pressure changes which are neglected using the Reynolds theory.
iii. **Infinite width approximation**. Flow components in the third dimension are neglected. This is valid when considering the flow at a mean bearing diameter but it is hardly correct when modeling the full 3D problem since side leakages cannot be taken into account. Assuming the same flow characteristics for the whole width leads to substantial overestimation of load carrying capacity.
iv. **Isothermal flow**. One of the most significant disadvantages of the Reynolds equation solution is the assumption of constant temperature in the oil film. In a real bearing there are temperature variations that have a great influence on the viscosity of the oil. Due to this effect, the load carrying capacity of the bearing calculated with the use of Reynolds equation is overestimated.
v. **Calculation without influence of the pad and runner deformations**. The bearing surfaces are assumed to be perfectly flat and rigid without taking into account deformations of the bearing elements caused by the thermal and pressure fields. This assumption becomes less valid in large scale bearings.

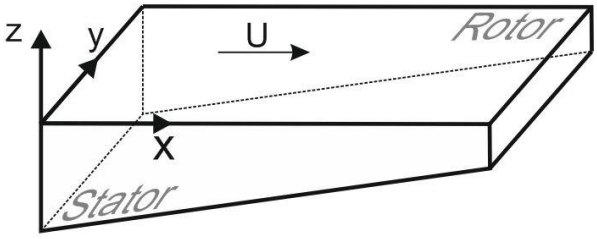


**Figure 7: Sketch of a typical 3-d slider; depiction of the coordinate system used for calculations.**

As mentioned earlier, thrust bearings consist of fixed or tilting sector-shaped pads. The Reynolds equation in such bearings is usually written in cylindrical coordinates. However, since film thickness is small compared to the radius of curvature in such bearings, the Reynolds equation can be written in Cartesian coordinates without significant loss of accuracy. A typical fluid geometry of a thrust bearing, and the corresponding reference coordinate system are presented in Figure 7. Therefore, taking into account assumptions (i)-(v) above, the Navier-Stokes equations may be written as:

X-direction:

$$\rho\left(u\frac{\partial u}{\partial x}+w\frac{\partial u}{\partial z}\right)=-\frac{\partial p}{\partial x}+\mu\left(\frac{\partial^2 u}{\partial x^2}+\frac{\partial^2 u}{\partial z^2}\right) \tag{18}$$

Z-direction:

$$\rho\left(u\frac{\partial w}{\partial x}+w\frac{\partial w}{\partial z}\right)=-\frac{\partial p}{\partial z}+\mu\left(\frac{\partial^2 w}{\partial x^2}+\frac{\partial^2 w}{\partial z^2}\right) \tag{19}$$

In order to get the above equations into dimensionless form we use the following characteristic parameters:

- $L_x$ : Length in x-direction $(\mathrm{m})$
- $L_z$ : Length in z-direction $(\mathrm{m})$
- $u_0$ : Velocity in x-direction $(\mathrm{m/s})$
- $w_0$ : Velocity in z-direction $(\mathrm{m/s})$
- $\rho_0$ : Density $(\mathrm{kg/m^3})$
- $\eta_0$ : Dynamic viscosity $(\mathrm{Ns/m^2})$
- $p_0$ : Pressure $(\mathrm{Pa})$

By using the above characteristic parameters the non-dimensional parameters are defined:

$$x^* = \frac{x}{L_x}, \quad z^* = \frac{z}{L_z}, \quad u^* = \frac{u}{u_0}, \quad w^* = \frac{L_x}{L_z} \cdot \frac{w}{u_0}$$
$$\rho^* = \frac{\rho}{\rho_0}, \quad \mu^* = \frac{\mu}{\mu_0}, \quad p^* = \frac{p}{p_0} \tag{20}$$

In order to get the same modified Reynolds number in the z-direction as in the x-direction, the velocity $w^*$ is scaled as above. Substituting the dimensionless numbers into (18) gives:

$$\frac{1}{L_x} u_0^2 u^* \frac{\partial u^*}{\partial x^*} + \frac{1}{L_x} u_0^2 w^* \frac{\partial u^*}{\partial z^*} = -\frac{1}{L_x} \frac{p_0}{\rho_0} \frac{\partial p^*}{\partial x^*} \frac{1}{\rho^*} + \frac{\mu_0}{\rho_0} \left( \frac{u_0}{L_x^2} \frac{\partial^2 u^*}{\partial x^{*2}} + \frac{u_0}{L_z^2} \frac{\partial^2 u^*}{\partial z^{*2}} \right) \frac{\mu^*}{\rho^*} \tag{21}$$

Rearranging and multiplying by $L_x/u_0^2$ becomes

$$u^* \frac{\partial u^*}{\partial x^*} + w^* \frac{\partial u^*}{\partial z^*} = -\frac{p_0}{\rho_0} \frac{1}{u_0^2} \frac{\partial p^*}{\partial x^*} \frac{1}{\rho^*} + \frac{\mu_0 L_x}{\rho_0 u_0 L_z^2} \left[ \left( \frac{L_z}{L_x} \right)^2 \frac{\partial^2 u^*}{\partial x^{*2}} + \frac{\partial^2 u^*}{\partial z^{*2}} \right] \frac{\mu^*}{\rho^*} \tag{22}$$

Where the inverted Reynolds number appears:

$$1/Re = \frac{\mu_0 L_x}{\rho_0 u_0 L_z^2} \tag{23}$$

In addition, by defining the reference pressure as follows:

$$p_0 = \mu_0 u_0 L_x / L_z^2 \tag{24}$$

we get, a non-dimensional form of the Navier-Stokes equation in the x-direction:

$$u^* \frac{\partial u^*}{\partial x^*} + w^* \frac{\partial u^*}{\partial z^*} = -\frac{1}{Re^*} \frac{\partial p^*}{\partial x^*} \frac{1}{\rho^*} + \frac{1}{Re^*} \left[ \left( \frac{L_z}{L_x} \right)^2 \frac{\partial^2 u^*}{\partial x^{*2}} + \frac{\partial^2 u^*}{\partial z^{*2}} \right] \frac{\mu^*}{\rho^*} \tag{25}$$

In a similar way, the Eq.(18) yields:

$$u^* \frac{\partial v^*}{\partial x^*} + w^* \frac{\partial w^*}{\partial y^*} = -\frac{1}{Re^*} \left( \frac{L_z}{L_x} \right)^2 \frac{\partial p^*}{\partial z^*} \frac{1}{\rho^*} + \frac{1}{Re^*} \left[ \left( \frac{L_z}{L_x} \right)^2 \frac{\partial^2 w^*}{\partial x^{*2}} + \frac{\partial^2 w^*}{\partial z^{*2}} \right] \frac{\mu^*}{\rho^*} \tag{26}$$

From assumption (iii), $L_z \ll L_x$, the term $(L_z/L_x)^2$ can be neglected. Thus, Eq.(25) can be rewritten as:

$$Re^* u^* \frac{\partial u^*}{\partial x^*} + Re^* w^* \frac{\partial u^*}{\partial z^*} = -\frac{\partial p^*}{\partial x^*} \frac{1}{\rho^*} + \frac{\partial^2 u^*}{\partial z^{*2}} \frac{\mu^*}{\rho^*} \tag{27}$$

Fluid flow in lubricating contacts is generally a creeping flow, therefore inertial phenomena which are expressed through the terms multiplied with the Reynolds number in Eq.(27), can be neglected. This yields:

$$\frac{\partial p^*}{\partial x^*} = \mu^* \frac{\partial^2 u^*}{\partial z^{*2}} \tag{28}$$

Integrating Eq.(28) twice with respect to z we get:

$$u = \frac{1}{2\mu}\frac{\partial p}{\partial x} z^2 + Az + B \tag{29}$$

$A$ , $B$ are constants and Eq.(29) can be solved by applying appropriate boundary conditions. For the case of a hydrodynamic wedge we have:

$$u = U_0 \text{ at } \quad z = 0 \qquad \text{(rotor)}$$

$$u = 0 \quad \text{at} \quad z = -h(x) \qquad \text{(stator)}$$

Substituting,

$$A = \frac{U_0}{h} + \frac{h}{2\mu}\frac{\partial p}{\partial x}, \qquad B = U_0$$

therefore velocity can be calculated as:

$$u = \frac{(z^2 - zh)}{2\mu}\frac{\partial p}{\partial x} + \frac{U_0 z}{h} + U_0 \tag{30}$$

Eq.(30) combined with Eq.(1):

$$\tau = \frac{\partial p}{\partial x}\left(z - \frac{h}{2}\right) + \frac{U_0 \mu}{h} \tag{31}$$

The continuity equation for the one-dimensional slider states that:

$$\frac{\partial u}{\partial x} + \frac{\partial w}{\partial z} = 0 \tag{32}$$

Integrating Eq.(32) with respect to z we get:

$$w_0^h = -\int_0^{-h(x)} \frac{\partial u}{\partial x} dz \tag{33}$$

By substituting (30) to (33), interchanging the differentiation and integrating, we get:

$$(w_h - w_0) = -\frac{\partial}{\partial x}\left[\frac{1}{2\mu}\frac{\partial p}{\partial x}\int_0^{-h(x)}(z^2 - zh)dz\right] - \frac{\partial}{\partial x}\left[\int_0^{-h(x)}\frac{z}{h}U_0 dz\right]$$
$$= -\frac{\partial}{\partial x}\left[\frac{1}{2\mu}\frac{\partial p}{\partial x}\left(\frac{h^3}{3} - \frac{h^2 h}{2}\right)\right] - \frac{\partial}{\partial x}\left[\left(\frac{U_0}{h}\frac{h^2}{2}\right)\right] \quad (34)$$
$$= \frac{\partial}{\partial x}\left(\frac{h^3}{12\mu}\frac{\partial p}{\partial x}\right) - \frac{U_0}{2}\frac{\partial h}{\partial x}$$

For steady-state conditions, $\partial \mathrm{h}/\,\partial \mathrm{t} = 0$, the left-hand term $(\mathrm{w_h} - \mathrm{w_0}) = \partial \mathrm{h}/\,\partial \mathrm{t}$ is zero, hence, Eq.(34) yields:

$$\frac{\partial}{\partial x}\left(h^3\frac{\partial p}{\partial x}\right) = 6\mu U_0\frac{\partial h}{\partial x} \quad (35)$$

Eq.(35) is the most common form of the Reynolds equation. In smooth, fixed converging bearings, film thickness is a linearly decreasing function of bearing length. Film thickness is usually expressed in terms of convergence ratio k which is defined as $k = (h_1 - h_0)/h_0$. Therefore, h can be calculated as:

$$h = h(x) = h_0 + \frac{(h_1 - h_0)}{L}\cdot x = h_0 \cdot (1 + \frac{k \cdot x}{L}) \quad (36)$$

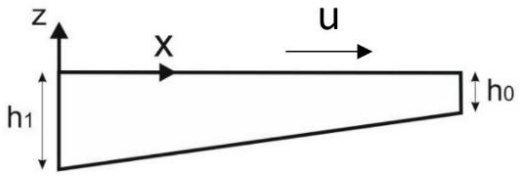


**Figure 8: Sketch of a 2-d slider; depiction of the coordinate system used for calculations.**

For a given film geometry, the pressure distribution over the bearing length can be calculated as:

$$p(x) = \frac{6\mu U_0 L}{k h_0}\left(-\frac{1}{h} + \frac{h_0}{h^2}\cdot\frac{k+1}{k+2} + \frac{1}{h_0(k+2)}\right) \quad (37)$$

The load which can be supported by a certain film geometry is calculated as:

$$W = \int_0^B \int_0^L p\,dx\,dy \quad (38)$$

Utilizing the Eq.(37) the load per unit width of a bearing of infinite width can be calculated with the aid of Eq.(39):

$$\frac{W}{B} = \frac{6U_0\mu L^2}{k^2 h_0^2}\left(-ln(k+1) + \frac{2k}{k+2}\right) \tag{39}$$

During the operation of a thrust bearing, apart from axial (thrust) forces, friction forces inevitably arise. These forces resist the rotor motion and have a great impact on the bearing efficiency factor. The resultant friction force is the integral of viscous shear stresses over the bearing surface.

$$F = \int_0^B \int_0^L \tau dx \tag{40}$$

Based on Reynolds theory, the friction per unit width can be easily calculated by the following equation:

$$\frac{F}{B} = \frac{U_0\mu L}{h_0}\left(\frac{6}{k+2} - \frac{4\,ln(k+1)}{k}\right) \tag{41}$$

Combining Eqs.(39) and (41) friction coefficient, in bearings of infinite width, can be calculated by the following equation:

$$f = \frac{F}{W} \xrightarrow{Reynolds} f = \frac{kh_0}{L}\left[\frac{3k - 2(k+2)\,ln(k+1)}{6k - 3(k+2)\,ln(k+1)}\right] \tag{42}$$

A noteworthy observation arises from the last equation, where it is clear that the friction coefficient is independent from operational speed and viscosity. That means that for a desired value of minimum film thickness, $h_0$, it is possible to optimize performance by finding the optimum value of the convergence ratio. It can be easily proven that a minimum value of friction coefficient is attained for a value of convergence ratio equal to $k = 1.55$ while load capacity is maximized for $k = 1.2$. This behavior is depicted in the diagram of Figure 9.

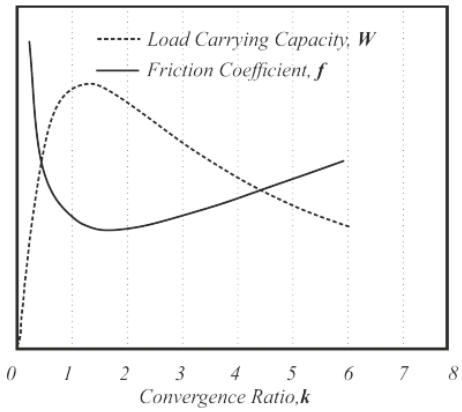


**Figure 9: Friction coefficient and load capacity versus convergence ratio for bearings of infinite width.[30]**

## 2.4. Design and performance parameters

### *Geometry*

A thrust bearing normally consists of a number of identical pads ($N_p$) which are assembled in a circular arrangement (see Figure 10(a)). Between pads there are deep recesses that ensure the supply of cool oil close to the heated areas. These grooves usually extend across the entire width of the bearing; fresh oil is normally fed through the entrance at the inner radius region. Pad width ($B$) is expressed as the distance between the outer ($R_o$) and the inner radius ($R_i$) at each pad; together with pad length ($L_{pad}$), these are the key parameters affecting the active area ($A$) of the pad (Figure 10(b)). The specific (mean) pressure that develops on that area indicates the operational level and for hydrodynamic thrust bearings and typically ranges between 0.5 and 3.0 MPa.

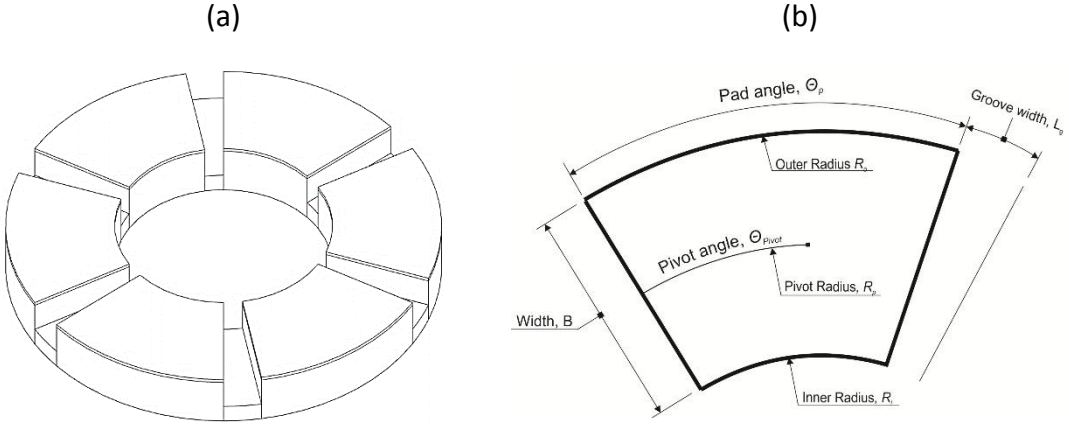


**Figure 10: (a) Typical arrangement of a thrust bearing with six pads, (b) Principal dimensions of a bearing pad.**

### *Pivot location*

In tilting or pivoting pad thrust bearings, the pivot location has a significant effect on the bearing performance. Circumferential position is usually expressed as a percentage of the pad arc length measured from the leading edge of the pad while its radial position is determined as percentage of pad width measured from the inner radius. Usually, the pivot point is located at the pad mid-sector ($R_P = R_{in} + 0.5B$) while it has been proven [31] that at a radial position, 55-58% of the bearing width (measured from $R_i$) the radial tilt angle is zeroed. In the longitudinal (circumferential) direction of the pad, pivot location is usually about 60% of the pad length ( $\Theta_{Pivot} = 0.6\Theta_P$) beyond the leading edge of the pad, for optimal performance. However, a location of the pivot of 70-75% of the pad length beyond the leading edge was found to give the highest possible loads and lowest bearing metal temperatures [32].

A centrally located pivot point provides manufacturing simplicity and enables operation in both directions of rotation, but according to the Reynolds theory (and whenever the assumption of rigid bodies is made) such bearings have zero load carrying capacity. This results from the fact that, relative to the center of the pad, an asymmetric pressure profile would impose a moment about the pivot, tending to align the pad parallel to the runner. A parallel pad generates no hydrodynamic pressure, thus making the operation of such an arrangement impossible. However, in real operation, centrally pivoted bearings operate without problems since thermal and elastic deformations lead to appropriate wedge film geometries for pressure development. The excessive deformation (crowning) of a pad can be controlled in different ways such as increasing the pad thickness, using multi-layered structures or selecting a stronger backing material.

***Materials***

From a manufacturing standpoint, the last crucial parameters are the bearings materials and their thickness. The maximum pressure that is developed at the bearing surfaces is usually less than 5 MPa and is not generally large enough to cause significant bending moments, compared to the material strength. However, the thermal load due to friction is significant, and for this reason the selection of materials with appropriate thermal properties is essential. Typically, temperatures on the surface of the stationary pad, are higher than those on the rotor surface. This occurs mainly because, at steady-state operation, stationary pads are constantly exposed the same flow characteristics while, on the rotating surface, each point faces different conditions at every moment since it periodically passes over cooling grooves which maintain the whole body at a cooler temperature.

For better heat conduction, but also because dry contact is always a possibility in hydrodynamic bearings, a thin layer of Babbitt metal is commonly used on the surface of each pad. Babbitt metal is a metal matrix composite which is characterized by resistance to scraping thanks to its self-lubricating properties. In case of contact, the soft Babbitt layer prevents massive damage to the rotor surface. Furthermore, even in the case of harsh lubricating conditions and possible damage, the replacement of the pad coating is an economically preferable solution to fixing a possible damage of the rotor itself.

Recent research in the area of advanced composite materials has attempted to examine whether polymers can be considered appropriate replacements for the Babbitt metal. It has been observed that certain polymers (Polytetrafluoroethylene-PTFE, Polyetheretherketone-PEEK) exhibit lower friction coefficients, wider temperature operating ranges and higher resistance against lubrication oil contaminants than metals. In addition, the application of a PTFE layer on the surface of thrust bearing pads proved

to give a more uniform pressure distribution and lower maximum pressure due to the lower value of Young's modulus for PTFE compared to Babbitt [33]. Another important advantage is the PTFE's ability to manage the expected convexity of the pad observed due to thermal stress, at the design stage, by manufacturing, for example, pads with prefabricated opposite convexity.

***Oil Properties***

The primary function of lubricating oils is to provide a continuous layer of fluid between surfaces in relative motion, in order to reduce friction and prevent wear. In addition, they are used for heat extraction and for preventing oxidation, whereas, with suitable additives, they can assist in debris removal preventing their own contamination. In lubrication, viscosity is the fluid property which has the most crucial role. Different oils exhibit different viscosities and the thickness of the generated lubricating film is proportional to that viscosity. A lubricant with high viscosity can provide thicker films ensuring increased safety against contact. However, this does not mean that the oil with the higher viscosity is the most appropriate for all applications. More viscous oils require higher energy levels in order to be sheared (to flow) while the generated heat due to friction is similarly high, resulting in a substantial increase in temperature. In addition, at high speeds, lubricants with very high viscosity cannot manage to penetrate into the hydrodynamic wedge leading to impaired lubrication with all that this entails. Therefore, as in any engineering application, the viscosity of the lubricant must be properly selected so as to provide optimal performance for the anticipated operating parameters.

***Feeding oil supply rate***

Total oil feed to the bearing should satisfy three requirements. There must be sufficient flow into the hydrodynamic wedge to fully separate the surfaces, to match the side leakages from each sector and to maintain temperatures at the desired levels during operation. If an excess of lubricant is supplied, significant amounts of churning losses develop due to unnecessary oil streams. Different designs have introduced direct injection of cold and clean oil at the entrance of the channel instead of the typical flooded lubrication. In that way, oil enters and exits its operating region without further mixing with other circulation streams and backflows. However, their effectiveness is limited in low-speed applications.

***Rotating Speed***

Fluid velocity affects flow properties in a number of ways. At low enough velocities, the inertia of the fluid may be ignored and we have creeping flow. As the speed is increased, inertia becomes more important, but each fluid particle follows a smooth trajectory; the

flow is then said to be laminar. Further increases in speed may lead to instability that eventually produces a more random type of flow called turbulent flow which, in general, is not desirable. Turbulent flow may be observed in the groove region of the bearing, however it has been proven experimentally that flow in the groove region can be considered laminar for Re<1000 [34].

## 2.5. Hydrophobicity

Recently, certain surfaces have been studied, which exhibit an incredibly low friction coefficient with liquids flowing over them, and as such prove very difficult to wet. A typical example in nature can be found in the leaves of a lotus plant, on which droplets of water move without leaving any trace. Such surfaces are called hydrophobic. Today, it is possible, to artificially create hydrophobic surfaces in a laboratory, and various industrial applications have been proposed (e.g. ship hull coatings). The key is creating a very smooth-but with the appropriate nano-roughness-surface such that air molecules become trapped in the microscopic grooves between the surface and the fluid, drastically decreasing shear stresses in the fluid-solid interface.

The hydrophobicity of a material can be characterized by the geometry of a drop of liquid on its surface. The three-phase boundary of the droplet is where solid, liquid and air meet and can be visualized using Figure 11. The angle formed by the droplet and surface at this point is known as the contact angle, and is used to categorize the surface as hydrophilic, hydrophobic and super-hydrophobic. If the droplet forms a sphere that barely touches the surface with the contact angle '$\theta_c$' being more than 90 degrees then the surface is water-repelling or hydrophobic, whereas contact angle values larger than 150$^o$ correspond to super-hydrophobic surface characteristics.

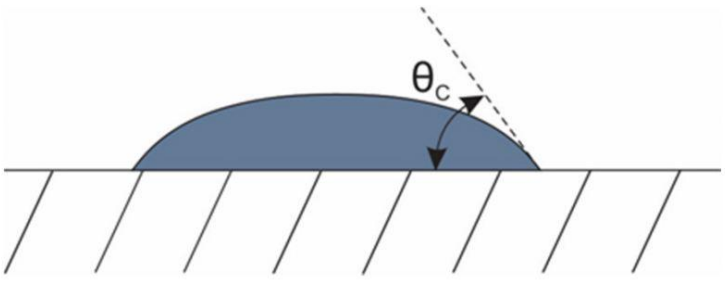


**Figure 11: Contact angle formed by a liquid droplet on a solid surface. [35]**

Most recent research on hydrophobicity has shown that the phenomenon is mainly a matter of surface chemistry, determined by the properties of the materials used. As already mentioned, aside from naturally occurring hydrophobic surfaces, manufactured surfaces can also be created. Various processes are used for this such as machining the

surface to create micro or nano-scale geometric patterns which are then filled with hydrophobic compounds, dispersing micrometric particles in a gel or resin which is then applied to the surface, depositing nano-fibres on the surface, or chemically attacking surfaces with appropriate acids.

For hydrophobic surfaces, the basic assumption of fluid mechanics, known as the no-slip condition, is no longer universally valid. Here, the velocity of the moving surface and the fluid velocity at the boundary differ, and various mathematical models have been developed to express this case. In the present study, the modified Navier model, which was introduced in [36], is utilized. This model relates the velocity at which the liquid slips to the shear stress at the liquid-solid interface. Thus, it states that if local shear stress exceeds a threshold value, the slip condition occurs and the velocity is calculated as follows:

$$u_s = \begin{cases} 0, & \tau < \tau_{cr} \\ (\tau - \tau_{cr}) \cdot \dfrac{b}{\eta}, & \tau \geq \tau_{cr} \end{cases} \tag{43}$$

Slip length, $b$, is a property of a surface, indicating how slippery the surface is when interacting with a particular fluid. It is defined as the frictious distance under the surface of the fixed boundary where the velocity extrapolates to zero, assuming linear reduction at the same rate as that on the surface of the boundary (Figure 12). Non dimensional slip length, $b^*$, can be defined in terms of a characteristic film thickness of the bearing and can be calculated using Eq.(44)

$$b = b^* \cdot H_{ref} \tag{44}$$

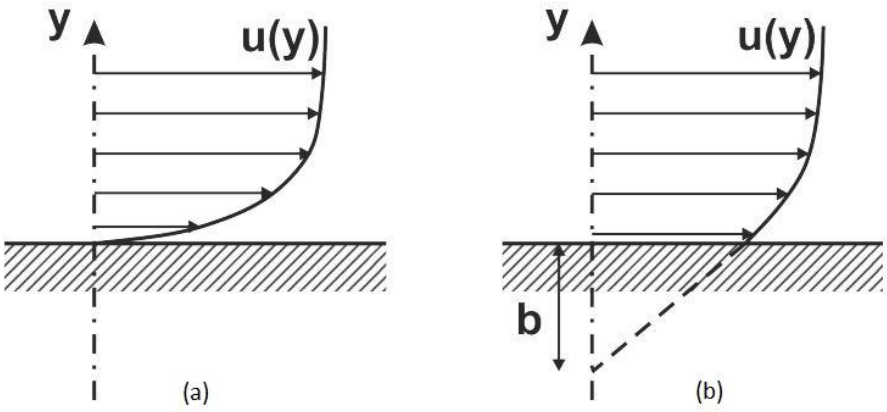


**Figure 12: Velocity profile near the fluid-solid interface. (a) no-slip conditions, (b) slip conditions with slip length b.**

# 3. Numerical modelling

## 3.1. Computational fluid dynamics

As demonstrated in Chapter 2 of the present work, the governing equations in fluid mechanics are solvable for only a limited number of flows. The known solutions are very useful in helping to understand fluid flows but can rarely be used in engineering analysis or design. The engineer is forced to use different approaches, with the most common being the simplification of the equations used. This is based on a combination of approximations and dimensional analysis which lead to non-dimensional representative parameters such as the Reynolds number, the Froude number etc. Having reduced the number of independent parameters (in some cases down to one), the researcher is able to perform experiments even on scale models, under the condition of geometric similarity. However, many flows require several dimensionless parameters for their description, and it may be impossible to set up a scaled experiment. A common example is the flow around a ship versus the flow around its scaled model. Matching both Reynolds and Froude numbers of the prototype and model is most often impossible.

Even if a good match can be made between the original and simulated phenomena, experiments may be too expensive and time consuming in order to make detailed studies while the measured data is generally limited to a few measuring locations. That means that essential information like whether flow separation occurs or whether a temperature exceeds some limit is not easily obtained. As technological improvement requires more careful and optimized designs, and high-tech applications demand detailed prediction of flows, experimental development will be even more impracticable in the future.

The rapid growth of computing power in the last half century has resulted in the rise of a new research field, known as Computational Fluid Dynamics. CFD constitutes a new approach between theory and experiment, in the study of the fluid dynamics discipline. With the aid of applied mathematics, computers may approximate the solution of partial differential equations using numerical methods. To obtain a solution numerically, a discretization method should be used so that the differential equations are approximated by a system of algebraic equations which are adequately simple to be solved by a computer. The approximations are applied to small domains in space and/or time so the numerical solution provides results at discrete locations in space and time.

As already stated, numerical results provided by CFD methods are only approximations of complex physical phenomena. Differences between computed and experimental results do always exist, and are caused by errors of the numerical process, which can be classified into the following categories:

- Errors due to approximations or idealizations in modeling the problem. Typical examples are found in the modeling of complex phenomena such as turbulence, combustion and multiphase flows. Regarding the present work the Navier-Stokes equations for incompressible, Newtonian fluids can be solved accurately. However, other simplifications related to thermal effects and elastic deformations have been taken into account and they will be mentioned hereafter.
- Discretization errors. They can be reduced by increasing the number of elements, by using more accurate (higher-order) interpolation schemes, or by applying the approximations to smaller regions. Both lead to more time-consuming solutions so that a compromise is usually needed (refer to Section 3.4).
- Errors due to insufficient iterations. In solving the discretized equations, iterative methods are usually used. If convergence is not reached, the attained solution is not accurate. Usually, the number of iterations is adjusted so that some representative operating parameters of the problem (e.g. max/average temperature, max/average pressure etc.) reach certain steady values.

## 3.2. Model definition

The simplest level of modeling a hydrodynamic lubrication problem is modeling isothermal flow across a two dimensional channel with appropriate boundary conditions (stator modeled as stationary wall and rotor modeled as moving wall with constant velocity). This modeling procedure is called Hydrodynamic (HD) and can be extended to 3-D HD if the channel (finite) width is also taken account. More realistic models are capable of taking into account thermal effects (heat dissipation and transfer) and fluids whose viscosity is temperature dependent. The corresponding simulations are called Thermohydrodynamic (THD) simulations, and depending on the flow domain they can be two-dimensional (2D-THD) or three dimensional (3D-THD). Even more sophisticated codes are capable of including thermal distortion and elastic deformation of the interacting bodies. The corresponding simulations are called Thermoelastohydrodynamic (TEHD) simulations, and the results of such models can approach reality with great accuracy. However, the computational cost of such complex models is prohibitively high for early-stage research effects such as feasibility studies, optimization processes, etc.

In the present study, three-dimensional thermohydrodynamic (THD) analyses of tilting pad thrust bearings are presented, assuming that the bearings pad and collar are rigid, non-deformable bodies. To this end, the system of equations presented in Section 2.3 are solved with the CFD code ANSYS CFX.

Heat phenomena taken into account are:

- ✓ Rise in temperature caused by viscous flow
- ✓ Heat transfer between oil and solids (pad and collar)
- ✓ Heat exchange with the environment
- ✓ Mixing oil effect at grooves

***Geometry***

For the purposes of the present study a three-dimensional parametric CAD model of a pivoted thrust bearing has been generated utilizing the Autodesk Inventor software. The model includes the fluid domain as well as the solid bodies of the pad and the rotor. Between the solid parts no structural link exists, so therefore the load is externally applied to the rotor is transferred to the supporting pad through a film lubricating oil.

The thrust bearing is assumed to operate without misalignment, while the runner sliding surface is parallel to the bearing plane. Those assumptions enable modeling of a single pad, thus substantially reducing the computational cost. At the same time, only the part of the rotor which is over the pad at any given moment has been included in the model. The basic geometric parameters of the model correspond to those studied by Glavatskih et al. [39] and are presented in Table 1:

| **Basic Geometry** | |
|---|---|
| Number of pads, $N_p$ | 6 |
| Outer diameter, $D_o$ | 228.6 mm |
| Inner diameter, $D_i$ | 114.3 mm |
| Pad angle, $\Theta_P$ | 50 degrees |
| Pivot circumferential position, $\Theta_{Pivot}$ | 60% relative to leading edge |
| Pivot radius, $R_{Pivot}$ | 50% relative to inner radius (85.725mm) |
| Pad thickness, $t_{pad}$ | 28.58 mm |
| Collar thickness, $t_{collar}$ | 51 mm |

**Table 1: Basic geometric characteristics of the tilting pad bearing of the present study.**

***Oil and Solid Properties***

In addition to the geometric characteristics, the thermo-physical properties of the lubricating oil and the solids are equally important for accurate simulations. These properties are presented in Table 2, and are kept the same for all the simulations carried out in the present study.

| Lubricant – VG 46 | |
|---|---|
| Viscosity law | McCoull and Walther |
| Dynamic viscosity at 40°C, $\mu_{40}$ | 0.037 Pa.s |
| Dynamic viscosity at 100°C, $\mu_{100}$ | 0.056 Pa.s |
| Density, $\rho$ | 855 kg/m$^3$ |
| Thermal conductivity, $\lambda_f$ | 0.13 W/m.K |
| Heat capacity, $c_{pf}$ | 2035 J/(kg.K) |
| Feeding oil temperature, $T_{feed}$ | 50°C |
| Feeding oil flow rate, $Q_{feed}$ | 0.00025 m$^3$/s |
| **Solids** | |
| Thermal conductivity, $\lambda_s$ | 47 W/(m.K) |
| Heat capacity, $c_{ps}$ | 434 J/(kg.K) |

**Table 2: Thermophysical properties of the lubricating oil and of the bearing solid bodies (rotor and stator).**

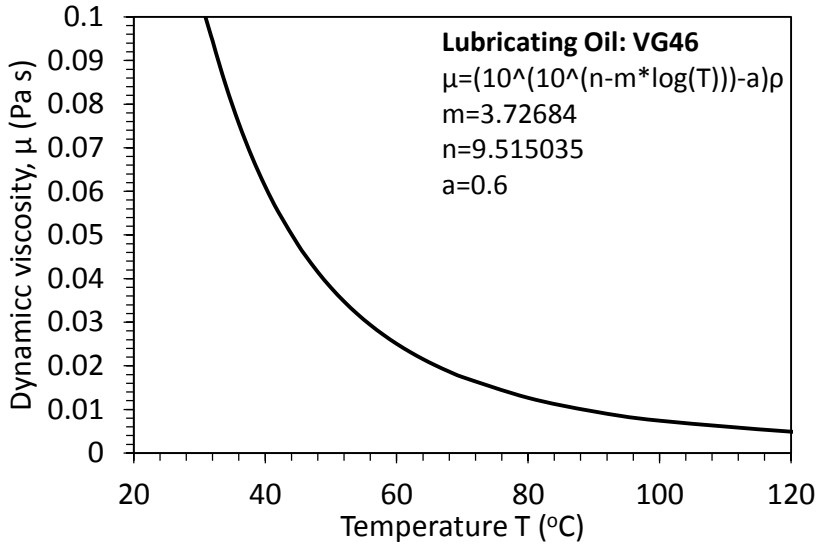


**Figure 13: Temperature dependence of VG46 viscosity, based on the McCoull and Walther model.**

### *Boundary Conditions*

Boundary conditions define the flow conditions at the boundaries of the domain, either with a solid or fluid. The solid bodies of the pad and the rotor both consist of 6 facets. The facets in contact with fluid are set as walls, meaning that those limits are impermeable by fluid particles, allowing nonetheless heat exchange in the fluid-solid interface. Furthermore, for non-hydrophobic surfaces, the well-known no-slip condition is employed, which equalizes fluid and solid velocities in the fluid-solid interface. For hydrophobic boundaries, fluid velocities can be calculated using Eq.(43) of Section 2.5.

The surface heat transfer coefficients of solid surfaces at the boundaries of the computational domain are dependent upon the overall design of a bearing, including the size and depth of cavities behind the pads, operating conditions, housing temperatures etc. Therefore, it is possible only to roughly estimate surface heat transfer coefficients from simpler models.

Here, different heat transfer coefficients were assumed according to the specific location of each surface. In particular, heat transfer at the outer surfaces of the pad is higher compared to that at rotor outer surfaces because it is located in the bearing housing where oil ensures higher heat convection. The assumed convection coefficient values had been kept constant, for different rotor rotational speeds. Although rotor speed affects the convection coefficient at the rotor-air interface, its influence on the overall bearing performance is not substantial and can be neglected. In the fluid-pad and fluid-rotor interfaces, continuity of temperature and heat flux is implemented.

For the reasons discussed in Section 2.4, the pad surface is usually plated with a thin layer of Babbitt metal which has slightly different thermal properties (heat capacity) than the pad material. Here, for simplicity, a homogenous pad is assumed; its equivalent calculated using the following formula:

$$\lambda_s = \frac{\lambda_{pad} t_{pad} + \lambda_{babbitt} t_{babbitt}}{t_{back} + t_{babbitt}} \tag{45}$$

where,

$\lambda_{back}$: thermal conductivity of pad

$\lambda_{babbitt}$: thermal conductivity of Babbitt layer

$t_{babbitt}$: thickness of Babbitt layer

$t_{back}$: backup plate thickness

At the collar inner surface, an adiabatic condition is assumed, whereas rotational periodicity is set at the collar side surfaces.

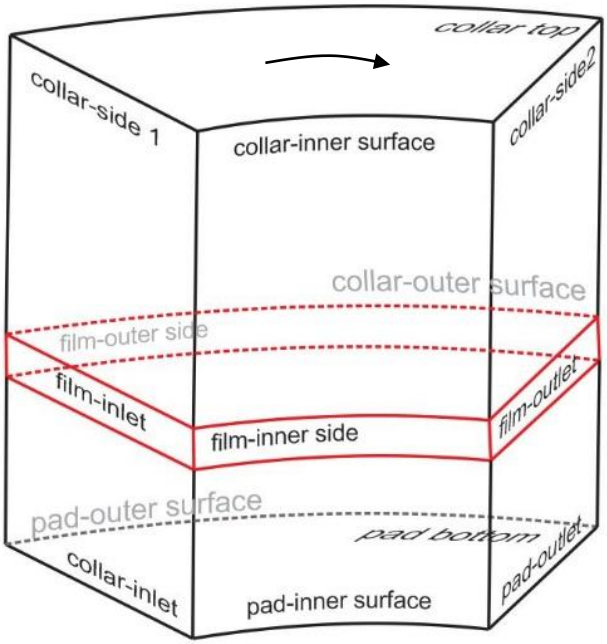


**Figure 14: Sector pad bearing: name convention of rotor, pad and film boundary surfaces**

| **Collar – Rotating about Global-Z axis** | |
|---|---|
| Collar- Top | $a_{conv} = 25\ W/m^2.K,\ T_{amb} = 20^oC$ |
| Collar- Bottom | Fluid-Solid interface: Heat Flux, Temperature Continuity |
| Collar- Outer surface | $a_{conv} = 25\ W/m^2.K,\ T_{amb} = 20^oC$ |
| Collar- Inner surface | Adiabatic |
| Collar-Sides | Periodic Conditions |
| **Pad – Stationary Domain** | |
| Pad - Top | Fluid-Solid interface: Heat Flux, Temperature Continuity |
| Pad - Bottom | $a_{conv} = 100\ W/m^2.K,\ T = T_{feed}$ |
| Pad - Outer surface | $a_{conv} = 100\ W/m^2.K,\ T = T_{feed}$ |
| Pad - Inner surface | $a_{conv} = 100\ W/m^2.K,\ T = T_{feed}$ |
| Pad - Inlet Side | Adiabatic |
| Pad - Outlet Side | Adiabatic |
| **Fluid Domain** | |
| Film - Inlet | Opening: zero relative pressure, $\frac{\partial \boldsymbol{V}}{\partial n^*} = \frac{\partial T}{\partial n^*} = 0$ |
| Film – Inner side | Opening: zero relative pressure, $\frac{\partial \boldsymbol{V}}{\partial n^*} = \frac{\partial T}{\partial n^*} = 0$ |
| Film – Outer side | Outlet: zero relative pressure, $\frac{\partial \boldsymbol{V}}{\partial n^*} = \frac{\partial T}{\partial n^*} = 0$ |
| Film – Outlet | Outlet: zero relative pressure, $\frac{\partial \boldsymbol{V}}{\partial n^*} = \frac{\partial T}{\partial n^*} = 0$ |
| *where n is the vector normal to the surface | |

**Table 3: Thermal and flow boundary conditions for the tilting pad of the present study.**

For the fluid domain, an opening type condition with zero relative pressure was set for the inlet boundary. This means that backflow is permitted and it is likely to occur because of the pressure field inside the channel (Poiseuille flow, Section 2.2). The assumption of zero pressure at the leading edge may be not strictly valid in the case of groove existence [2-3]. As oil is entrained into the channel, part of it is stagnated at the pad side resulting in a positive pressure at the leading edge. However, the phenomenon was ignored for simplicity since it has negligible impact on load carrying capacity, as an effect of hydrostatic action, according to [37]. The same, opening type, condition was used for the inner radius surface while the rest of sides (trailing edge, outer radius surface) are taken as outlets. Furthermore, at all edges, the pressure is normally set to zero. The film temperature at the leading edge of the pad is determined taking into account the hot oil carry over effect which is explained hereinafter.

***Hot Oil Carry Over Effect***

Heat balance in the groove region is not readily determined. Heat generated in the lubricant by viscous shearing is partly released to the surrounding structure, while the main part is taken away with the flow and, ideally, is to be discharged to a drain/cooling container. That amount of hot oil is replaced by feeding oil of low temperature. However, the bearing pads are arranged in such way that the outlet of the preceding pad is located close to the inlet of the following one and at the same time, the space occupied by the grooves is as small as possible in order to maximize the active bearing surface. Due to these reasons, a quantity of warm lubricant which exits from the preceding pad enters the inlet of the following, one so that the hot lubricant replacement is never perfect. In practice, this effect increases oil inlet temperature in comparison to the cold feeding oil temperature.

In contrast to using an empirical method such as the one suggested by Ettles in [38], in this study, the mixing phenomenon is approximated in a more deterministic manner, based on the methodology presented in [39]. Thus, to acquire an estimation of the input temperature, we consider the conservation of mass in the channel and the conservation of energy at the grooves. Based on Figure 15, these yield:

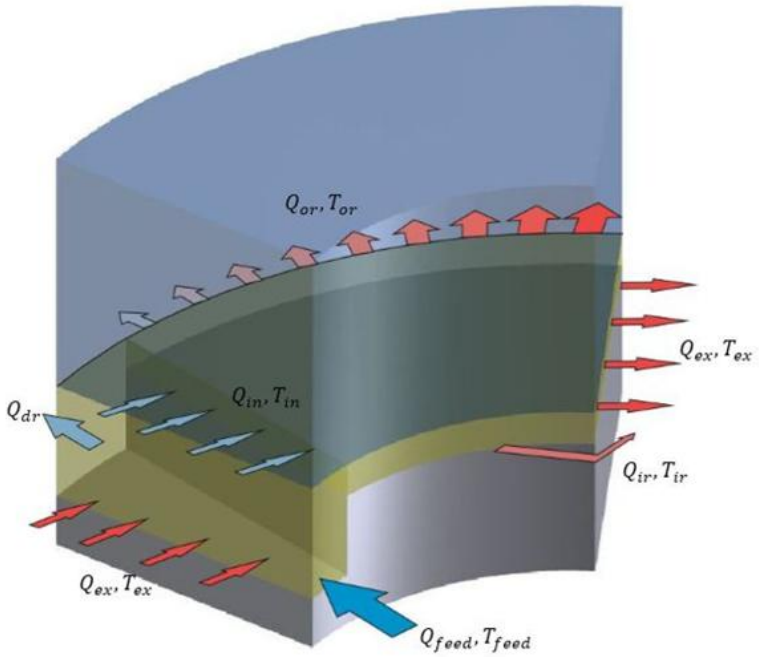


**Figure 15: Mass oil flows in the channel and within groove domain.**

- Conservation of mass in the channel:

$$Q_{in} = Q_{or} + Q_{ex} + Q_{ir} \tag{46}$$

- Conservation of feeding oil:

$$Q_{feed} = Q_{dr} + Q_{or} \tag{47}$$

- Conservation of energy within a groove:

$$Q_{feed}T_{feed} + Q_{ir}T_{ir} + Q_{ex}T_{ex} + H_{rotor} = (Q_{dr} + Q_{in})T_{in} + H_{groove} \tag{48}$$

where mass flow rate and temperature symbols are defined in Figure 15.

This approach assumes that, at the groove region, the collar conducts the same amount of heat as the bearing housing absorbs at the same time. In this way the modeling of complex energy paths which have minor impact on the performance of the bearing, is avoided.

$$H_{rotor} \cong H_{groove} \tag{49}$$

Solving Eq.(48) with respect to $T_{in}$, we get:

$$T_{in} = \frac{Q_{feed}T_{feed} + Q_{ex}T_{ex} + Q_{ir}T_{ir}}{Q_{dr} + Q_{in}} \quad (50)$$

Replacing the Eqs.(46),(47) to Eq.(50), yields:

$$T_{in} = \frac{Q_{feed}T_{feed} + Q_{ex}T_{ex} + Q_{ir}T_{ir}}{(Q_{feed} - Q_{or}) + (Q_{ir} + Q_{or} + Q_{ex})} = \frac{Q_{feed}T_{feed} + Q_{ex}T_{ex} + Q_{ir}T_{ir}}{Q_{feed} + Q_{ir} + Q_{ex}} \quad (51)$$

As can be seen from the above equation, the prerequisite for finding $T_{in}$ is the calculation of quantities $Q_{ex}, T_{ex}, Q_{ir}, T_{ir}, Q_{or},$ for given $Q_{feed}, T_{feed}$. However, these quantities depend on multiple factors (such as film geometry, specific load, shaft speed) and their calculation would not been possible without the use of CFD methods.

A representative indicator of the mixing phenomenon is the quantity α in the following equation, which is called hot oil carry over coefficient, and typically ranges around 0.7:

$$T_{in} = a \cdot T_{feed} + (1 - a) \cdot T_{ex} \quad (52)$$

Since both $T_{ex}$ and $T_{ir}$ temperatures are affected by $T_{in}$, the calculation of leading edge temperature is an iterative process. Initially, the assumption $T_{in} = T_{feed}$ is made. In order to minimize the independent variables of the problem, the feeding oil temperature was set at $50^{o}C$ and the feeding oil flow rate was set at $0.00025\ m^3/s$, while they were retained constants for all cases examined.

***Bearing Equilibrium***

The geometry of the lubricant film varies depending on operating conditions. Mathematically, it is described as a function of the two tilt angles about the pivot point; particular of pitch angle in the circumferential direction, and roll angle in the radial direction respectively, as well as of the film thickness at the pivot point. Considering a local coordinate system at the pivot point, the film thickness at any point is expressed as follows:

$$H(x_p, y_p) = H_{pivot} + tan(\theta_{pitch}) \cdot x_p + tan(\theta_{roll}) \cdot y_p \quad (53)$$

For any film geometry defined as above, the pressure distribution is integrated over the pad area to give the resulting force and the moments in two perpendicular directions about the pivot point. For the calculation, a Half-Sommerfeld type of boundary condition is implemented which ignores any negative pressures. With the input variable being the applied load on the bearing ($W_{req}$), the following equations are solved to obtain the film geometry which represents the physical balance of the bearing at a steady state. In the

moment equations only the resultant force due to film pressure is considered as the moment due to friction has a minor impact and can be ignored.

$$W - W_{req} = \int_0^L \int_0^B p_{HS} dxdy - W_{req} = 0 \tag{54}$$

$$M_{x,p} = \int_0^L \int_0^B p_{HS} x dxdy = 0 \tag{55}$$

$$M_{y,p} = \int_0^L \int_0^B p_{HS} y dxdy = 0 \tag{56}$$

where $p_{HS}$ is the pressure after application of the Half-Sommerfeld boundary condition, defined as:

$$p_{HS} = \begin{cases} p & \text{if} \quad p \geq 0 \\ 0 & \text{if} \quad p < 0 \end{cases}$$

## 3.3. The Newton-Raphson method

The above system of equations is solved using the Newton-Raphson method, which is implemented through a scripting tool coupled with ANSYS software. With this technique it is possible to adjust the film geometry in terms of $h_{pivot}, \theta_{pitch}, \theta_{roll}$, until the residuals Eqs. (54), (55) and (56) are below some threshold.

The Newton-Raphson method is the simplest multidimensional root-finding technique, while it is also extremely powerful, as it can be applied, theoretically, to any N-dimensional system. At the same time, it displays rapid convergence provided, however, that a sufficiently good initial guess is made. Starting with an initial guess which is reasonably close to the true root, the main idea of this method is that a function is approximated locally by its tangent line. The intercept of the tangent line with the x-axis will typically be a better approximation to the function's root than the original guess, and then, the method can be iterated.

Applying the method to a system of three functional relations to be zeroed, which involve respectively three independent variables, is as follows:

$$F_1(x_1, x_2, x_3) = 0 \tag{57}$$

$$F_2(x_1, x_2, x_3) = 0 \tag{58}$$

$$F_3(x_1, x_2, x_3) = 0 \tag{59}$$

We now let $\boldsymbol{x}$ denote the entire vector of values $x_i$ and $\boldsymbol{F}$ denote the entire vector of functions $F_i$**.** Newton's method also requires calculation of the functions derivatives. If analytical expressions for the derivatives are not available, it is necessary to approximate the true local derivatives as follows:

$$\boldsymbol{F}'(\boldsymbol{x}) \approx \frac{\boldsymbol{F}(\boldsymbol{x} + d\boldsymbol{x}) - \boldsymbol{F}(\boldsymbol{x})}{\boldsymbol{dx}} \tag{60}$$

In the neighborhood of $\boldsymbol{x}$, each of the functions $F_i$ can be expanded in Taylor series:

$$F_i(\boldsymbol{x} + \delta\boldsymbol{x}) = F_i(\boldsymbol{x}) + \sum_{j=1}^{3} \frac{\partial F_i}{\partial x_j} \delta x_j + O(\delta \boldsymbol{x}^2) \qquad i = (1,2,3) \quad j = (1,2,3) \tag{61}$$

The matrix of partial derivatives appearing in Eq.(61) is the Jacobian matrix $J$:

$$J = \begin{bmatrix} \dfrac{\partial F_1}{\partial x_1} & \dfrac{\partial F_1}{\partial x_2} & \dfrac{\partial F_1}{\partial x_3} \\ \dfrac{\partial F_2}{\partial x_1} & \dfrac{\partial F_2}{\partial x_2} & \dfrac{\partial F_2}{\partial x_3} \\ \dfrac{\partial F_3}{\partial x_1} & \dfrac{\partial F_3}{\partial x_2} & \dfrac{\partial F_3}{\partial x_3} \end{bmatrix} \tag{62}$$

The determinant of matrix $J$ is calculated as follows:

$$\begin{aligned} detJ = \frac{\partial F_1}{\partial x_1}\left(\frac{\partial F_2}{\partial x_2} \cdot \frac{\partial F_3}{\partial x_3} - \frac{\partial F_3}{\partial x_2} \cdot \frac{\partial F_2}{\partial x_3}\right) - \frac{\partial F_1}{\partial x_2}\left(\frac{\partial F_2}{\partial x_1} \cdot \frac{\partial F_3}{\partial x_3} - \frac{\partial F_3}{\partial x_1} \cdot \frac{\partial F_2}{\partial x_3}\right) \\ + \frac{\partial F_1}{\partial x_3}\left(\frac{\partial F_2}{\partial x_1} \cdot \frac{\partial F_3}{\partial x_2} - \frac{\partial F_3}{\partial x_1} \cdot \frac{\partial F_2}{\partial x_2}\right) \end{aligned} \tag{63}$$

By neglecting terms of order $\delta \boldsymbol{x}^2$and higher and by setting $F_i(\boldsymbol{x} + \delta\boldsymbol{x}) = 0$, we obtain a set of linear equations for the corrections $\delta\boldsymbol{x}$ that move each function closer to zero simultaneously, namely

$$\boldsymbol{J} \cdot \delta\boldsymbol{x} = -\boldsymbol{F} \tag{64}$$

The corrections are then added to the solution vector:

$$\boldsymbol{x}_{new} = \boldsymbol{x}_{old} + \delta\boldsymbol{x} \tag{65}$$

Which, in expanded form, reads:

$$x_{1,new} = x_{1,old} - \left( \left( \frac{\partial F_2}{\partial x_2} \cdot \frac{\partial F_3}{\partial x_3} - \frac{\partial F_2}{\partial x_3} \cdot \frac{\partial F_3}{\partial x_2} \right) \cdot F_1(x_{1,old}) + \left( \frac{\partial F_1}{\partial x_3} \cdot \frac{\partial F_3}{\partial x_2} - \frac{\partial F_3}{\partial x_3} \cdot \frac{\partial F_1}{\partial x_2} \right) \cdot F_2(x_{1,old}) + \left( \frac{\partial F_2}{\partial x_2} \cdot \frac{\partial F_2}{\partial x_3} - \frac{\partial F_1}{\partial x_3} \cdot \frac{\partial F_2}{\partial x_2} \right) \cdot F_3(x_{1,old}) \right) / detJ \quad (66)$$

$$x_{2,new} = x_{2,old} - \left( \left( \frac{\partial F_2}{\partial x_3} \cdot \frac{\partial F_3}{\partial x_1} - \frac{\partial F_3}{\partial x_3} \cdot \frac{\partial F_2}{\partial x_1} \right) \cdot F_1(x_{2,old}) + \left( \frac{\partial F_1}{\partial x_1} \cdot \frac{\partial F_3}{\partial x_3} - \frac{\partial F_1}{\partial x_3} \cdot \frac{\partial F_2}{\partial x_1} \right) \cdot F_2(x_{2,old}) + \left( \frac{\partial F_1}{\partial x_3} \cdot \frac{\partial F_2}{\partial x_1} - \frac{\partial F_2}{\partial x_3} \cdot \frac{\partial F_1}{\partial x_1} \right) \cdot F_3(x_{2,old}) \right) / detJ \quad (67)$$

$$x_{3,new} = x_{3,old} - \left( \left( \frac{\partial F_2}{\partial x_1} \cdot \frac{\partial F_3}{\partial x_2} - \frac{\partial F_2}{\partial x_2} \cdot \frac{\partial F_3}{\partial x_1} \right) \cdot F_1(x_{3,old}) + \left( \frac{\partial F_1}{\partial x_2} \cdot \frac{\partial F_3}{\partial x_1} - \frac{\partial F_3}{\partial x_2} \cdot \frac{\partial F_1}{\partial x_1} \right) \cdot F_2(x_{3,old}) + \left( \frac{\partial F_1}{\partial x_1} \cdot \frac{\partial F_2}{\partial x_2} - \frac{\partial F_1}{\partial x_2} \cdot \frac{\partial F_2}{\partial x_1} \right) \cdot F_3(x_{3,old}) \right) / detJ \quad (68)$$

In general, the convergence is quadratic: as the method converges, the difference between the solution and the approximation is squared (the number of accurate digits roughly doubles) at each step. In Table 4, a typical example of the successive estimations of the equilibrium finding process using the Newton-Raphson method is presented, and it verifies the above statement. Normally, the process is terminated after three or four iterations, achieving a convergence of under $0.1\,Nm$ of moment and under $15\,N$ of applied load.

However, as we have already mentioned, the initial guess is of great importance. In Table 5, where, for the same case as above, the initial guess is different and at a greater distance from the known solution, the method fails to converge. This is due to fact that film thickness at the pivot location, $H_{pivot}$, is assigned a negative value in the 3rd iteration which has no physical meaning. In addition, the pitch angle, $\theta_{pitch}$, which regulates the wedge's

convergence in the circumferential direction also takes a negative value leading to a divergent film geometry.

| Iter. | Independent parameters | | | | | | Dependent parameters | | |
|---|---|---|---|---|---|---|---|---|---|
| | $H_{pivot}$ (μm) | | $\theta_{pitch}$ (*μdeg*) | | $\theta_{roll}$ (*μdeg*) | | *W-W$_{req}$ (N)* | $M_{x,p}$ *(Nm)* | $M_{y,p}$ *(Nm)* |
| *Guess* | 30 | 27.04% | 20870.2 | 67.09% | 8285.8 | 80.12% | 914.532 | 2.60963 | 8.62404 |
| *1st* | 23.2815 | -1.41% | 11388.5 | -8.82% | 4033.6 | -12.32% | 539.607 | -0.79714 | -2.60607 |
| *2nd* | 23.7207 | 0.45% | 12407.3 | -0.66% | 4491.9 | -2.36% | 184.696 | -0.23008 | -0.57628 |
| *3rd* | 23.6379 | 0.10% | 12505.9 | 0.13% | 4586.0 | -0.31% | 12.327 | -0.04137 | -0.02913 |
| *4th* | 23.6153 | 0.00% | 12488.9 | -0.01% | 4599.5 | -0.02% | 1.071 | -0.00154 | -0.00438 |
| *5th* | 23.6150 | 0.00% | 12489.7 | 0.00% | 4600.2 | 0.00% | 0.114 | -0.00010 | -0.00086 |
| *6th* | 23.6151 | 0.00% | 12490.1 | 0.00% | 4600.3 | 0.00% | 0.031 | -0.00005 | -0.00012 |

**Table 4 Implementation of the Newton-Raphson method in tilting pad thrust bearing.**

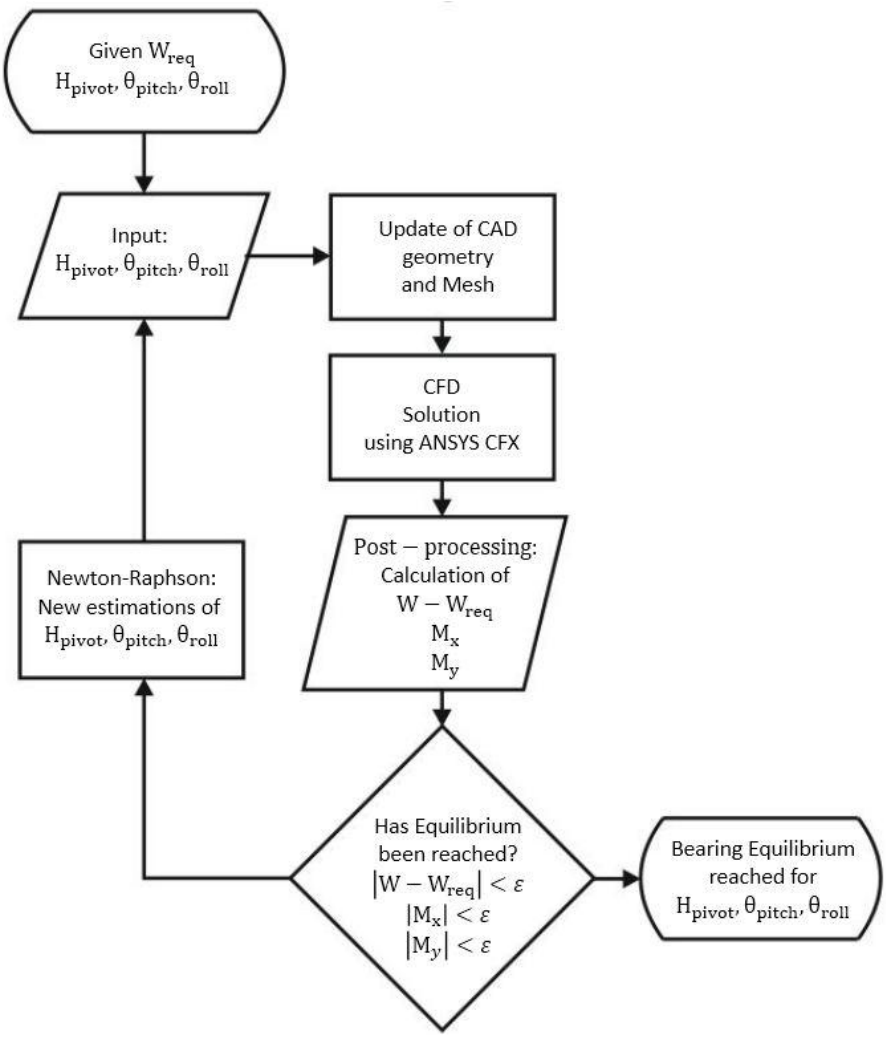


**Figure 16: Iterative process of approaching the equilibrium position of a tilting pad thrust bearing.**

| Iter. | Independent parameters | | | | | | Dependent parameters | | |
|---|---|---|---|---|---|---|---|---|---|
| | $H_{pivot}$ (μm) | | $\theta_{pitch}$ ($\mu deg$) | | $\theta_{roll}$ ($\mu deg$) | | $W$-$W_{req}$ (N) | $M_{x,p}$ (Nm) | $M_{y,p}$ (Nm) |
| *Guess* | 32 | 35.506% | 22196.52 | 77.713% | 11663.95 | 153.548% | 914.52 | 2.609 | 8.624 |
| *1st* | 20.1332 | -14.75% | 7202.58 | -42.333% | 672.46 | -85.382% | 539.60 | -0.797 | -2.606 |
| *2nd* | 52.1897 | 121.0% | 4328.77 | -65.342% | -36.27 | -100.788% | 184.69 | -0.230 | -0.576 |
| *3rd* | -11.1475 | -147.5% | -3063.70 | -124.529% | 3274.25 | -28.825% | Fail to adjust geometry | | |

**Table 5: Unsuccessful implementation of Newton-Raphson method due to poor selection of an initial guess.**

## 3.4. Spatial discretization - Mesh Study

The system of equations presented in Section 2.3 is solved on a finite volume grid. Its basic purpose is the discretization of a continuous physical domain, such as the lubricant domain of a bearing system, into a finite number of elements for which the solution of complex equations is attainable. However, grid (mesh) quality in terms of density (number of elements) as well as shape is of high importance. Finer grids lead to more realistic solutions and faster convergence, as they may increase solver's (software) performance.

In this study, a hexahedral mesh was used for all domains (pad, rotor, film) which follows the pad curvature along its length. The density is increased close to the rigid surfaces in order to approximate the thermal boundary layers with sufficient accuracy. A typical mesh of a thrust-bearing is presented in Figure 17.

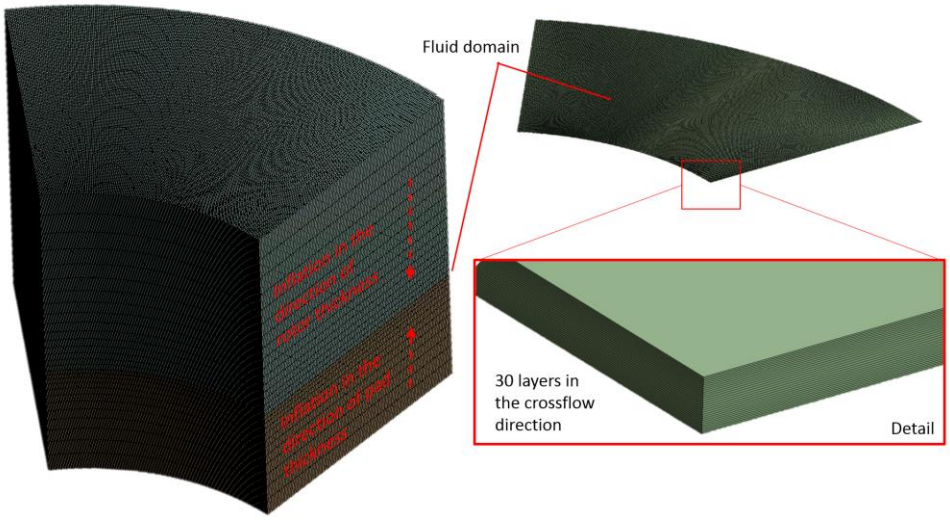


**Figure 17: Typical mesh of the tilting-pad thrust bearing of the present study.**

For determining the accuracy provided by certain grid densities, a mesh study was performed. The number of element layers along the film thickness and the number of cells (divisions) per linear meter were elected as the most representative mesh parameters. Spatial resolution tests were performed by generating meshes with numbers of finite volumes both lower and substantially higher than the typical meshes finally used. The design case of 1500 RPM rotational speed and 2.0 MPa specific load was solved multiple times with the above-mentioned parameters varying. The film geometry with a thickness ranging around 30 micrometers was kept fixed for all runs. It proved that the most sensitive physical property to grid changes was the total load $W$ that develops on pad surface.

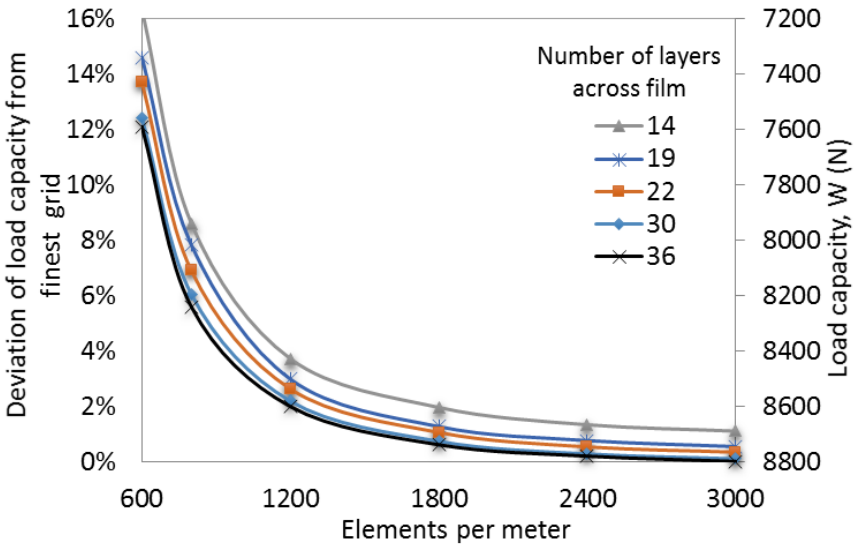


**Figure 18: Mesh study analysis.**

The results are presented in Figure 18. The relative differences in all the flow integral quantities (load carrying capacity, friction force) between typical and very fine meshes were in all cases lower than 0.5%. As can be seen, the dominant parameter for grid quality is the number of elements in the circumferential direction. However, for values higher than 2000 elements/meter, the effect of this parameter becomes negligible. As a result, though it is of secondary importance, the number of elements across the film thickness determines the final precision of the model. Given the above results, it was considered appropriate to use a grid with 2400 elements per meter and 30 elements across film thickness. Even though it was too dense for the standard geometry it would be also able to provide sufficient accuracy for the more geometrically complex models, presented in Chapter 4. Typical meshes consisted of approximately $1.4x10^6$ finite volumes.

## 3.5. Model Validation

The validation of the model used in the present study was performed by comparing the results of respective cases with those in published literature. The THD problem of tilting thrust bearings has been solved for plain pads by Glavatskih & Fillon [9] using Reynolds' theory. Since the surface of a plain tilting pad bearing is smooth and Reynolds numbers are small, the results of the present CFD model should be equivalent to those obtained by solution of the Reynolds' equation.

Data for three different loading cases have been compared[1]. This is enough to provide acceptable certainty for the validation. Through the results, it becomes apparent that the present simulation is sufficiently accurate since it provides results for important parameters with deviation below 2%, in comparison to results by from Glavatskih & Fillon.

| **Parameters** | **CFD - Present Study** | | | **Reynolds Equation Glavatskih et al, 2007** | | |
|---|---|---|---|---|---|---|
| Shaft speed, *N (RPM)* | 1500 | 1500 | 1500 | 1500 | 1500 | 1500 |
| Specific load, *P (MPa)* | 1.0 | 1.5 | 2.0 | 1.0 | 1.5 | 2.0 |
| Film thick. at pivot, $H_{pivot}$*(μm)* | 48.68 | 34.02 | 23.58 | 46.11 | 33.04 | 24.67 |
| Pitch angle, $\theta_{pitch}$ *(μdeg)* | 30930 | 20882 | 12436 | 27400 | 19304 | 13668 |
| Roll angle, $\theta_{roll}$ *(μdeg)* | 9995 | 6753 | 4586 | 9134 | 6421 | 4763 |
| Min. film thickness, $H_{min}$ *(μm)* | 31.35 | 22.32 | 16.77 | 30.87 | 22.30 | 17.14 |
| Max. oil pressure, $p_{max}$ *(MPa)* | 2.40 | 3.62 | 4.88 | 2.41 | 3.64 | 4.85 |
| Hot oil carry over coeff., $a$ | 0.75 | 0.75 | 0.75 | 0.75 | 0.75 | 0.75 |
| Max. oil temperature, $T_{max}$ *(°C)* | 73.57 | 81.43 | 88.42 | 74.66 | 81.61 | 88.06 |
| Avg. Film/Rotor Temp., $T_{f/r}$ *(°C)* | 63.04 | 69.67 | 77.22 | 63.05 | 69.68 | 77.22 |
| Avg. Film Inlet Temp., $T_{in}$ *(°C)* | 54.64 | 56.71 | 59.02 | 58.51 | 61.97 | 65.80 |
| Max. Film/Pad Temp., $T_{f/p}$ *(°C)* | 73.15 | 81.16 | 88.27 | 74.25 | 81.31 | 87.85 |
| Max. Pad Temp., $T_{pad}$ *(°C)* | 73.04 | 81.07 | 88.22 | 73.89 | 80.95 | 87.54 |

**Table 6: List of operating parameters to compare between CFD solution (present study) and Reynolds' equation solution (Glavatskih et al, 2007).**

To approximate the validation data presented in Table 6, the studied model had to be slightly modified in order to be consistent with that studied in [25]. In particular, the following changes were made:

- The rotor was ignored in the model and a constant temperature of 62°C at the film-rotor interface was imposed.
- A hot oil carry over coefficient $\alpha = 0.75$ was imposed.

[1] Data were provided by Prof. M. Fillon from the University of Poitiers. The authors gratefully acknowledge helpful discussions with Prof.Fillon.

- The ambient temperature was taken as $T_{amb} = 54.5\,^{o}C$ instead of 20 $^{o}C$.

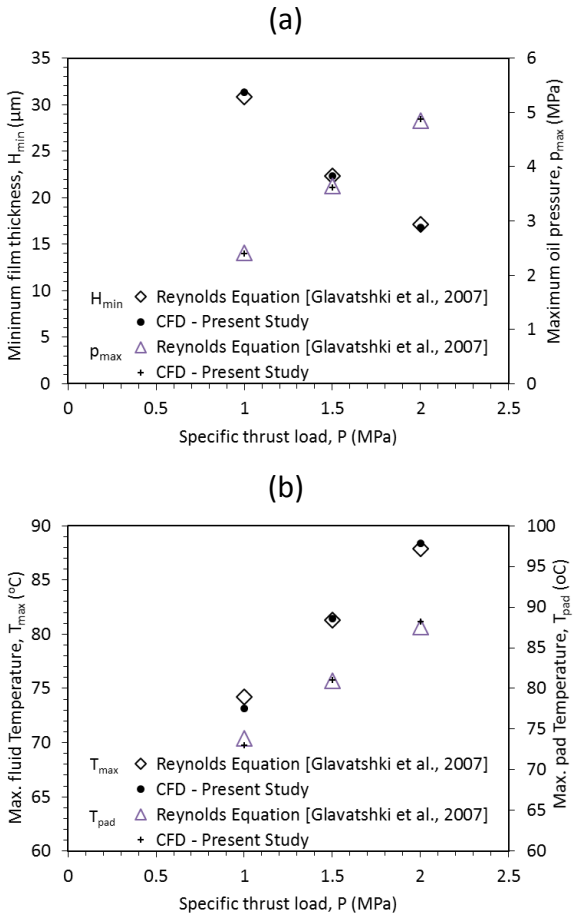


**Figure 19: Present CFD model: Validation against published literature results (a) minimum film thickness and maximum oil pressure versus specific thrust load, and (b) maximum fluid temperature and maximum pad temperature versus specific thrust load.**

## 3.6. Results of the basic model

The main advantage of tilting thrust bearings is their ability to support external axial loads over a wide operating range. Therefore, in the present study, a comparison has been performed considering four representative values of specific load, from 0.5 to 2.0 MPa, and two values of rotational speed, 1500 RPM and 3000 RPM. In Table 7, various operating characteristics are presented in detail for the eight different cases under consideration. Here, the model presented in detail in Section 3.2 is used. The corresponding to rotational speed of 1500 RPM and specific load of 2.0 MPa, which yields a total pad load of $W = 8565N\ (873kg)$, will be used later as the reference condition.

| Shaft speed, N | 1500 RPM | | | | 3000 RPM | | | |
|---|---|---|---|---|---|---|---|---|
| *P (MPa)* | 0.50 | 1.00 | 1.50 | 2.00 | 0.50 | 1.00 | 1.50 | 2.00 |
| $H_{pivot}$ *(μm)* | 61.71 | 43.30 | 34.85 | 29.71 | 74.94 | 52.05 | 41.94 | 35.99 |
| $\theta_{pitch}$ *(mdeg)* | 34.313 | 26.442 | 22.690 | 20.361 | 40.728 | 30.832 | 26.360 | 23.752 |
| $\theta_{roll}$ *(mdeg)* | 12.586 | 8.612 | 6.748 | 5.675 | 14.990 | 10.147 | 8.035 | 6.799 |
| $H_{min}$ $(\mu m)$ | 42.97 | 28.52 | 21.92 | 17.97 | 52.67 | 34.85 | 27.00 | 22.36 |
| $p_{max}$ *(MPa)* | 1.19 | 2.37 | 3.55 | 4.73 | 1.18 | 2.37 | 3.55 | 4.72 |
| $T_{max}$ *(°C)* | 63.4 | 69.4 | 74.3 | 78.7 | 74.4 | 82.6 | 88.4 | 93.1 |
| $T_f$ *(Nm)* | 1.68 | 2.13 | 2.41 | 2.60 | 2.18 | 2.72 | 3.06 | 3.31 |
| $f$ | 0.0091 | 0.0058 | 0.0044 | 0.0035 | 0.0118 | 0.0074 | 0.0056 | 0.0045 |
| $P_f$ *(W)* | 263.52 | 334.82 | 378.67 | 409.15 | 683.52 | 855.77 | 962.87 | 1038.58 |
| $H_{rotor}$ $(W)$ | 7.96 | 8.65 | 9.29 | 9.88 | 9.27 | 10.06 | 10.71 | 11.29 |
| $H_{stator}$ $(W)$ | 6.23 | 8.77 | 10.89 | 12.81 | 12.68 | 16.40 | 19.00 | 21.07 |
| $H_{absorbed}$ | 5.38% | 5.20% | 5.33% | 5.55% | 3.21% | 3.09% | 3.09% | 3.12% |

**Table 7: Reference tilting-pad bearing design: Performance indices for different operating conditions of the bearing.**

In bearings, minimum film thickness is known to be directly related to bearing load: an increase in bearing load results in decreased bearing film thicknesses, and vice versa. This relationship is confirmed by the results of Table 7, which are shown in Figure 20(a). In the same figure, the effect of rotor speed on bearing performance is also apparent: higher rotational speeds lead to the formation of thicker lubricating oil films for the same imposed load. The latter is another effect predicted by the theory of hydrodynamic lubrication, as shown in Eq.(39).

Furthermore, shear stress is known to be directly related to velocity as well as to pressure gradient in the streamwise direction, see Eq.(31). Consequently, friction forces and therefore friction torque and friction losses are proportional to load and shaft speed. At the same time, considering the energy equation, the resulting temperature values are, as expected, dependent on the bearing operating conditions: Figure 20(b) and Figure 21(a) confirm the above correlations. From Figure 17(b) it also apparent that over 94.5% of the internal heat generation due to friction is removed by the oil itself, as only small percentage of heat is transferred to the environment through the rotor and stator. This result is consistent with that showed by Dadouche et al. in [6].

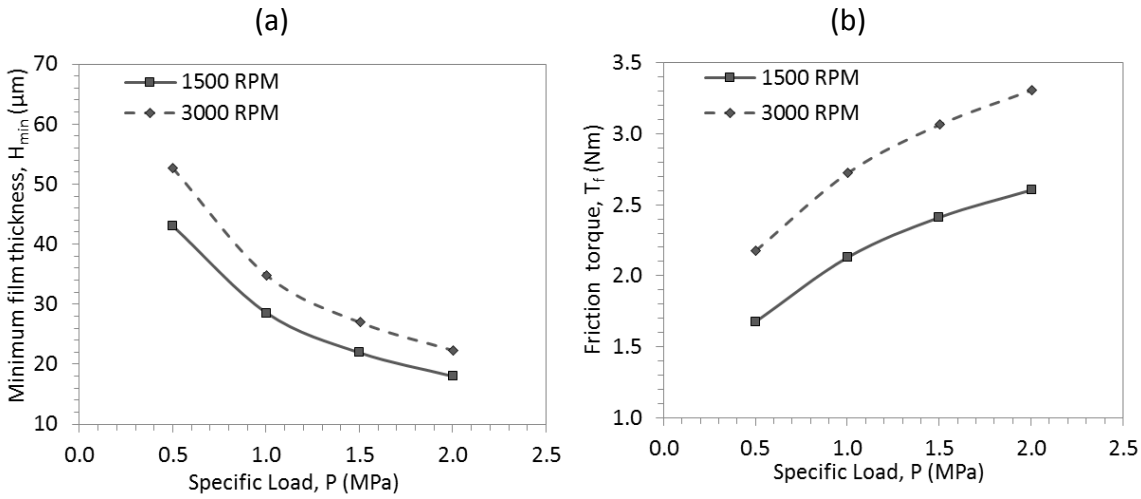


**Figure 20: (a) Minimum film thickness, $H_{min}$, and (b) Friction torque, $T_f$, versus specific bearing load for two different values of rotational speed.**

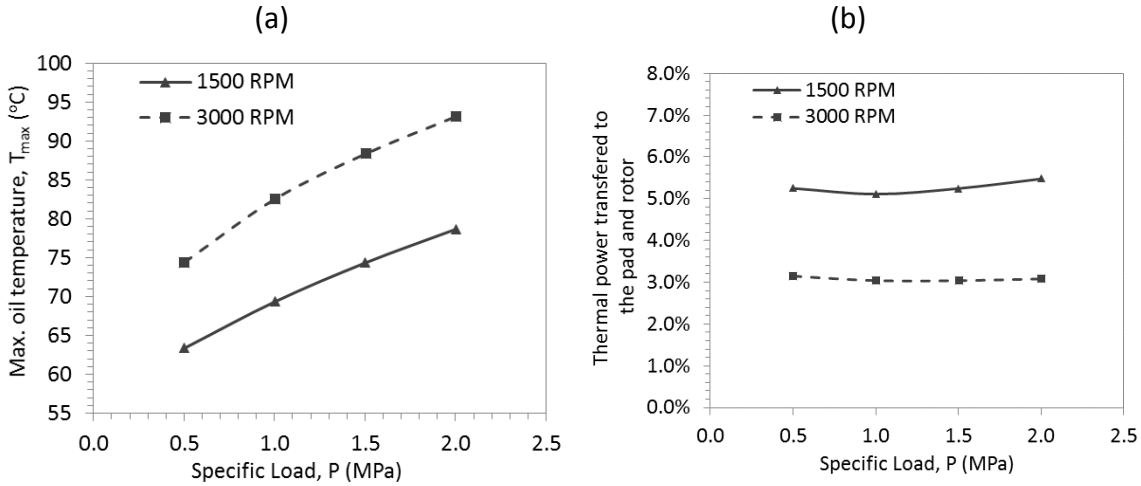


**Figure 21: (a) Maximum oil temperature, $T_{max}$, and (b) Thermal power transferred to the pad and rotor (as percentage of friction power) versus specific bearing load, for two different values of rotational speed.**

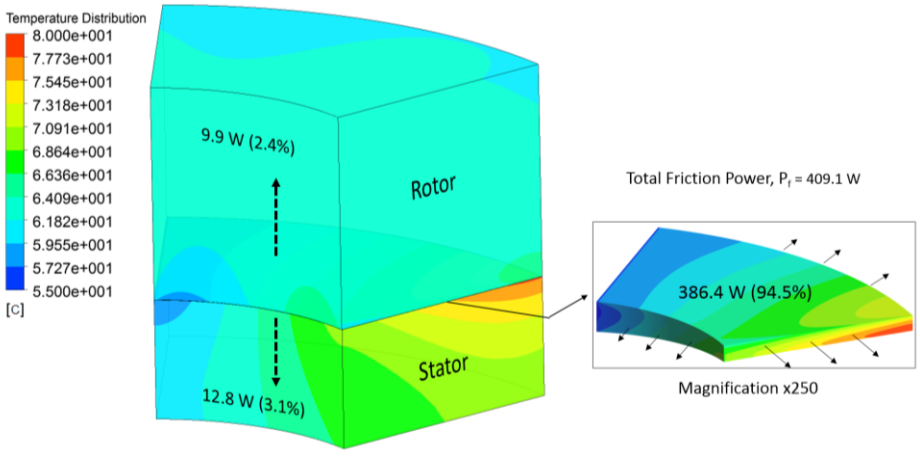


**Figure 22: Specific bearing load 2.0 MPa, rotational speed 1500 RPM: Total friction power and heat power transferred through the solid parts of the bearing.**

From the results of Table 7 and from Figure 23, it is noticeable that the coefficient of friction, $f$, is related to pitch angle ($\theta_{pitch}$). In particular, friction coefficient is a decreasing function of specific load, whereas the trend of pitch angle is similar. Therefore, the pitch angle at equilibrium could be also considered as an indicator of bearing efficiency (small values of pitch and correspond to small values of friction coefficient) and vice versa.

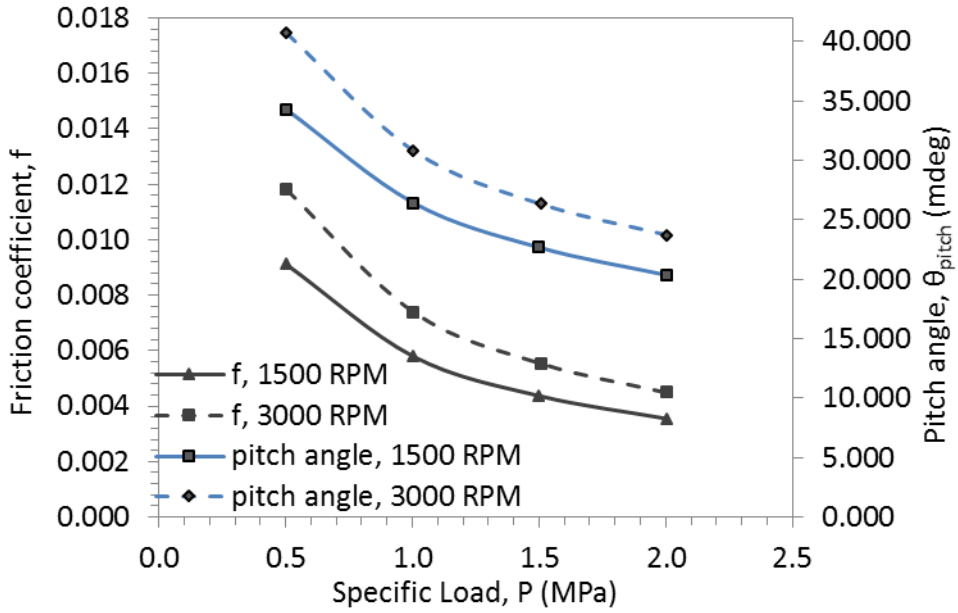


**Figure 23: Friction coefficient and pitch angle versus specific bearing load for two different values of rotational speed.**

The Reynolds number is defined based on the minimum film thickness, $H_{min}$ and the circumferential velocity of the rotor, $U = \omega r$. Taking into account the variations of circumferential velocity and viscosity variation (due to the temperature field), a local Reynolds number can be defined at every bearing location.

In Figure 24, a color-coded plot of the local Reynolds number is presented. The maximum value of 225 is found at the outermost region of the pad. Therefore, the considered assumption of laminar flow is confirmed. Although, there is not a single accepted Reynolds number corresponding to the onset of turbulence in bearing lubrication, prior studies (e.g. [34]) indicate the range from 1000 to 1500, where turbulence is likely to occur.

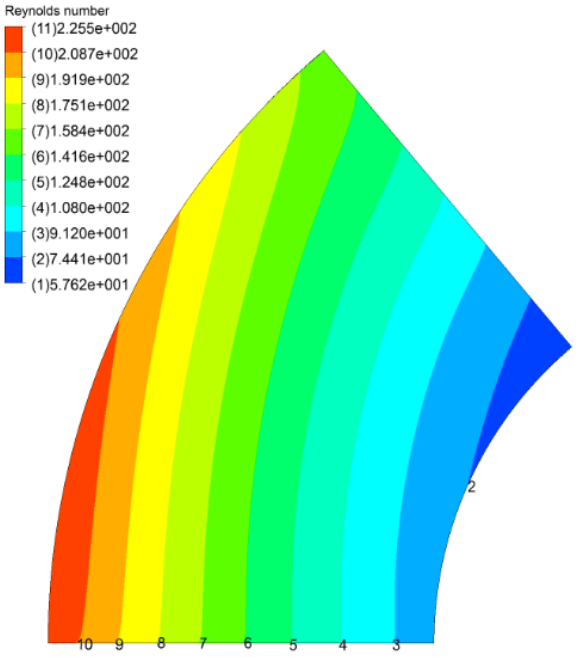


**Figure 24: Specific bearing load 2.0 MPa, rotational speed 3000 RPM: Color-coded plot of local Reynolds number.**

Figure 25 presents the corresponding distribution of pressure at three radial positions of the moving wall (rotor), see also Figure 26. As shown, pressure attains a maximum approximately at the bearing mid-sector ($r_{mid}$), decreasing towards the side edges of the bearing ($r_{inner}, r_{outer}$), due to fluid leakage.

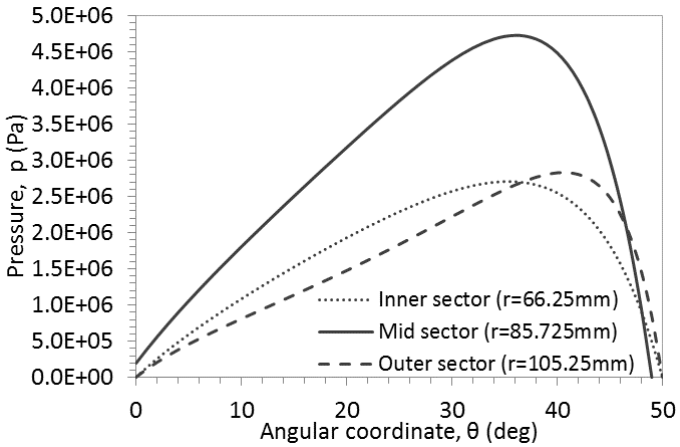


**Figure 25: Specific bearing load 2.0 MPa, rotational speed 1500 RPM: streamwise pressure distribution at three different radial positions of the bearing.**

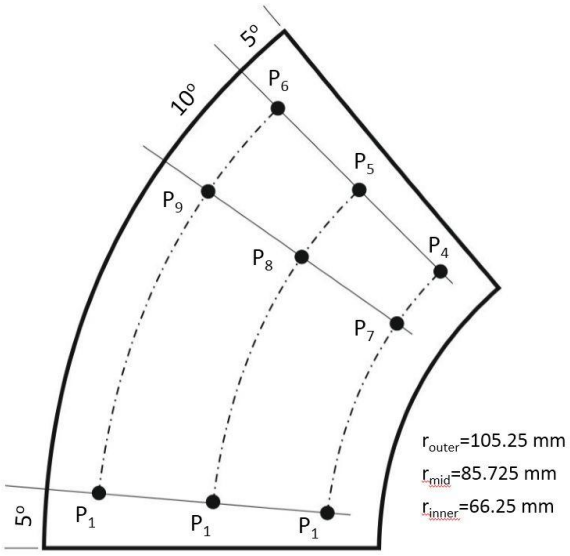


**Figure 26: Sketch of a bearing pad; depiction of points data output.**

(a) (b)

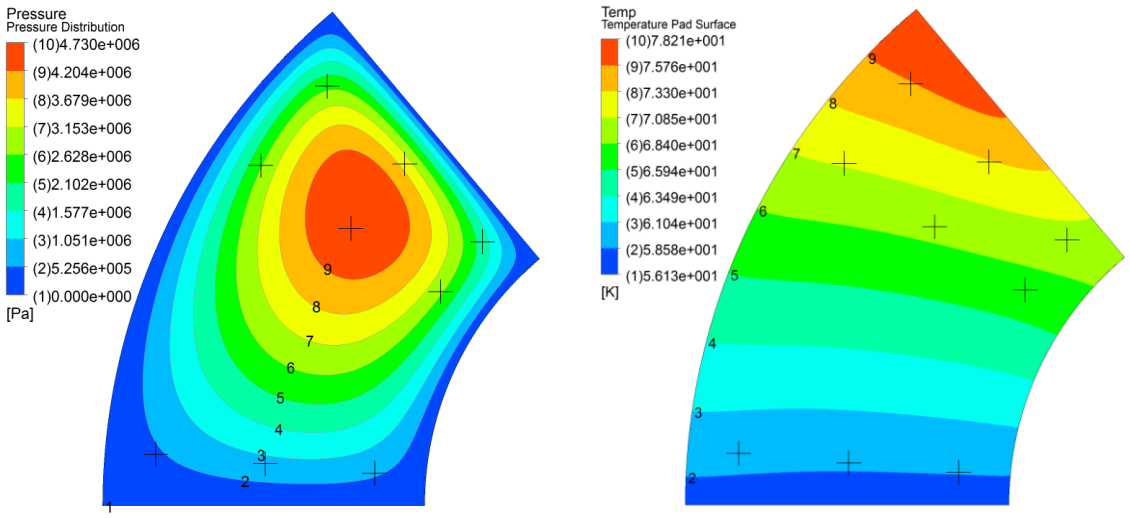


**Figure 27: Specific bearing load 2.0 MPa, rotational speed 1500 RPM: (a) Pressure and (b) Temperature distributions at the lubricant-pad interface.**

In Figure 27 pressure and temperature distributions at the fluid-pad interface for a specific bearing load of 2.0 MPa and rotational speed of 1500 RPM are presented. Pressure attains a maximum at a circumferential position, lying at approximately 70% of the bearing mid sector counting from inflow, which is slightly after the pivot point. The corresponding temperature distribution displays maximum values at the outer region of the bearing, close to the lubricant outflow. This can be attributed to the effect of oil heating due to viscous dissipation as well as the action of centrifugal forces.

| Shaft speed | 1500 RPM | | | | 3000 RPM | | | |
|---|---|---|---|---|---|---|---|---|
| P (MPa) | 0.50 | 1.00 | 1.50 | 2.00 | 0.50 | 1.00 | 1.50 | 2.00 |
| | **Local Pressure values on pad surface (Pa)** | | | | | | | |
| P1 | 1.44E+05 | 2.90E+05 | 4.40E+05 | 5.92E+05 | 1.44E+05 | 2.88E+05 | 4.35E+05 | 5.84E+05 |
| P2 | 2.20E+05 | 4.42E+05 | 6.69E+05 | 8.99E+05 | 2.21E+05 | 4.39E+05 | 6.60E+05 | 8.83E+05 |
| P3 | 1.12E+05 | 2.24E+05 | 3.39E+05 | 4.55E+05 | 1.12E+05 | 2.19E+05 | 3.26E+05 | 4.33E+05 |
| P4 | 4.50E+05 | 9.07E+05 | 1.36E+06 | 1.83E+06 | 4.48E+05 | 9.03E+05 | 1.36E+06 | 1.81E+06 |
| P5 | 8.38E+05 | 1.70E+06 | 2.57E+06 | 3.46E+06 | 8.28E+05 | 1.67E+06 | 2.52E+06 | 3.38E+06 |
| P6 | 5.98E+05 | 1.22E+06 | 1.84E+06 | 2.48E+06 | 5.93E+05 | 1.21E+06 | 1.83E+06 | 2.46E+06 |
| P7 | 6.86E+05 | 1.37E+06 | 2.04E+06 | 2.71E+06 | 6.87E+05 | 1.37E+06 | 2.06E+06 | 2.73E+06 |
| P8 | 1.18E+06 | 2.35E+06 | 3.52E+06 | 4.68E+06 | 1.18E+06 | 2.36E+06 | 3.53E+06 | 4.68E+06 |
| P9 | 6.52E+06 | 1.30E+06 | 1.95E+06 | 2.59E+06 | 6.53E+05 | 1.31E+06 | 1.96E+06 | 2.61E+06 |
| | **Local Temperature values on pad surface (°C)** | | | | | | | |
| P1 | 54.9 | 56.5 | 57.7 | 58.8 | 61.6 | 64.1 | 65.7 | 66.9 |
| P2 | 55.1 | 56.8 | 58.0 | 59.1 | 62.0 | 64.6 | 66.3 | 67.6 |
| P3 | 55.3 | 57.1 | 58.3 | 59.4 | 62.4 | 65.4 | 67.4 | 68.9 |
| P4 | 59.1 | 63.2 | 66.7 | 70.1 | 67.8 | 74.3 | 77.6 | 80.7 |
| P5 | 60.8 | 65.6 | 69.5 | 73.3 | 70.4 | 76.9 | 81.6 | 85.7 |
| P6 | 61.9 | 67.2 | 71.5 | 75.6 | 72.3 | 78.5 | 84.7 | 89.0 |
| P7 | 55.5 | 60.0 | 62.2 | 67.2 | 61.3 | 65.0 | 69.8 | 73.2 |
| P8 | 55.9 | 59.6 | 63.3 | 69.4 | 61.8 | 65.9 | 69.4 | 72.6 |
| P9 | 56.1 | 60.1 | 63.9 | 71.1 | 61.9 | 66.2 | 69.8 | 73.1 |

**Table 8: Record of pressure and temperature at the locations depicted in Figure 26, for different values of bearing specific load and rotational speed.**

# 4. Artificial surface texturing / Hydrophobicity

The pressure buildup mechanism of hydrodynamically lubricated bearings is highly sensitive to changes in the bearing surface geometry. Recent research activity has demonstrated that appropriate introduction of small periodic irregularities, in the form of dimples or grooves, on the pad surface of thrust bearings has beneficial effects on the bearing performance. This artificial surface texturing serves to increase the hydrodynamically generated pressure, trap debris that can damage the working surfaces, and act as a lubricant reservoir, providing oil, especially in mixed lubrication conditions, where local oil starvation prevails. In the recent literature, several different dimple geometries, including rectangular, trapezoidal, cylindrical or spherical geometries, have been studied. Among the different possible designs, bearings with rectangular texturing are of special interest, mainly because, in comparison to spherical patterns, rectangular texturing provides higher load capacity due to the corresponding constant texture depth [21]. At the same time, rectangular grooves have lower manufacturing cost compared with the more complex trapezoidal patterns.

The objective of the present Chapter is the cross-evaluation of tilting pad thrust bearings with different texture patterns, in comparison to the reference plain (conventional) bearing presented in Chapter 3, under similar operating conditions. The ultimate goal is to find appropriate texture patterns that provide enhanced performance characteristics. Regarding texture patterns, four different types of sector-pad thrust bearings of the same principal dimensions have been evaluated: (a) a pocket bearing, (b) a bearing with circumferential grooves, (c) a bearing with radial grooves and (d) a bearing with rectangular dimples, sketches of the geometry of each are presented in Figure 28. In addition, for the two most effective geometries, the impact of varying texture parameters is investigated at representative operating conditions. The examined parameters are textured depth, as well as radial and circumferential texture extents.

Finally, as an alternative to the textured bearing, a pivoted thrust bearing with hydrophobic properties on part of the pad surface is also examined in the final section of this chapter.

## 4.1. Textured models

The numerical model defined in Chapter 3 is used as a basis for generating models of textured tilting pad bearings. The boundary conditions, spatial discretization and operating parameters are kept the same, whereas, the geometric model is altered, in particular, at the surface of the pad. As already mentioned, four different types of surface patterns are implemented, all covering a comparable region of the pad area.

In particular, the circumferential span of all textured patterns extends from the leading edge up to an angle of 35°, which corresponds to a texture length $L_t = 0.7L$, where $L$ is the circumferential pad length at mid sector. Texture in the radial direction is symmetric with respect to the pad mid-sector; the textured radial width being $B_t = 0.8B$, where $B$ is the pad radial width. Textured depth, $H_t$, is set equal to 30 μm for all simulations. The thrust collar surface is assumed planar and smooth.

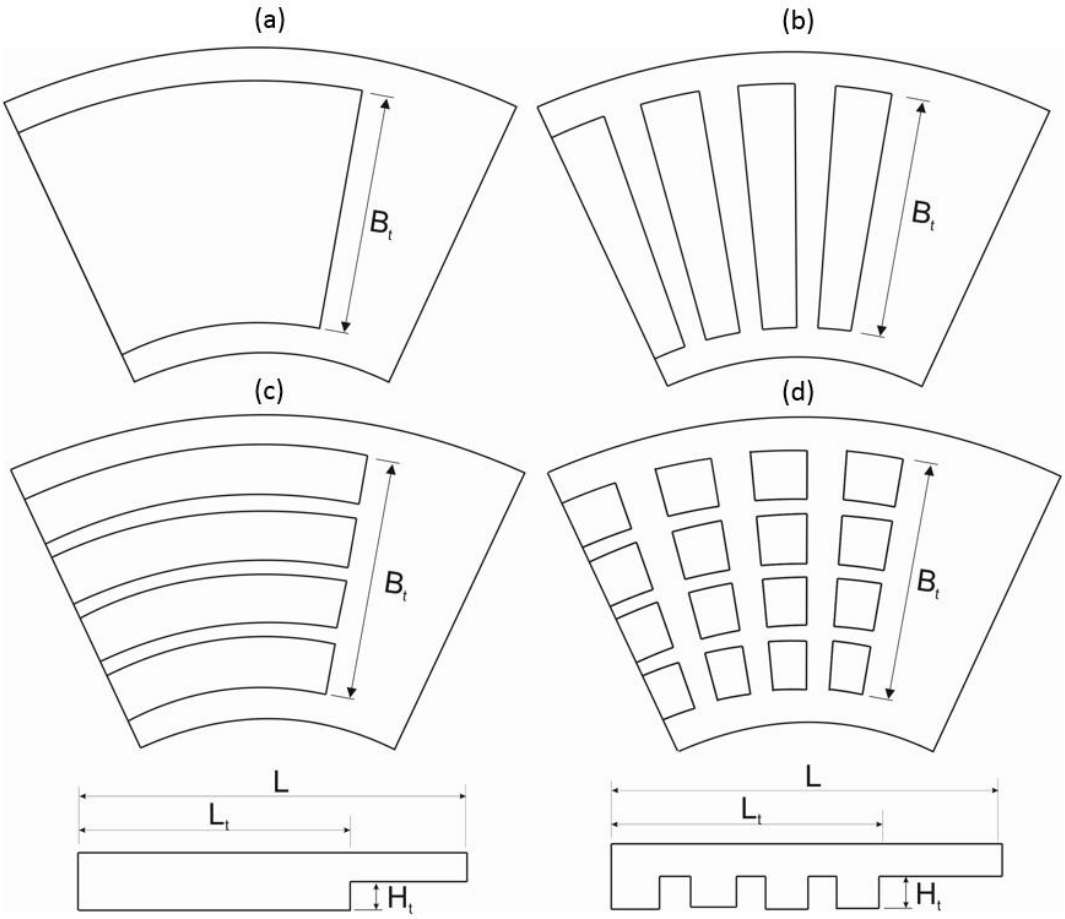


**Figure 28: Sketch of a (a) pocket bearing, (b) bearing with radial grooves, (c) bearing with circumferential grooves, and (d) bearing with rectangular surface texturing.**

In the following paragraphs, a comparison of important bearing parameters such as temperature, pressure, shear stress and minimum film thicknesses will be presented and discussed.

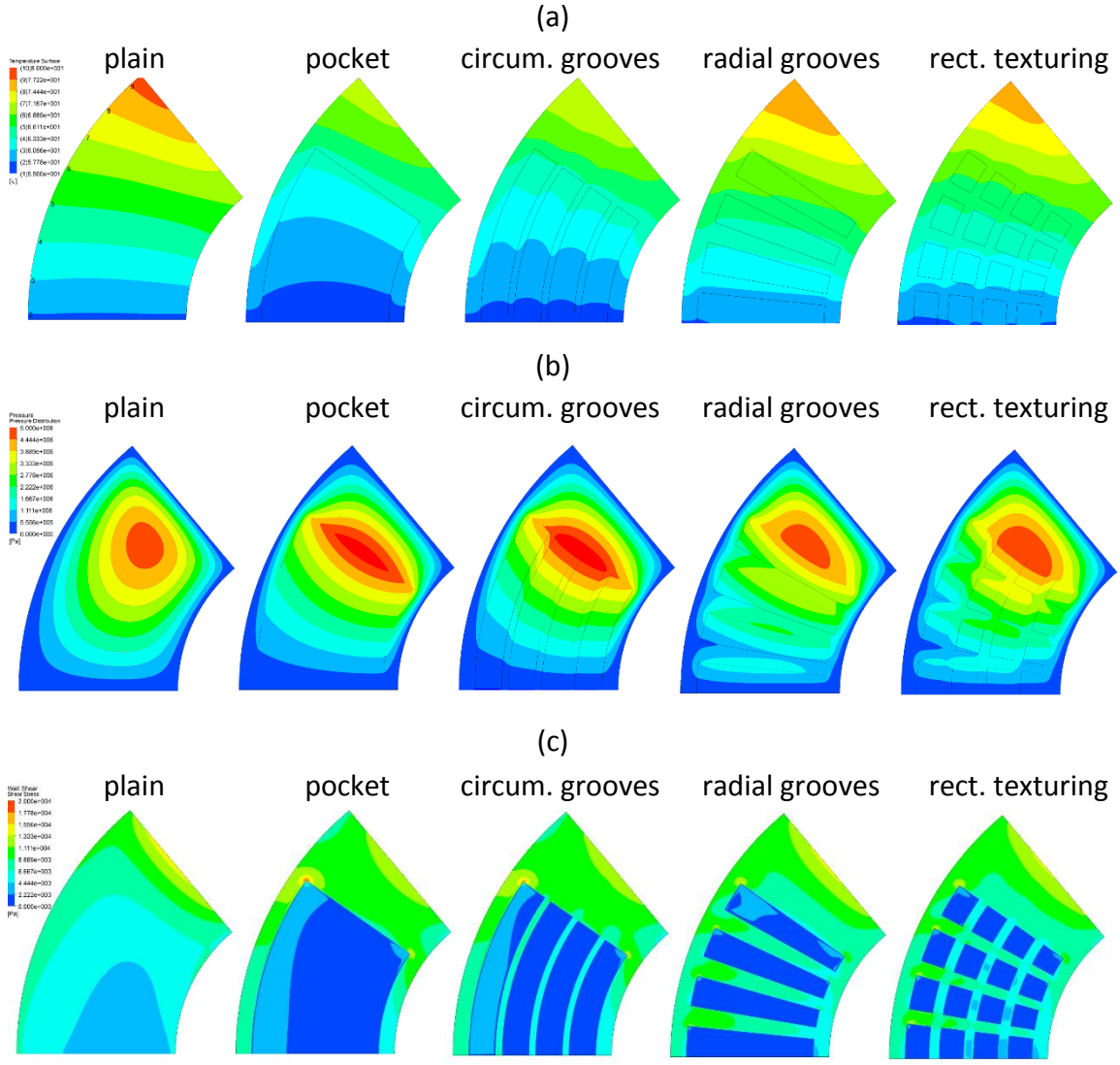


**Figure 29: Specific bearing load 2.0 MPa, rotational speed 1500 RPM: Color-coded contours of (a) temperature, (b) pressure and (c) shear stress in the fluid-pad interface for the textured geometries of the present study.**

### *Temperature distribution effects*

Figure 29(a) presents the distribution of temperature throughout the pad for the five different bearing types of the present study. All bearings are loaded with a specific load of 2.0 MPa, at a rotational speed of 1500 RPM. Figure 30(e),(f) presents the maximum fluid temperature versus the specific bearing load for two different values of rotational speed. From Figure 29(a), it is evident that, compared to other types, the pocket bearing and the bearing with circumferential grooves exhibit lower temperatures throughout the

pad surface. The blue areas, which correspond to cooler fluid, span a wider range of the inflow region, while the maximum temperatures (depicted in Figure 30(e),(f)) are 8.8% and 7% lower - for pocket and circumferential grooves respectively- in comparison to that of the plain bearing. For the bearing with radial grooves, the corresponding cooling effect is slight since the decrease of $T_{max}$ is only about 1%.

Typically, for all the considered bearing types, temperature values obtain maxima at the outer bearing radius close to the outflow region (Figure 29(a)). In Figure 30(e),(f), the difference of maximum fluid temperature of the four textured bearings in comparison to the maximum fluid temperature of the reference plain tilting pad bearing is presented. It is observed that, at low loads, the maximum fluid temperature is only slightly smaller in the textured bearings, whereas at higher loads temperature decrease is more pronounced, reaching approximately 9% for the pocket bearing at specific load of 2.0 MPa both at 1500 RPM and 3000 RPM. Bearings with radial grooves or rectangular texturing exhibit a behavior similar to that of the plain bearing, especially at higher specific loads.

***Pressure distribution***

Figure 29(b) displays the pressure distribution for each examined pad at the reference load of 2.0 MPa and corresponding rotational speed of 1500 RPM. Furthermore, the impact of the various geometries on pressure is depicted more clearly in Figure 31(a) where the pressure profiles at the bearing mid sector are shown. Based on Figure 31(a), we can observe that the pocket bearing and the bearing with circumferential grooves exhibit lower values of pressure at the inflow region compared to the plain bearing, however the trend is reversed in the region of maximum pressure, where those bearings exhibit superior behavior. Due to the higher values of maximum pressure, these two types of bearings display steeper pressure slopes, in comparison to those of the plain bearing, in the outflow region.

Caution must be given when examining the displayed results as, from Figure 31(a), it would appear that a plain bearing can carry higher loads because of the greater area beneath the pressure curve. However, given that all models were solved for the same loading conditions, we can infer that this conclusion would not be correct. The reason for the misleading image is that the pressure profile of one sector does not give the correct picture of the overall pressure distribution, the integral of which yields load capacity. In fact, as shown in Figure 29(b) and especially in Figure 32(a), bearings with patterns, thanks to their geometrical particularities, maintain pressure over a wider range in the radial direction.

***Shear force and friction effects***

In Figure 29(c), shear stress distribution at the lubricant-pad interface of the five different bearings is presented. In the plain bearing, shear stress is characterized by a gradual increase as a result of the gradual reduction of film thickness across the fluid domain. On the contrary, the textured geometries exhibit lower shear within the pocket/grooves and an almost constant (and fairly high) value of shear stress elsewhere.

The effect of each textured pattern on shear stress and, consequently, on friction is clarified with the aid of Figure 30(c,d). In these plots, the relative change of friction torque of the four textured bearings in comparison to that of a plain tilting-pad bearing is presented as a function of specific bearing load, while two values of rotational speed are studied (1500 RPM and 3000 RPM). The pocket bearing exhibits substantially reduced friction in the entire loading range, whereas the bearing with circumferential grooves follows the same trend, except for cases with very low values of specific load. On the contrary, the bearings with radial grooves or rectangular texturing exhibit friction forces higher than those of the standard, plain pad design.

***Film thickness***

The final critical parameter for comparing the bearings results is minimum film thickness. In Figure 30(a),(b), the impact of the studied geometries on this parameter is shown, for different loading and operating conditions of the bearings.

The pocket bearing and the bearing with circumferential grooves display the best behavior, with a remarkable increase in $H_{min}$ for all cases considered. The increase ranges from 10% to 22% for the pocket bearing and 4-20% for the bearing with circumferential grooves. It is of interest that, at the nominal bearing load (1500 RPM, 2.0 MPa), the performance of these two types of bearing is equivalent. The observations are similar for operation at 3000 RPM with the improvement in $H_{min}$ reaching approximately 24%.

For the bearing with rectangular texturing, the trend is similar but the improvement in $H_{min}$ is much milder, exhibiting an increase of only 6% at nominal load. On the contrary, radial grooves display a decreasing trend of $H_{min}$ reaching a lower value in comparison to that of plain bearing, at nominal operating conditions (1500 RPM, 2.0 MPa).

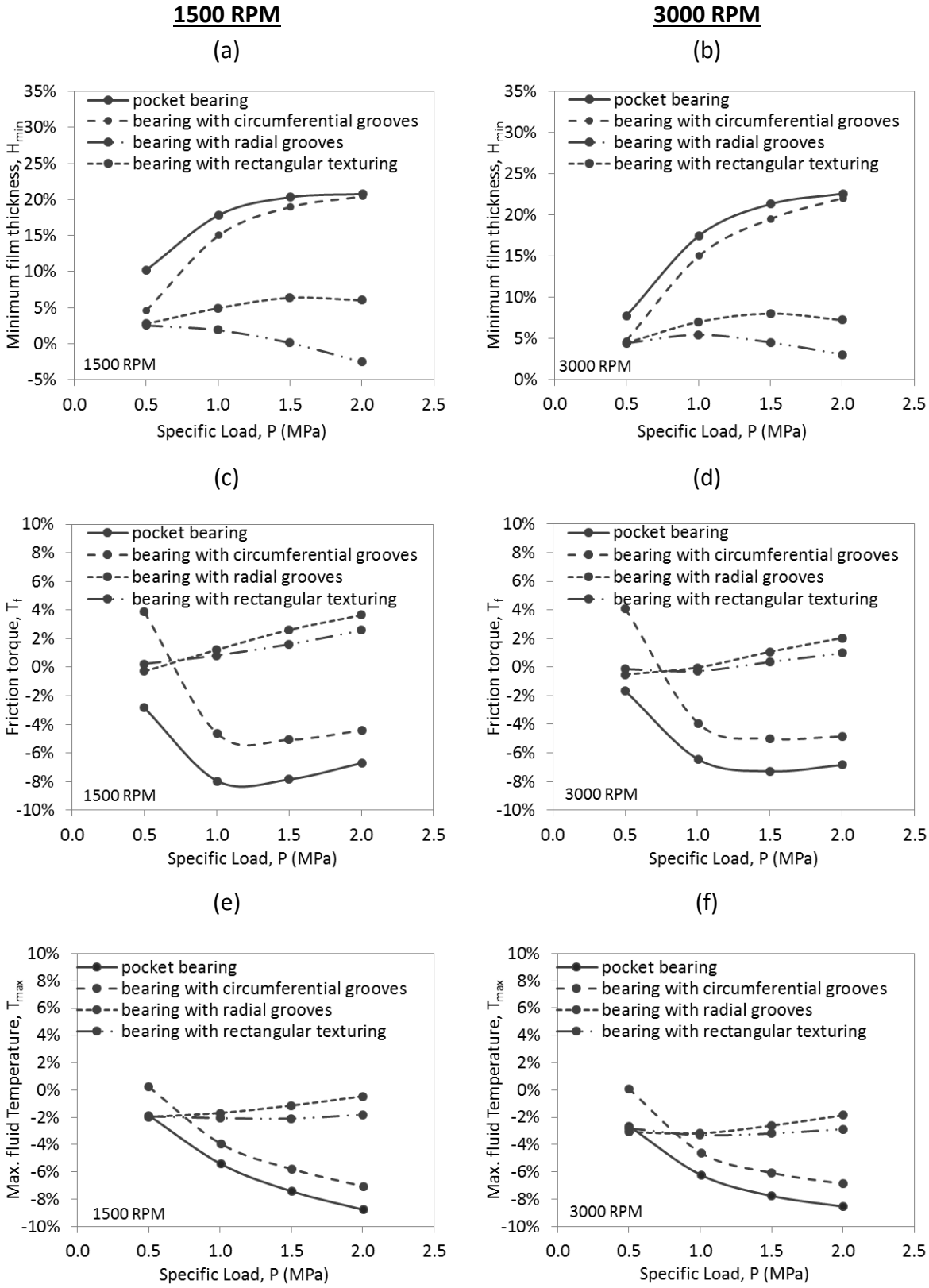


**Figure 30: Relative change of (a,b) Minimum film thickness, $H_{min}$, (c,d) Friction torque, $T_f$ and (e,f) Maximum fluid temperature versus specific bearing load, for the four textured bearings, in comparison to those of a plain tilting-pad bearing. Results are presented for two different values of rotational speed.**

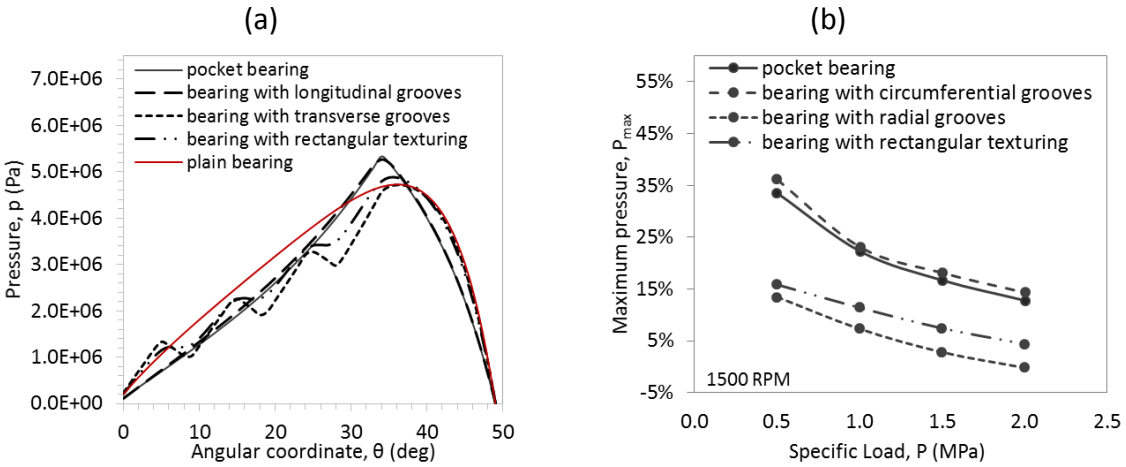


**Figure 31: Rotational speed 1500 RPM: (a) Pressure distribution at the bearing mid sector for nominal load of 2.0 MPa, and (b) relative change of maximum pressure as a function of specific bearing load, for the plain and the four textured bearings.**

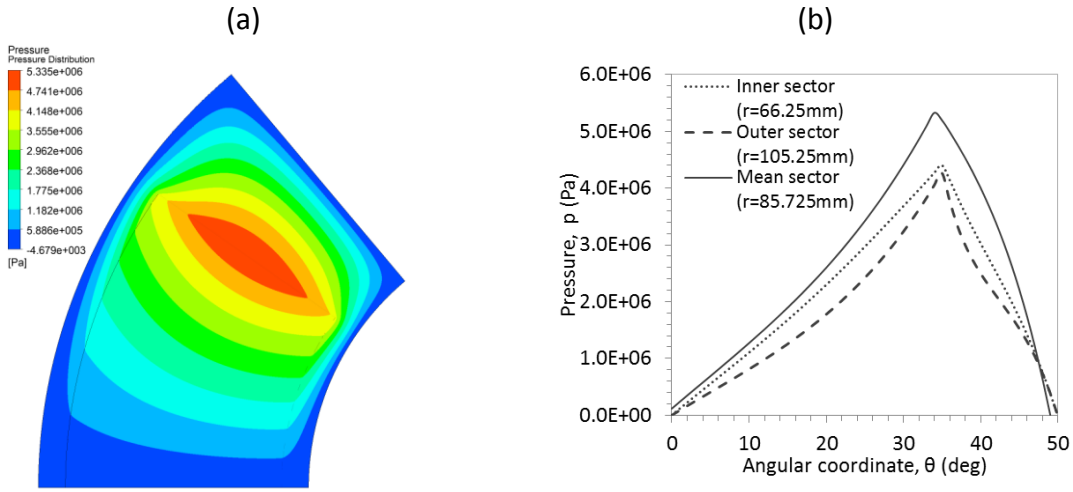


**Figure 32: Pocket bearing, nominal operating conditions (1500 RPM, 2.0MPa): (a) Color-coded contour of pressure as a function of specific bearing load, for the plain and the four textured bearings.**

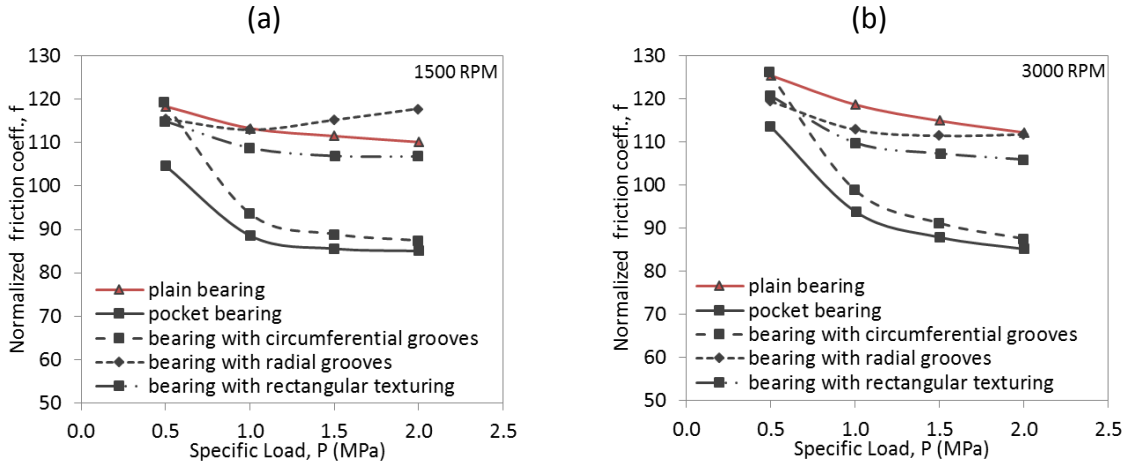


**Figure 33: Normalized friction coefficient as a function of bearing specific load for the plain bearing and the four textured bearings. Rotational speed (a) 1500 RPM, (b) 3000 RPM.**

***Summary***

In conclusion, the present results illustrate a superior performance of the open pocket bearing in comparison to the other bearing types. Very good results are also obtained for the bearing with circumferential grooves. On the contrary, the introduction of texturing in radial direction (spanwise) deteriorates the overall bearing performance especially at high bearing load Figure 33.

## 4.2. Parametric analysis

In the present section, the results of a systematic variation of the principal texture parameters are presented. Based on the results of the previous section, only open pocket bearings and bearings with circumferential grooves are investigated at representative operating conditions (1500 RPM and 3000 RPM, 1.0 MPa and 2.0 MPa). The considered parameters are: textured depth ($H_t$), and circumferential texture extent ($L_t$) and radial texture extent ($B_t$). The effect of parameter was examined separately, by varying only one at a time, while keeping the other two at their nominal value. The range of values examined was chosen to be sufficient in order to display the trends and to discover optimal points. In certain cases, the range of the tested values was limited by the inability of the bearing to reach an equilibrium position due to the strong impact of the textured geometry on the pressure build-up mechanism. Such a case, for example, was encountered when examining the textured length ($L_t$) parameter; in particular a value of $L_t = 0.8L$ did not permit the bearing to balance in some of the examined operating conditions.

### 4.2.1. Variation of Depth

In Figure 35, the effect of texture depth on bearing performance is demonstrated. In particular, the main bearing indices (minimum film thickness, friction torque, and maximum fluid temperature) are plotted against texture depth, for two values of specific load and rotational speed. Here, the values of circumferential extent ($L_t$) and radial extent ($B_t$) are kept constant and equal to $0.7\ L$ and $0.8\ B$ respectively.

Firstly, the maximum values of fluid temperature for the examined pads are shown in Figure 35(e,f) and a notable effect can be seen. Temperature is shown to be inversely proportional to textured depth, i.e. higher values of $H_t$, lead to lower values of $T_{max}$. For very higher values of $H_t$, a reduction of 7-9% in $T_{max}$ is attained for pocket bearings. A

similar trend is observed for the bearings with circumferential grooves, though the reduction is slightly less (6-8%).

At the same time, from Figure 35(c),(d), it can be seen that friction torque follows the same trend as maximum temperature and is inversely proportional to textured depth. For the case of a pocket bearing at $P = 1.0$ MPa, for $H_t = 50\mu\text{m}$, a decrease in friction torque of over 12%, in comparison to the plain bearing, is presented, with a tendency for further decreases.

In Figure 35(a),(b), minimum film thickness is plotted against texture depth. At the nominal bearing load of $2.0\ MPa$, minimum film thickness exhibits a maximum at values of texture depth around $20\ \mu m$ and $30\ \mu m$, whereas it decreases at higher values of texture depth. For example, for the bearing with circumferential grooves at $2.0\ MPa$, optimum performance (in terms of $H_{min}$) is attained for $H_t = 30\mu\text{m}$. The improvement compared to the plain bearing is of the order of 22%. At lower loads (Figure 35(a)), optimum values of $H_t$, depend on bearing type and shaft speed. In general, the optimal $H_t$ appears to be higher than $30\mu m$ for all cases considered.

In Figure 34, pressure and shear stress distributions in the streamwise direction, along the bearing mid sector, are presented for different values of $H_t$ of the pocket bearing. It is observed that maximum pressure increases with an increasing $H_t$, up to a value of approximately $20\ \mu m$. However, at higher values of $H_t$, the maximum pressure is shown to decrease. Therefore, an optimal value of $H_t$ exists, which for the present model lies between $20\ \mu m$ and $30\ \mu m$. This behavior can be explained as follows: As $H_t$ increases, the bearing deviates from the smooth converging bearing and behaves as a step bearing. Increase of $H_t$ leads to more fluid enter the domain, therefore enhancing the wedge effect of the bearing. However, at large values of $H_t$, the fluid entering cannot exit the domain, therefore, a large zone of recirculation is present at the bearing inflow, influencing bearing behavior.

Finally, as pictured in Figure 34(b), it is clear that shear stresses are substantially influenced by pocket depth, decreasing with increasing depth. At the inflow region, shear stresses decrease with increasing depth, but on the contrary increase at the region of maximum pressure. This is mainly due to the fact that the strain term $\partial u/\partial z$ is proportional in the pocket area.

In conclusion, it is found that pocket depth and the depth of circumferential grooves substantially affect both bearing performance (load capacity) and efficiency (friction) of the bearing, but towards different directions. While low textured depths provide higher minimum film thicknesses ($H_{min}$) and thus better load capacity, higher depths improve

the frictional characteristics, since they are characterized by to lower friction forces, torque resistance and energy consumption.

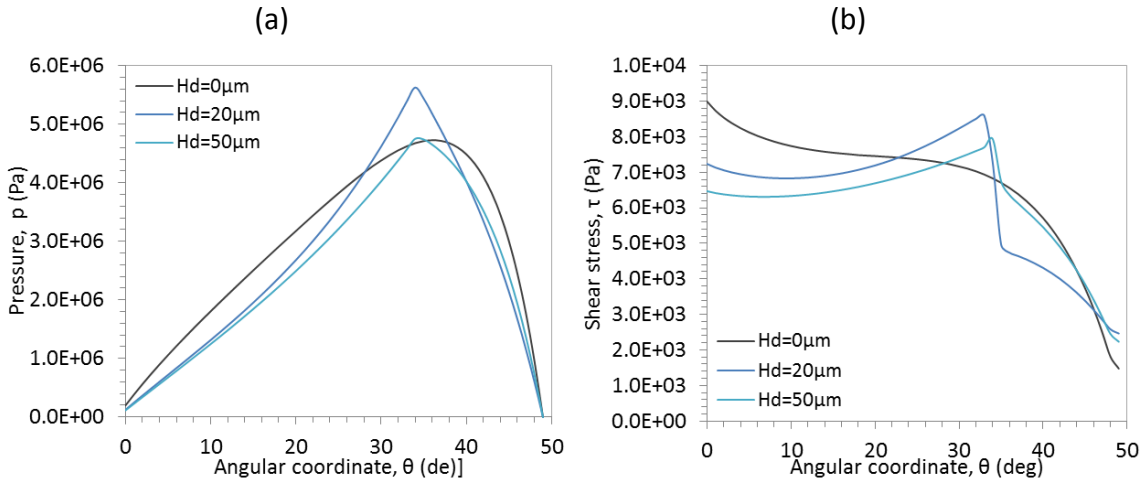


**Figure 34: Pocket bearing: specific bearing load 2.0 MPa, rotational speed 1500 RPM (a) Pressure (b) Shear stress distribution at the pocket bearing mid sector, for different values of pocket depth $H_t$.**

## 4.2.2. Variation of Circumferential Extent

In Figure 356 the effect of texture length on bearing performance is demonstrated. In particular, the main bearing indices (minimum film thickness, friction torque and maximum fluid temperature) are plotted against texture length for two values of specific load and rotational speed. Here, the values of textured depth ($H_t$) and radial extent ($B_t$) are kept constant and equal to $30\ \mu m$ and $0.8B$ respectively.

The effect on film thickness is insignificant at low bearing loads. Specifically, Figure 36(a), shows that minimum film thickness varies less than 2% for different values of texture extent in the circumferential direction. The results are quite different for high loads (2.0MPa) since there is a constant increase of $H_{min}$with increasing textured length ($L_t$). Although it seems that, based on the curve derivative, there is room for further improvement, for values greater than $L_t > 0.7$, the bearing displays instabilities, and an equilibrium position can not be attained.

In terms of efficiency, the pocket bearing proves to have the best performance. It achieves slightly lower friction torque values, reduced up to 10.5% in relation to the plain bearing at the specific load of 1.0 MPa, whereas the bearing with circumferential grooves attains a maximum reduction of 9% (Figure 36(c)). It is observed that friction torque increases with increasing textured length. $L_t$. At high values of specific load, (Figure 36(d)), the trend is milder.

Finally, based on Figure 36(e) and (f), we observe that the effect of $L_t$ on maximum oil temperature $T_{max}$ is practically insignificant.

While both the pocket bearing and the bearing with circumferential grooves display the behavior analyzed previously, the latter comprises a more economical solution if the performance at higher specific loads is what matters. This is contrary to the conclusion based on friction effects where the pad with the pocket pad bearing has better efficiency.

### 4.2.3. Variation of Radial Extent of Texturing

In Figure 357 the effect of texture width on bearing performance is demonstrated. In particular, the main bearing indices (minimum film thickness, friction torque and maximum fluid temperature) are plotted against texture width for two values of specific load and rotational speed. Here, the values of textured depth ($H_t$) and circumferential extent ($L_t$) are kept constant and equal to $30\ \mu m$ and $0.7L$ respectively.

Based on Figure 37, we can observe that the trends are similar for all the cases and the geometrical models. In particular, regarding the $H_{min}$, it can be deducted that maximum values are attained for a fairly wide range of applied texturing $B_t = (0.5 \div 0.7)B$. However, caution is needed as, for larger values of $B_t$, the performance abruptly falls. The same applies for the friction torque, except that optimum values are obtained at $B_t$ values around $0.7$, leading to a friction reduction of 9% at 1.0 MPa and 7% at 2.0MPa, for the case of the pocket bearing. The conclusions are similar for the bearing with circumferential grooves. The difference lies in the small decrease in efficiency, of the latter, as can be seen from Figure 37(c) and Figure 37(d).

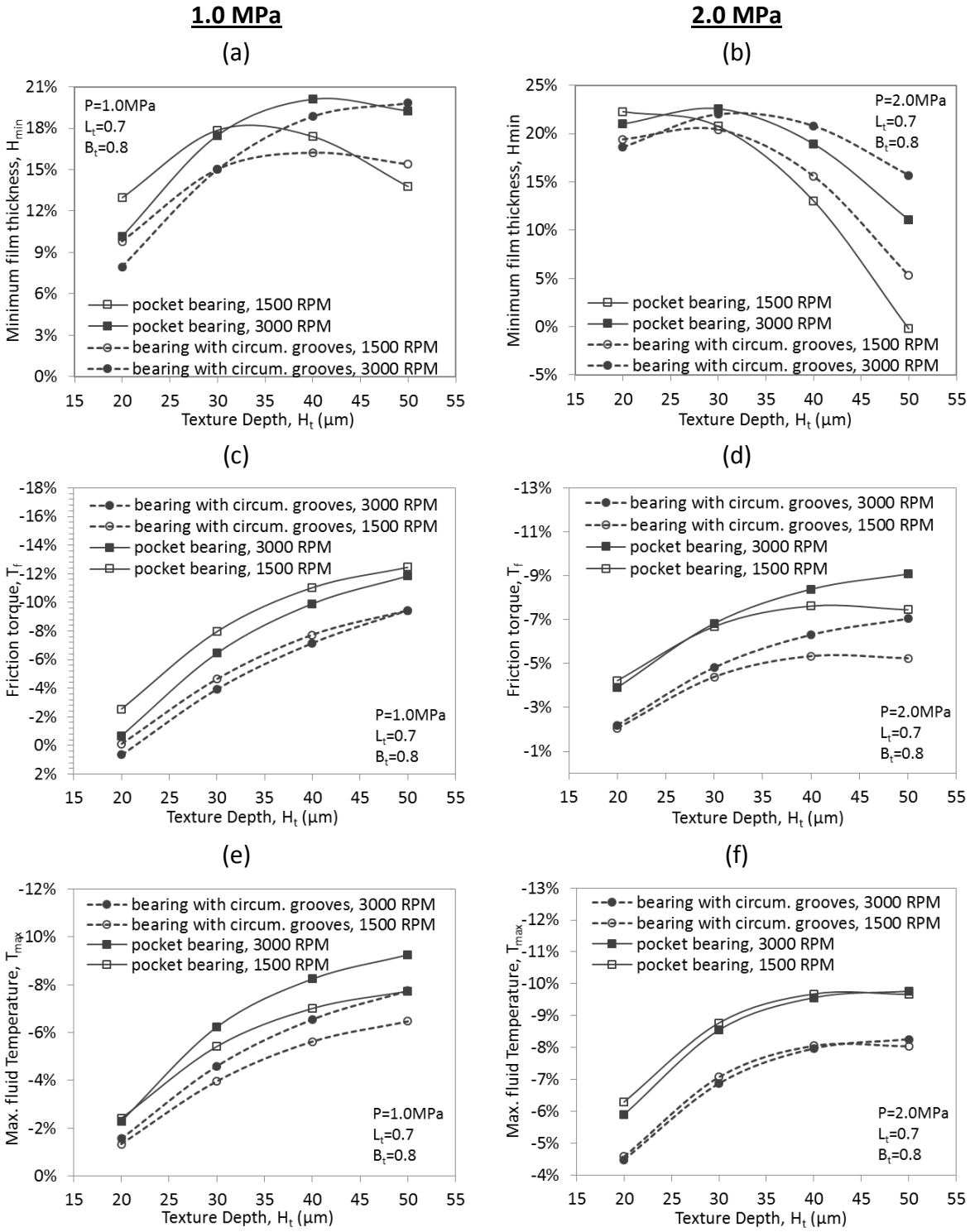


**Figure 35: Summarized results of the parametric analysis of textured depth for the pocket pad bearing and the bearing with circumferential grooves in relation to the performance of the plain pad bearing under certain operating conditions: (a,b) effects on minimum film thickness, (c,d) effects on friction torque, (e,f) effects on maximum fluid temperature.**

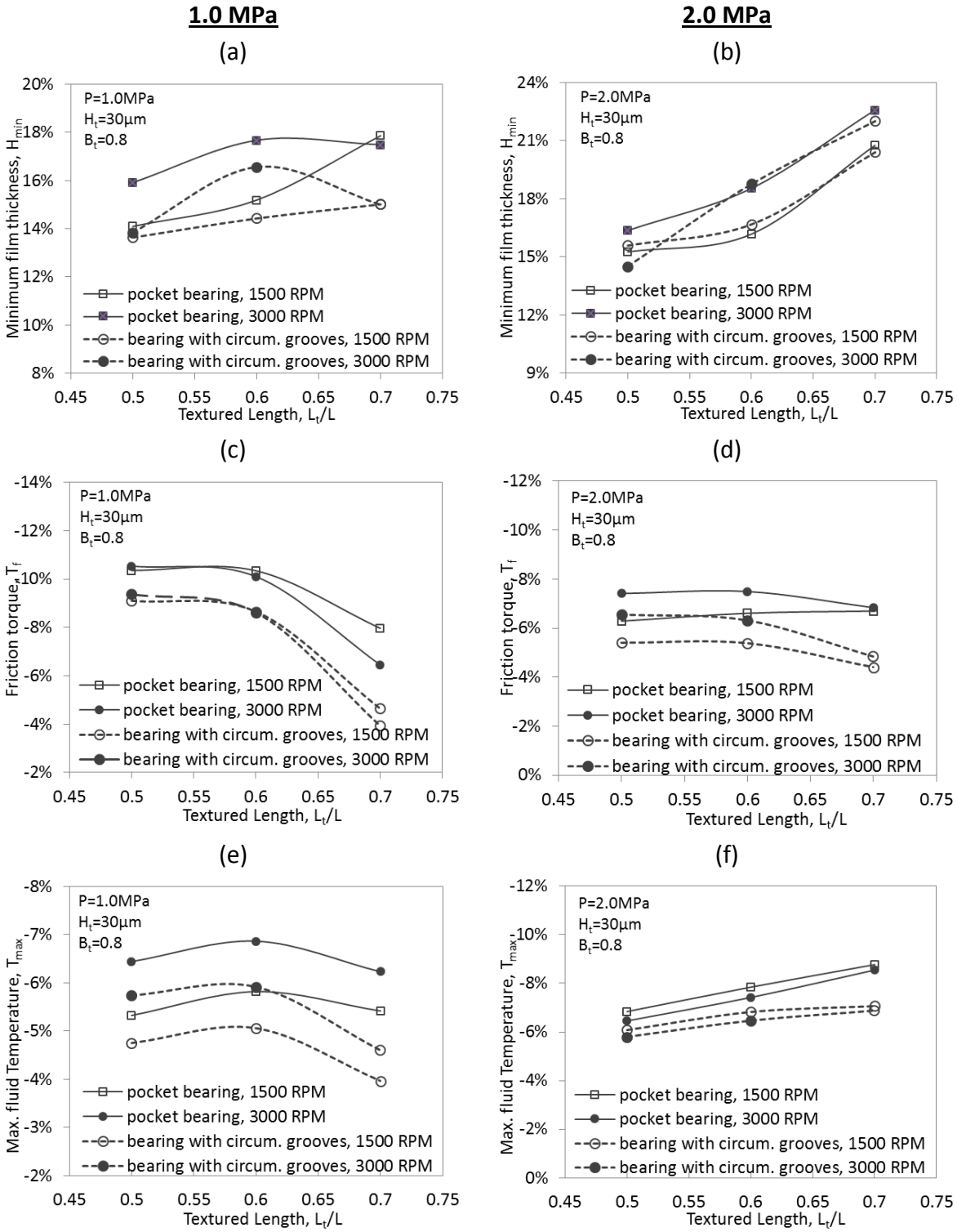


**Figure 36: Summarized results of the parametric analysis of textured length for the pocket pad bearing and the bearing with circumferential grooves in relation to the performance of the plain pad bearing under certain operating conditions: (a,b) effects on minimum film thickness, (c,d) effects on friction torque, (e,f) effects on maximum fluid temperature.**

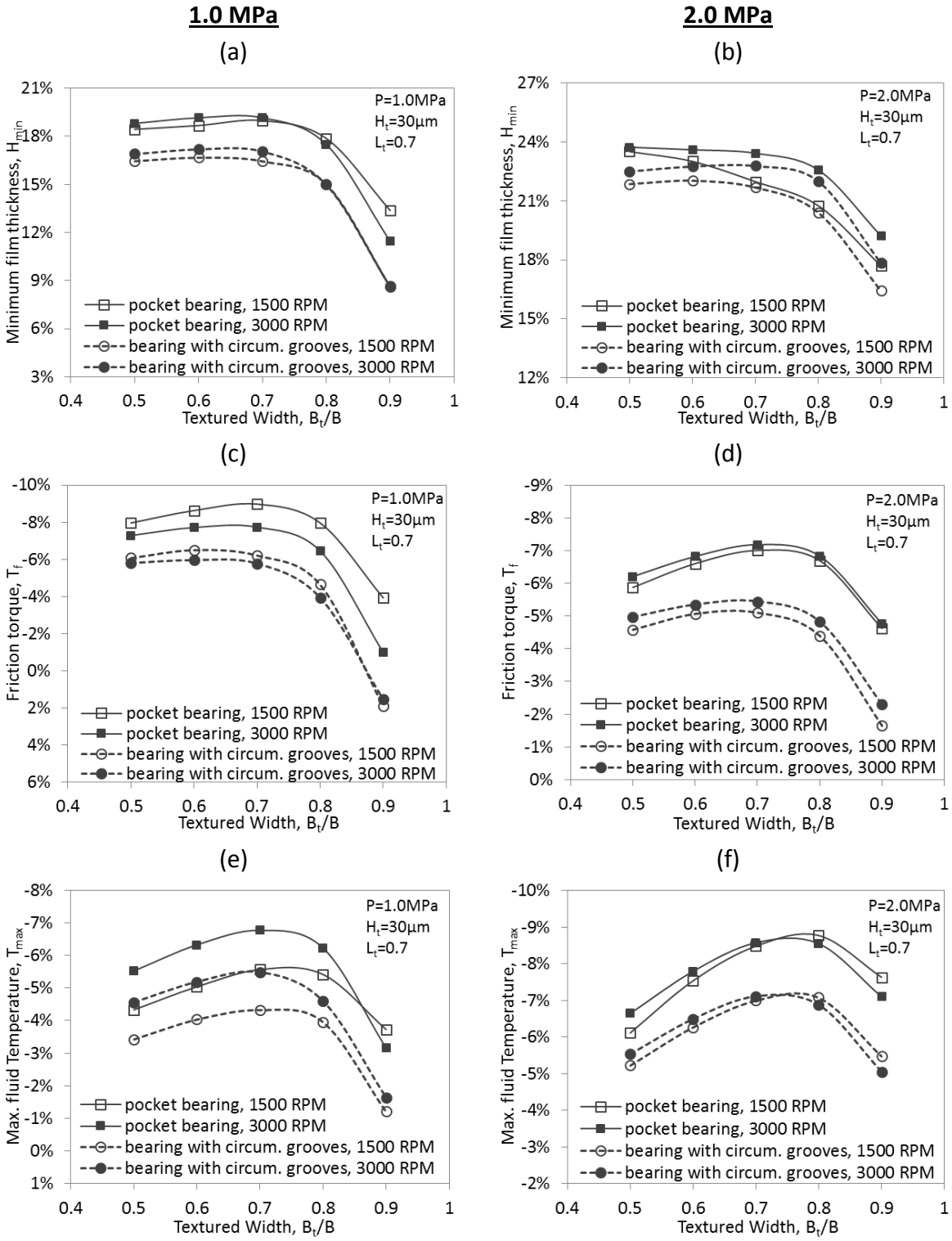


**Figure 37: Summarized results of the parametric analysis of textured width for the pocket pad bearing and the bearing with circumferential grooves in relation to the performance of the plain pad bearing under certain operating conditions: (a,b) effects on minimum film thickness, (c,d) effects on friction torque, (e,f) effects on maximum fluid temperature.**

## 4.3. Hydrophobic model

In this section, the effect of introducing hydrophobic properties on part of the tilting pad surface is investigated. The numerical model defined in Chapter 3 is utilized maintaining the geometrical dimensions, the spatial discretization and the operating parameters. The boundary conditions at the surface of the pad were appropriately altered in order to simulate the hydrophobic properties. The modified Navier's model which was introduced in Section 2.5 has been used for this purpose. A sketch of the hydrophobic slider studied here is presented in Figure 38. Geometric parameters are those corresponding to the reference pocket bearing, namely $B_S = 0.8B$ and $L_S = 0.7L$, where $B_S$ is the radial width of the hydrophobic part of the pad and $L_S$ is the corresponding circumferential length.

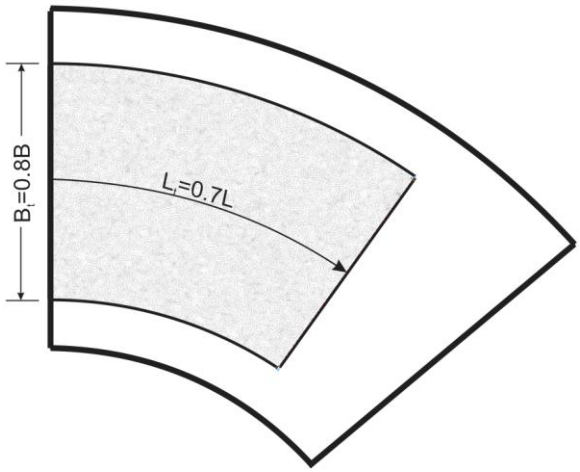


**Figure 38: Sketch of a plain tilting pad with hydrophobicity on part of the pad area.**

As has been already mentioned, the key parameter that quantifies the hydrophobic properties of a surface is the slip length b, whose definition has been given in Section 2.5. This quantity is a model: it does not physically exist nor does it remain constant when the fluid flow conditions on the surface change. For these reasons, the implementation of the non-dimensional number $b^* = b/H_{ref}$ in the simulation of hydrophobic surfaces is necessary. However, in our particular study, due to the variation in film thicknesses during the equilibrium finding process, the definition of a fixed $H_{ref}$ which normally describes a characteristic height of the fluid flow, is impossible. Thus, guided by the previous experience and the results of the standard, plain bearing, the value of $H_{ref} = 20\mu m$ was set as a representative one. Recent experimental work has shown that in superhydrophobic surfaces, slip-length b is generally in the range between a few hundred nanometers and several micrometers. Here, to identify the potential of introducing hydrophobicity on part of the stator, several simulations have been carried out with values of non-dimensional slip length varying from 0.1 to 1000.

All other parameters of the bearing were kept constant at their nominal values. The results are presented in Figure 39, where minimum film thickness and friction torque are plotted against non-dimensional slip length $b^*$. It is noted that the bearing is under a specific load of 2.0 MPa at 1500 RPM.

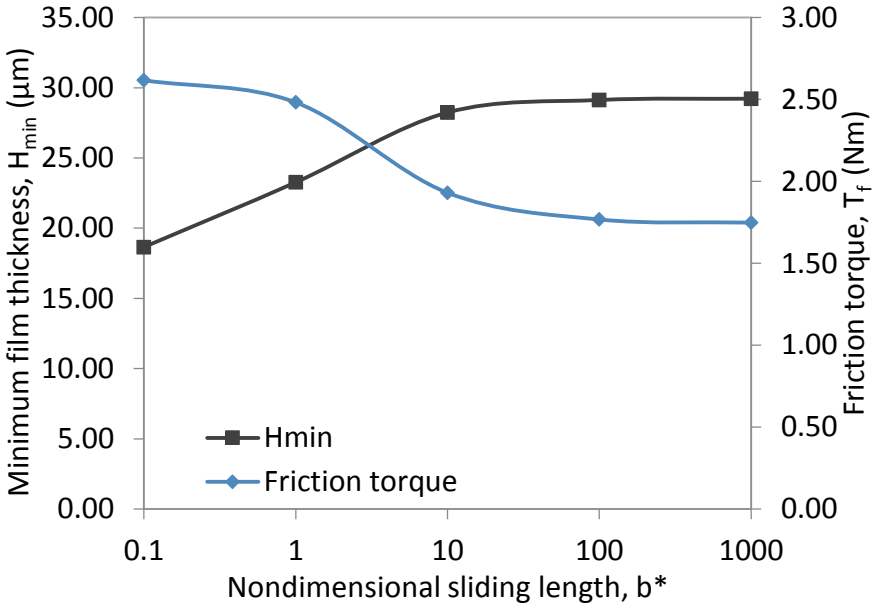


**Figure 39: Specific load 2.0 MPa, rotational speed 1500 RPM: Minimum film thickness, $H_{min}$, and friction torque $T_f$, versus non-dimensional slip length b*.**

The results of Figure 39 demonstrate a substantial increase of minimum film thickness and a substantial decrease of friction torque at increasing of non-dimensional slip length $b^*$. In particular, values of $b^*$ close to zero, the bearing approaches the performance of the conventional, plain, tilting pad thrust bearing. Progressively in the range between 0.1 and 10, the performance indices are greatly enhanced whereas for values of $b^*$ greater than 10, there is actually no further improvement. Although $b^*$ values of 10 correspond to slip lengths of 200μm, far exceeding the limits of the contemporary technological capabilities, this figure indicates the general potential of the hydrophobicity in pivoted-pad thrust bearings.

For the case of $b^* = 100$, where the benefit is the maximum possible, the following results are presented: In Figure 40, the slip effect is illustrated by plotting fluid velocity in the fluid-pad interface. In the non-hydrophobic part of the stator, fluid velocity is zero (no-slip condition), where at the hydrophobic part, non-zero velocity observed.

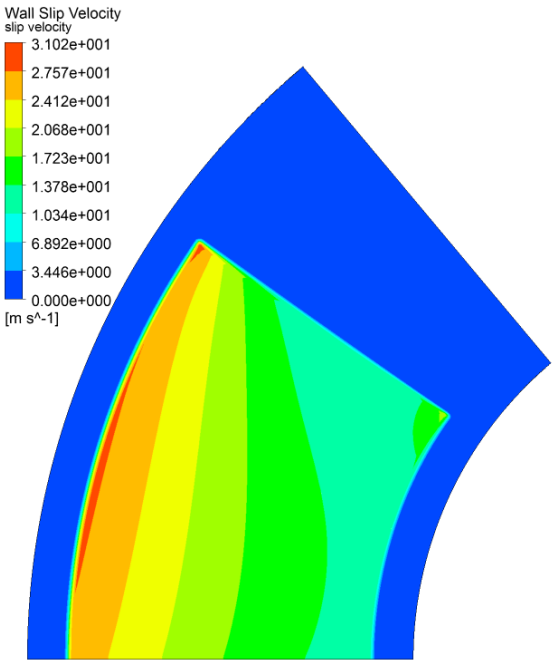


**Figure 40: Specific load 2.0 MPa, rotational speed 1500 RPM, b*=100: Color coded contours of fluid velocity at the fluid-pad interface of the hydrophobic slider are presented.**

While pressure distribution (Figure 41(a)) is quite similar to that resulting from the introduction of a pocket geometry (see Section 4.1), the temperature field is completely different as is evident from Figure 41(b). The low shear stresses in the hydrophobic region, are associated with lower heat generation, and, therefore, with lower local values of oil temperature. However, outside the region in question, temperature distribution is familiar; temperature values attain maxima at the outer bearing radius close to the outflow region and are slightly reduced (approximately by 2 $^{o}$C) compared to the plain bearing.

Due to the improved friction indices, a remarkable reduction in power loss of the order of 32% is attained for the bearing with partial hydrophobic properties. Indeed, as shown in Figure 42(a), this improved performance is maintained at different values of bearing specific load.

The increase in load capacity is even greater, as can be deduced by the corresponding increase in $H_{min}$. As shown in Figure 42(b), for the case of 1500 RPM and 2.0 MPa, the bearing with hydrophobic treatment displays a minimum film thickness, $H_{min}$ of about 30μm whereas the plain bearing has $H_{min} \cong 18\mu m$. Regarding this parameter, an improvement of over 40% is maintained even at low bearing loads.

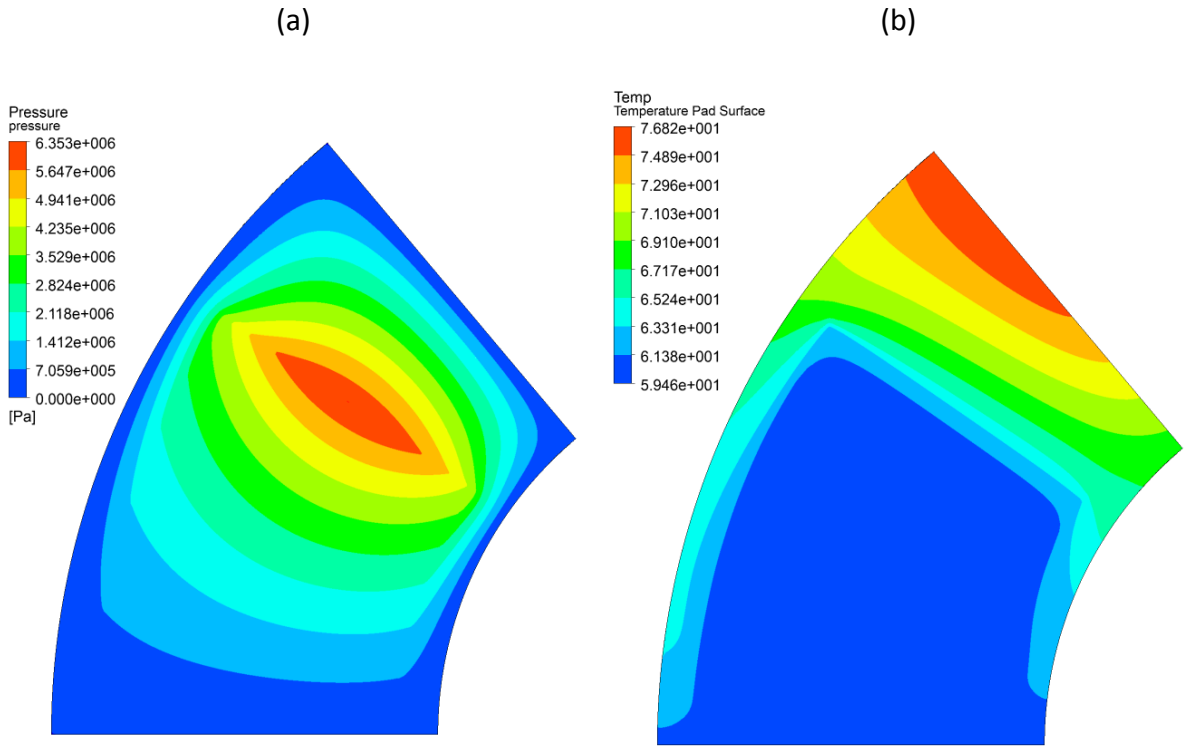


**Figure 41: Specific load 2.0 MPa, rotational speed 1500 RPM, b*=100: (a) pressure, and (b) temperature at the fluid-pad interface of the hydrophobic thrust bearing.**

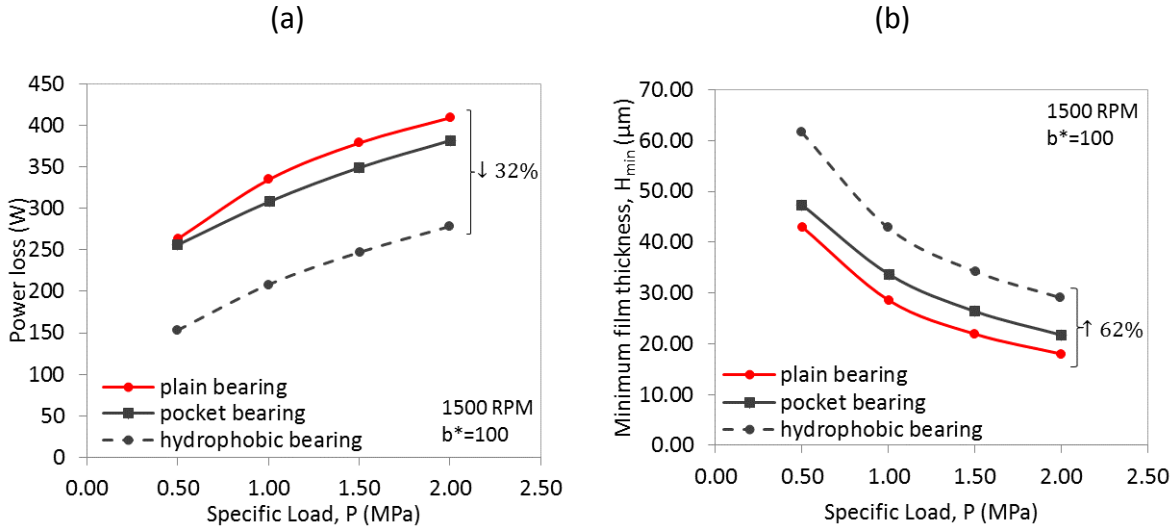


**Figure 42: Performance of tilting pad thrust bearing with hydrophobic properties in relation to specific load and compared to the plain bearing and the pocket bearing: (a) power loss, (b) minimum film thickness.**

# 5. Conclusions and Future work

## 5.1. Conclusions

The results of the present work allow for valuable conclusions regarding the application of surface treatment technologies (artificial surface texturing or hydrophobicity) to tilting-pad thrust bearings. In particular, if appropriately designed, surface treatment can grant notable improvements on the overall bearing behavior: a load carrying capacity with increased film thickness can be achieved, energy losses due to friction can be moderated and maximum oil temperatures can be reduced. However, the selection of surface treatment type and parameters is critical.

Based on the present results, pocket bearings and bearings with circumferential grooves, display enhanced tribological indices, whereas bearings with radial grooves or rectangular texturing have mildly positive or even negative behavior, in comparison to conventional plain bearings. In particular, minimum film thickness, as an indicator of load bearing capacity and of risk of contact, is improved by 10-22% for the pocket bearing and by 4-20% for the circumferentially grooved bearing. Meanwhile, friction is substantially reduced for both these bearings, though for the latter the improvement is not maintained at low loads. Finally, the reduction in maximum temperature is of the order of 8.8% and 7%, respectively. It is clear from the above that the pocket bearing has the best overall performance. However, the bearing with circumferential grooves achieves significant improvements as well. In some cases, these improvements are sufficient so that the circumferentially grooved bearing may be preferred for its lower production cost, as a result of a smaller surface area requiring treatment. It should be stressed that by applying proper texturing, the same film thickness and thus load capacity can be achieved with a pad of smaller principal dimensions. In that case, friction is further reduced, not only because of surface treatment, but also because of the smaller active area of the bearing.

Furthermore, parametric analysis revealed the impact of the main texture parameters (texture depth, circumferential and radial texture extent) on the performance of tilting-pad thrust bearings. Values of texture depth around 30 μm ensure high values of minimum film thickness (equivalently: load capacity), but lead to higher friction torque, whereas larger depths have the opposite effect. Depending on the demands of the application, a compromise between those opposing effects, may be important for optimal design. Texture extent in the streamwise direction plays a less important role in terms of performance; it does not affect temperatures, while film thickness is only affected at high bearing loads. Therefore, it can be minimized to reduce the technical cost of texturing. The radial extent of texturing, on the other hand, seems to influence more markedly, with all criteria indicating an optimal value around $B_t = 0.7B$.

Remarkable enhancements can also be observed with the use of another recent technological feature in tribological applications, namely that of hydrophobicity. Power loss due to friction may be reduced by around 32% throughout a broad range of specific loads, while gains in load capacity are even greater, reaching 62%. Here the main design parameter is the non-dimensional slip-length $b^*$. This parameter is optimum in regards to both friction reduction and load capacity for values greater than 10, corresponding, in the present model, to actual slip lengths of 200 μm. This value far exceeds the limits of contemporary technology, but indicates the great potential of hydrophobic technology in pivoted pad thrust bearings.

## 5.2. Future work

Driven by the simplifying assumptions of the present study, suggestions for future research include modeling of tilting-pad thrust bearings, in which the following parameters are also taken in consideration:

i. Thermal and elastic deformations due to the temperature and pressure fields, resulting in thermoelastohydrodynamic (TEHD) analysis.
ii. The detailed groove geometry and its exact influence on bearing performance.

At the same time, the implementation of surface texturing requires further investigation. Areas of interest could include:

i. The optimization of the exact geometric pattern, given the operating needs of particular applications.
ii. Economic cost assessment studies, taking into account performance degradation of surface properties due to wear over time.
iii. Validation of the theoretically predicted results of the present study through experiments.

## Literature

[1] Kim, K. W., Tanaka, M., Hori, Y., 1983, “A Three-Dimensional Analysis of Thermohydrodynamic Performance of Sector-Shaped, Tilting-Pad Thrust Bearings”, ASME Journal of Lubrication Technology, Vol. 105, No. 3, pp. 406-413.

[2] Heckelman, D., Ettles, C. M., 1987, “Viscous and Inertial Pressure Effects at the Inlet to a Bearing Film”, STLE Transactions, Vol. 31, No. 1, pp. 1-5.

[3] Kim, J. S., Kim, K. W., 2002, “Effect of Distance Between Pads on the Inlet Pressure Build-Up on Pad Bearings”, ASME Journal of Tribology, Vol. 124, pp. 506-514.

[4] Vohr, J. H., 1981, “Prediction of Operating Temperature of Thrust Bearings”, ASME Journal of Lubrication Technology, Vol. 103, No. 1, pp. 97-106.

[5] Ettles, C. M., 1976, “The Development of a Generalized Computer Analysis for Sector Shaped Tilting Pad Thrust Bearings”, ASLE Transactions, Vol. 19, 2, pp. 153-163.

[6] Dadouche, A., Fillon, M., Dmochowski, W., (2006). “Performance of a Hydrodynamic Fixed Geometry Thrust Bearing: Comparison between Experimental Data and Numerical Results”, Tribology Transactions, 49, pp. 419–426.

[7] Brizmer, V., Kligerman, Y., and Etsion, I., 2003, “A Laser Surface Textured Parallel Thrust Bearing,” Tribol. Trans., 46(3), pp. 397–403.

[8] Papadopoulos, C. I., Nikolakopoulos, P. G., Kaiktsis, L., 2009, “Flow and Engineering Assessment in Converging Microchannels with Trapezoidal Roughness and Slip,” 36th Leeds-Lyon Symposium on Tribology: Multi Facets on Tribology, Lyon, Sept. 1–3.

[9] Dobrica, M. B., Fillon, M., Pascovici, M. D., Cicone, T., 2007, “Texturing Effects in Plane-Inclined Slider Bearings,” STLE-ASME International Joint Tribology Conference, San Diego, Oct. 22–24.

[10] Brajdic-Mitidieri, P., Gosman, A. D., Ioannides, E., Spikes, H. A., 2005, “CFD Analysis of a Low Friction Pocketed Pad Bearing,” ASME J. Tribol.,127(4), pp. 803–812.

[11] Etsion, I., Klingerman, Y., 1999, “Analytical and Experimental Investigation of Laser-Textured Mechanical Seal Faces”, Tribology Transactions, Vol. 42, No. 3, pp. 511-516.

[12] Glavatskikh, S. B., McCarthy, D. M. C., Sherrington, I., 2005, “Hydrodynamic Performance of a Thrust bearing with Micropatterned Pads”, Tribology Transactions, Vol. 48, pp. 392-498.

[13] Papadopoulos, C. I., Efstathiou,E. E., Nikolakopoulos, P. G., Kaiktsis, L., 2011. "Geometry Optimization of Textured Three-Dimensional Micro- Thrust Bearings", Journal of Tribology, 133(4), doi:10.1115/1.4004990.

[14] Yang, H., Ratchev, S., Turitto, M., Segal, J., 2009. "Rapid Manufacturing of Non-Assembly Complex Micro-Devices by Stereolithography". Tsinghua Science and Technology, 14, pp. 164-167.

[15] Etsion I., 2005, “State of the art in laser surface texturing”, ASME Journal of Tribology.,127(4), pp. 248-253.

[16] Etsion I., 2010, “Laser surface texturing and applications”. In: Nikas GK, editor. Recent developments in wear prevention, friction and lubrication. Kerala, India: Research Signpost, pp. 137–58.

[17] Dobrica, M. B., Fillon, M., 2009, “About the Validity of Reynolds Equation and Inertia Effects in Textured Sliders of Infinite Width,”Proc. Inst. Mech.Eng., Part J: J. Eng. Tribol., 223(1), pp. 69–78.

[18] Cupillard, S., Glavatskih, S., Cervantes M.J. (2009), “3D Thermohydrodynamic Analysis of a Textured Slider”. Tribology International, 42, pp. 1487–1495.

[19] Marian, V. G., Kilian, M., Scholz, W., 2007, “Theoretical and Experimental Analysis of Partially Textured Thrust Bearing with Square Dimples,” Proc. Inst. Mech. Eng., Part J: J. Eng. Tribol., 221(7), pp. 771–778.

[20] Van Ostayen, R. A. J., Van Beek, A., Munnig-Schmidt, R. H., 2007, “Film Height Optimization of Hydrodynamic Slider Bearings,”Proceedings of the ASME/STLE International Joint Tribology Conference, IJTC 2007, PART A, pp. 237–239.

[21] Papadopoulos, C. I., Nikolakopoulos, P. G., Kaiktsis, L., 2011, “Evolutionary Optimization of Micro-Thrust Bearings with Periodic Partial Trapezoidal Surface Texturing,”J. Eng. Gas Turbines Power, 133(1), pp. 1–10.

[22] Ma G.J., Wu C.W., Zhou P., 2007, “Wall Slip and Hydrodynamics of two-dimensional Journal Bearing”, Tribology International, 40(7), pp 1056-1066.

[23] Pavlioglou S.K. et al, 2014, "Tribological Optimization of Thrust Bearings Operated with Lubricants of Spatially Varying Viscosity", ASME GT2014-25292, pp 1-10.

[24] Vinogradova, O. I., 1999, “Slippage of Water Over Hydrophobic Surfaces,”Int. J. Min. Process., 56, pp. 31–60.

[25] Zhu, Y., Granick, S., 2001, “Rate Dependent Slip of Newtonian Liquid at Smooth Surfaces,” Phys. Rev. Lett., 87, pp. 096-105.

[26] Choo, J. H., Glovnea R. P., Forrest A. K., Spikes H. A., 2007, “A Low Friction Bearing Based on Liquid Slip at the Wall.” Journal of Tribology 129(3): 611.

[27] Hamrock, B. J., Schmid, S.R., Jacobson, B.O., Fundamentals of Fluid Film Lubrication, 2004.

[28] Borras, F. X., Master Thesis: Multiphysics Modelling of Spring- Supported Thrust Bearings for Hydropower Applications, Lelua, 2012.

[29] McCarthy, D. M., Doctoral Thesis: Sliding Bearings for Hydropower Applications - Novel Materials, Surface Texture and EALs, 2008.

[30] Stachowiak, G. W., Batchelor, A. W., 2005,Engineering Tribology, 3rd ed. Butterworth and Heinemann, Burlington, MA, Chap. 4.

[31] Raimondi, A. A., Szeri, A. Z., 1984, Journal and thrust bearings, in Handbook of Lubrication, v. II, Booser, E.R., Ed., 413-462, CRC Press, Boca Raton, FL.

[32] Gardner, W. W., 1988, "Tilting-pad thrust bearing tests, influence of pivot location", ASME Journal of Tribology., 110(4), pp. 609–613.

[33] Fillon, M., Glavatskih, S.B., 2008. "PTFE-Faced Centre Pivot Thrust Pad Bearings: Factors Affecting TEHD Performance." Tribology International 41(12), pp. 1219–1225.

[34] Shinkle, J. N., Hornung, K. G., 1965, "Frictional Characteristics of Liquid Hydrostatic Journal Bearings", ASME Journal of Basic Engineering, Vol. 87, Issue 1, pp. 163-169.

[35] Raptis, L., Diploma Thesis: Software development for the solution of hydrodynamic lubrication problems in main bearings of marine Diesel engines, Athens, 2004.

[36] Granick, S., 2003, "Equation for Slip of Simple Liquids at Smooth Solid Surfaces", American Chemical Society, Langmuir (19)pp. 5065–71.

[37] Wasilczuk, M., Grzegorz R., 2013. "On the Possibilities of Decreasing Power Loss in Large Tilting Pad Thrust Bearings." ISRN Tribology 2013, pp. 1–9.

[38] Ettles, C. M., 1980, "Size Effects in Tilting Pad Thrust Bearings", Wear, 59, pp. 231-245.

[39] Glavatskih, S. B., Fillon, M., Larsson, R., 2002, "The Significance of Oil Thermal Properties on the Performance of a Tilting-Pad Thrust Bearing." Journal of Tribology 124(2), pp. 377.